



An EPR study of the two-dimensional magnetic solitons  
by Kala Subbaraman

A dissertation submitted in partial fulfillment of the requirements for the degree of Doctor of  
Philosophy in Physics  
Montana State University  
© Copyright by Kala Subbaraman (1996)

Abstract:

Two dimensional or layered Heisenberg magnets in the classical continuum limit are known to support localized regions of magnetization called solitons. A theoretical and experimental investigation of a two dimensional spin five-halves, Heisenberg antiferromagnet has been conducted. Theoretical calculations that determine how the solitons will affect the temperature-dependent electron paramagnetic resonance (EPR) linewidth have been done. These calculations include the dependence of EPR linewidth on the nonmagnetic impurity concentration. The calculation consists of two parts. The first is the determination of the discrete core energy using simple numerical methods and the energy of the continuum area surrounding the core of the soliton. The second part involves the calculation of the dynamic correlation function performed within the framework of the soliton-magnon interaction picture. One of the most significant effects indicated by the above calculations is the large change in the EPR linewidth with very small amounts of doping nonmagnetic impurity atoms. The magnon contribution to the temperature dependent linewidth was calculated by extending the calculations of Chakravarty and Orbach for a quantum Heisenberg antiferromagnet. It was found to be rather insignificant when compared to the soliton contribution in the same temperature range.

We have investigated the possible effects of doping  $(n\text{-propylammonium})_2\text{Mn}_{1-x}\text{M}_x\text{Cl}_4$ , a quasi two-dimensional antiferromagnet with  $S = 5/2$ , where  $M = \text{Cadmium, Zinc or Magnesium}$ . The nonmagnetic impurities are present in very small molar quantities well below the percolation limit. Very good qualitative agreement between the observed linewidth temperature dependence and the above theory indicate that solitons indeed contribute to the thermodynamic behavior of layered magnetic compounds. A quantitative comparison of the soliton excitation energies as a function of impurity concentration reveals good agreement between theory and experiment.

AN EPR STUDY OF THE TWO-DIMENSIONAL MAGNETIC  
SOLITONS

by  
Kala Subbaraman

A dissertation submitted in partial fulfillment  
of the requirements for the degree

of

Doctor of Philosophy

in

Physics

MONTANA STATE UNIVERSITY  
Bozeman, Montana  
October 1996

D378  
Su 139

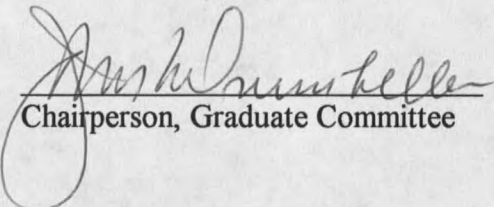
APPROVAL

of a thesis submitted by

Kala Subbaraman

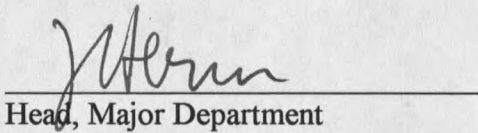
This thesis has been read by each member of the thesis committee and has been found to be satisfactory regarding content, English usage, format, citations, bibliographic style, and consistency, and is ready for submission to the College of Graduate Studies.

11/15/96  
Date

  
Chairperson, Graduate Committee

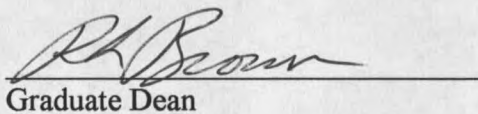
Approved for the Major Department

11-15-96  
Date

  
Head, Major Department

Approved for the college of graduate studies

1/20/97  
Date

  
Graduate Dean

## STATEMENT OF PERMISSION TO USE

In presenting this thesis in partial fulfillment of the requirements for a doctoral degree at Montana State University, I agree that the Library shall make it available to borrowers under rules of the Library. I further agree that copying of this thesis is allowable only for scholarly purposes, consistent with 'fair use' as prescribed in the U.S. Copyright Law. Requests for extensive copying or reproduction of this thesis should be referred to University Microfilms International, 300 North Zeeb Road, Ann Arbor, Michigan 48106, to whom I have granted "the exclusive right to reproduce and distribute my dissertation for sale in and from microfilm or electronic format, along with the right to reproduce and distribute my abstract in any format in whole or in part."

Signature Stale

Date 11-16-96

## ACKNOWLEDGEMENTS

I would like to sincerely thank my advisor Jack Drumheller for his support, advice, and encouragement during the time this thesis work was done. Craig Zaspel provided me with the thesis problem and helped me through nearly all aspects of it; I am indebted to Craig for sharing his ideas with me and for so much technical guidance that was given freely.

Thanks to Daniel Teske who helped me learn to use the AC susceptometer and Todd Grigereit for EPR spectrometer counsel, to Bob Parker for endless technical support on computer software and hardware issues, to Norm Williams and Erik Andersen for technical help. I wish to thank Dr. Ken Emerson for giving me free use of his chemistry laboratory and for sharing his expertise in crystal growth techniques. I am grateful to Jim Anderson for helping me with powder X-Ray diffraction measurements. Special thanks to Ray Larsen who put in lots of time and effort in the single crystal X-Ray diffraction measurements. Special appreciation is due to the office staff of Rose Waldon, Margaret Jarrett, Deb Chard and Carolyn Mazzatti who were very helpful. I thank John Hermanson for giving me the opportunity to continue my graduate studies at Montana State University and the rest of the faculty who made my stay here such an enjoyable and intellectually rewarding experience.

My husband Sunil deserves my deepest appreciation for his patience and for his constant support and encouragement during all my years at graduate school.

## TABLE OF CONTENTS

	Page
1. INTRODUCTION	1
1.1 Heitler London Model theory of Hydrogen molecule	2
1.2 Magnetic order	6
1.3 Long range order in low-dimensional systems	8
1.4 Topological excitations	13
References cited in Chapter 1	18
2. SURVEY OF THE THEORY OF EPR	20
2.1 Relaxation function and dynamic susceptibility	20
2.2 Paramagnetic resonance	23
2.3 The Kubo Tomita theory of magnetic resonance	27
2.4 Correlation function of the exchange modulation	28
2.5 Spin diffusion	31
2.6 EPR lineshape studies	34
2.7 Temperature dependence of the linewidth of a 2d AFM	36
References cited in Chapter 2	38
3. SOLITON CONTRIBUTION TO THE EPR LINEWIDTH	39
3.1 Introduction	39
3.2 Solitons in 2d Heisenberg magnets	42
3.2.1 Solitons in 2d Antiferromagnets	45
3.2.2 Motivation for the current work	46
3.2.3 Effects of doping with impurities	48
3.2.4 Discreteness of the lattice	49
3.2.5 Calculation of the discrete core energy	50
3.3 EPR linewidth calculation	55
3.3.1 Soliton-Magnon interaction	56
3.3.2 Calculation of the four-spin correlation function	59
3.4 Soliton contribution to the linewidth	63
3.4.1 Calculation of $\langle \cos(\omega t) \rangle$	64
3.4.2 Calculation of $\left\langle \frac{\cos^4 \gamma}{Q^2} \right\rangle$	65
3.4.3 Calculation of the thermal averages	65
3.4.4 Calculation of the terms of the type $\langle f(\mathbf{r}_0) \rangle$	66
3.4.5 Determination of the soliton density	68

3.5 Magnon contribution to the EPR linewidth	70
References cited in Chapter 3	73
4. EPR MEASURING TECHNIQUE AND EXPERIMENTAL DETAILS	76
4.1 Introduction	76
4.1.1 Detection of magnetic resonance	76
4.1.2 Parts of a spectrometer	83
4.2 Description of the investigated sample	85
4.2.1 Crystal structure of PAMC	85
4.2.2 Crystal growth and concentration measurement	87
4.3 Anisotropy measurements	88
4.4 Linewidth measurements	96
4.5 AC susceptibility measurements	109
4.6 X-Ray diffraction measurements	112
References cited in Chapter 4	119
5. RESULTS AND DISCUSSION	121
5.1 Conclusions	135
5.2 Additional work on this problem	136
References cited in Chapter 5	138
Appendices	139
A - Discrete core energy calculation	140
B - Matlab Program	141
C - Calculation of the partition function and $\langle r_0^2 \rangle$	145

## LIST OF TABLES

Table	Page
1. Summary of the anisotropy parameters for the pure and the doped samples of PAMC at $T < 65\text{K}$ , obtained by fitting $(a - b \sin^2 \theta)$ to the linewidth $\Delta H(\theta)$ .	90
2. Measured concentrations and excitation energies for cadmium doped compounds. Excitation energies were obtained from a linear fit to low -T EPR linewidths.	108
3. A summary of the measured concentrations and excitation energies for zinc doped compounds. Excitation energies were obtained from a linear fit to low-T EPR linewidths.	108
4. Measured concentrations and excitation energies for magnesium doped compounds. Excitation energies were obtained from a linear fit to low -T EPR linewidths.	109
5. Powder X-Ray diffraction data table for a sample of pure PAMC showing peak intensities and interplanar spacings.	116
6. Powder X-Ray diffraction data table for a sample of PAMC with some Mg showing peak intensities and interplanar spacings.	118
7. Measured and calculated excitation energies for various manganese compounds.	122
8. A comparison of the calculated soliton energies with the measured energies for cadmium doped compounds.	131
9. A comparison of the calculated soliton energies with the measured energies for zinc doped compounds.	131
10. A comparison of the calculated soliton energies with the measured energies for magnesium doped compounds.	133

## LIST OF FIGURES

Figure	Page
1. Two hydrogen atoms where protons are labelled a and b and electrons are labelled 1 and 2.	3
2. (a) Antiferromagnetic order on a square lattice. (b) Bragg peaks for antiferromagnetic order on a square lattice.	6
3. Two $k = 1$ configurations. (a) $\theta = \phi$ , (b) $\theta = \phi + \pi/2$ .	14
4. The distribution of $\theta$ for one-dimensional solitons: (a) topological (b) nontopological solitons. From Ref 23.	16
5. An EPR absorption line.	26
6. Gaussian and Lorentzian line shapes.	27
7. 2-spin correlation functions in (a) 3-d and (b) low-d magnetic systems. The time scale is defined by the exchange frequency $\omega_e$ .	32
8. Orientation of the spin $\vec{S}$ as a function of $\theta$ and $\phi$ , the polar angles.	42
9. The radial dependence of the polar angle of the spins in a 2d soliton.	43
10. The structure of a two-dimensional topological soliton in a ferromagnet.	44
11. Projection of the spins onto the square lattice at the soliton center. Small circles represent lattice sites.	51
12. A plot of the core energy vs the size parameter $r_0$ . The dotted line represents the curve for the soliton core energy without an impurity at the center. The solid line represents the case of a soliton with an impurity.	53
13(a). A plot of total soliton energy vs $r_0$ . $\circ$ --- represents a plain soliton. $\square$ — represents an impurity pinned soliton. (b). An expanded view of the above plot indicating the critical value of $r_0$ .	54
14. Diagram illustrating the relative angular separation between a magnon, a (pure) P-soliton, and an I-soliton (soliton with an impurity at the center).	59

15. Radial dependence of the structure of a soliton and a neighboring antisoliton.	67
16. Zeeman energy splitting in a magnetic field.	77
17. Lower half of the unit cell of PAMC. Only the carbon atoms of the propyl group are shown.	86
18. Angular variation of the EPR linewidth of pure PAMC at various temperatures.	91
19. Anisotropy of PAMC with some magnesium as an impurity, at various temperatures.	92
20. Anisotropy of PAMC with some cadmium as an impurity, at various temperatures.	93
21. Anisotropy of PAMC with no impurity at $T = 56.4$ K. The dotted line corresponds to the fit of equation 4.15.	94
22. Anisotropy of PAMC with some cadmium at $T = 52.5$ K. The dotted line corresponds to the fit of equation 4.15.	94
23. Anisotropy of PAMC with some magnesium at $T = 58$ K. The dotted line represents the fit of equation 4.15.	95
24. Anisotropy of PAMC with some magnesium at $T = 52$ K. The dotted line represents the fit of equation 4.15.	95
25. Linewidth temperature dependence of a 0.15% Cd doped sample.	97
26. Logarithm of the normalized linewidth vs inverse temperature for a 0.15% Cd doped sample.	98
27. Straight line fit of the logarithm of linewidth vs inverse temperature for a 0.15% Cd doped sample. The solid line is a spline interpretation.	98
28. Straight line fits to the logarithm of normalized linewidth vs $T_N/T$ for three Cd doped compounds and PAMC yielding the soliton excitation energies as slopes. The solid line is a spline interpretation used as a guide to the eye.	99
29. Linear fits to the logarithm of the normalized linewidth vs $T_N/T$ for four Cd doped compounds yielding the soliton excitation energies as slopes. The solid line, a spline interpretation, is a guide to the eye.	100

30. Linear fits of the logarithm of the normalized linewidth vs  $T_N/T$  for two Zn doped compounds and pure PAMC yielding the soliton excitation energies as slopes. The solid line is a spline interpretation used as a guide to the eye. 101
31. Linear fits of the logarithm of the normalized linewidth vs  $T_N/T$  for four Zn doped compounds yielding the soliton excitation energies as slopes. The solid line is a spline interpretation used as a guide to the eye. 102
32. Linear fits of the logarithm of the normalized linewidth vs  $T_N/T$  for four Zn doped compounds yielding the soliton excitation energies as slopes. The solid line is a spline interpretation serving as a guide for the eye. 103
33. Linear fits of the logarithm of the normalized linewidth vs  $T_N/T$  for three Zn doped compounds yielding the soliton excitation energies as slopes. The solid line is a guide to the eye. 104
34. Linear fits of the logarithm of the normalized linewidth vs  $T_N/T$  for three Mg doped compounds yielding the soliton excitation energies as slopes. The solid line is a guide to the eye. 105
35. Linear fits of the logarithm of the normalized linewidth vs  $T_N/T$  for three Mg doped compounds and PAMC yielding the soliton excitation energies as slopes. The solid line is a guide to the eye. 106
36. Linear fits of the logarithm of the normalized linewidth vs  $T_N/T$  for three Mg doped compounds yielding the soliton excitation energies as slopes. The solid line is a spline interpretation serving as a guide for the eye. 107
37.  $\chi$  vs T data for a Mg doped sample showing a sharp transition at  $(39.18 \pm 0.1)K$ . An ac field of frequency 375Hz and amplitude 0.3Oe was applied. 111
38. Powder X-Ray diffraction data for a pure sample of PAMC. 115
39. Powder X-Ray diffraction data for a sample of PAMC doped with some Mg. 117
40. Predicted linewidth versus temperature depicting the contributions from both solitons and magnons in the critical region. The solid curve results from Zaspel's calculation while the dotted curve results from our calculation based on Chakravarty and Orbach's expression for the magnon contribution. 124
41. Logarithm of linewidth vs inverse temperature depicting the soliton and the magnon contributions. Both the linewidth and the temperature have been divided by appropriate units to render the ratio dimensionless. Takahashi's expression has

been used in estimating the correlation length.	125
42. Linewidth versus temperature at various impurity concentrations. Takahashi's expression for the correlation length was used in estimating the linewidth.	126
43. Predicted linewidth versus temperature. CHN's expression for the correlation length was used in estimating the linewidth.	127
44. Logarithm of linewidth versus inverse temperature in the fluctuation region. Takahashi's expression for the correlation length was assumed in the calculation of the linewidth.	128
45. Logarithm of linewidth versus inverse temperature. CHN's expression for the correlation length was used in estimating the linewidth.	129
46. Cadmium doped data compared with theory.	132
47. Zinc doped data compared with theory.	132
48. Magnesium doped data compared with theory.	133

## ABSTRACT

Two dimensional or layered Heisenberg magnets in the classical continuum limit are known to support localized regions of magnetization called solitons. A theoretical and experimental investigation of a two dimensional spin five-halves, Heisenberg antiferromagnet has been conducted. Theoretical calculations that determine how the solitons will affect the temperature-dependent electron paramagnetic resonance (EPR) linewidth have been done. These calculations include the dependence of EPR linewidth on the nonmagnetic impurity concentration. The calculation consists of two parts. The first is the determination of the discrete core energy using simple numerical methods and the energy of the continuum area surrounding the core of the soliton. The second part involves the calculation of the dynamic correlation function performed within the framework of the soliton-magnon interaction picture. One of the most significant effects indicated by the above calculations is the large change in the EPR linewidth with very small amounts of doping nonmagnetic impurity atoms. The magnon contribution to the temperature dependent linewidth was calculated by extending the calculations of Chakravarty and Orbach for a quantum Heisenberg antiferromagnet. It was found to be rather insignificant when compared to the soliton contribution in the same temperature range.

We have investigated the possible effects of doping (n propylammonium)<sub>2</sub>Mn<sub>1-x</sub>M<sub>x</sub>Cl<sub>4</sub>, a quasi two-dimensional antiferromagnet with  $S = 5/2$ , where M = Cadmium, Zinc or Magnesium. The nonmagnetic impurities are present in very small molar quantities well below the percolation limit. Very good qualitative agreement between the observed linewidth temperature dependence and the above theory indicate that solitons indeed contribute to the thermodynamic behavior of layered magnetic compounds. A quantitative comparison of the soliton excitation energies as a function of impurity concentration reveals good agreement between theory and experiment.

## CHAPTER 1

## 1. INTRODUCTION

Over the last few decades, nonlinear effects have had far reaching influence and consequences in the various branches of mathematics, physics and engineering. The idea of the nonlinear effects as a 'unifying tool' in physics is a well-established notion by now.

In the last twenty years or so, the exponential growth in soliton research<sup>1,2</sup> can be attributed to the diversity of its applications and the availability of high speed computers. Soliton theory finds wide applications in some of the branches of contemporary physics such as phase transitions, statistical mechanics, quantum liquids, low-dimensional magnetism -- to name a few. Soliton-bearing systems are very popular among theorists, because of the complete integrability of the Hamiltonian systems from which they derive. During the same time soliton research was gaining ground, low dimensional magnetism has matured into a very important branch of physics. Low-d magnets serve as good model systems in solid-state physics both in theory and experiment.

The motivation for the current thesis, which constitutes an investigation of the effect of the soliton dynamics on the thermodynamics of a two-dimensional layered magnet, stems from two factors. Firstly the discovery of a series of Cu-layered oxides with extremely high superconducting transition temperature  $T_C$ , has provided a new impetus to the research activity in low-d, in particular 2d magnetism. This new class of materials, in addition to being the highest  $T_C$  superconductors, also happens to be the best models for 2d antiferromagnets (AFM). Secondly, in view of the exhaustive mathematical information available for soliton-bearing systems, they offer rare soluble

models. However experimental evidence for the existence of solitons has been slower in coming.

Insulating magnetic compounds are the most popular magnetic systems in the experimental studies of low-d magnetism. This branch of physics and solid-state chemistry has been well developed in the last twenty years or so<sup>3,4,5,6</sup>. The reduced spatial dimensionality is brought about in these compounds by the insertion of large alkyl groups between magnetic chains (in the 1d case) and between layers (in the 2d case) thus limiting the atomic orbital overlap which determines the long-range order in such systems. The restricted dimensionality offers analytic tractability, thus rendering them ideal vehicles for testing theories of magnetism. In addition nature provides a large variety of compounds which can be described as quasi-low dimensional. The study of low-d magnets is important, particularly in the context of critical phenomena and second-order phase transitions. Theoretical work on the statistical mechanics of the 1d Ising chain<sup>7</sup>, followed by the studies of 2d Ising magnets<sup>8</sup>, and its various exact solutions<sup>9</sup> are only a few examples which illustrate this fact. For 1d Heisenberg AFM, the exact ground state has been given by Bethe<sup>10</sup> and has led to a whole set of exactly solvable  $S = 1/2$  chain Hamiltonians.

The following is a survey of the physics relevant to the understanding of the material that will be presented in the subsequent chapters.

### 1.1 HEITLER-LONDON MODEL OF THE HYDROGEN MOLECULE<sup>11</sup>

The simplest example for demonstrating the effective interaction between two

neutral atoms, as a function of the radial distance of separation between them, is two hydrogen atoms. The interaction Hamiltonian from such a system is given by,

$$H = H_0 + H' \quad (1.1)$$

$$H_0 = \frac{\hbar^2}{2m} (\nabla_1^2 + \nabla_2^2) - \frac{e^2}{r_1} - \frac{e^2}{r_2} \quad \text{where } m \text{ is the electron mass.}$$

The Hamiltonian  $H'$  includes the Coulomb attraction between each proton and the opposite electron and the Coulomb repulsion between the protons and the electrons.

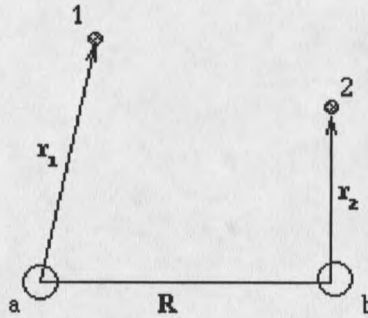


Figure. 1. Two hydrogen atoms where protons are labelled a and b and electrons are labelled 1 and 2.

$$H' = \frac{e^2}{R} + \frac{e^2}{r_{12}} - \frac{e^2}{r_{1b}} - \frac{e^2}{r_{2a}} \quad (1.2)$$

$R = |\mathbf{R}|$  is the separation between protons.

$r_{12} = |\mathbf{R} + \mathbf{r}_2 - \mathbf{r}_1|$  is the separation between the electrons.

$r_{1b} = |\mathbf{r}_1 - \mathbf{R}|$  and  $r_{2a} = |\mathbf{R} + \mathbf{r}_2|$  are the separations between the electron and the opposite nuclei.

The solution to  $H_0$  can be obtained by letting  $H' = 0$ , and by using a product of

hydrogen wavefunctions on the non-interacting atoms.

Let  $\phi_n(\mathbf{r})$  be the eigenfunction of the single hydrogen atom with energy

$$E_n = -\frac{me^4}{2\hbar^2 n^2} \quad (1.3)$$

The eigenfunctions of  $H_0$  are

$$\psi_p(1,2) = \phi_n(\mathbf{r}_1)\phi_m(\mathbf{r}_2),$$

$$\psi_p(2,1) = \phi_n(\mathbf{r}_2)\phi_m(\mathbf{r}_1) \quad \text{with a two-fold degeneracy.}$$

If we let the protons move closer together, the Pauli exclusion principle requires that the two electron wavefunctions be properly antisymmetrized with respect to the interchange of electrons which may be represented as,

$$\psi(\mathbf{r}_1, \mathbf{s}_1; \mathbf{r}_2, \mathbf{s}_2) = -\psi(\mathbf{r}_2, \mathbf{s}_2; \mathbf{r}_1, \mathbf{s}_1) \quad (1.4)$$

where we now explicitly include the electron spins  $\mathbf{s}_1$  and  $\mathbf{s}_2$ . With no spin-orbit coupling, the spin and position variables can be separated.

$$\psi(\mathbf{r}_1, \mathbf{s}_1; \mathbf{r}_2, \mathbf{s}_2) = \psi(\mathbf{r}_1, \mathbf{r}_2)\chi(\mathbf{s}_1, \mathbf{s}_2) \quad (1.5)$$

The Pauli principle requires that spin functions be antisymmetric if the spatial function is symmetric under interchange of electrons and vice versa.  $\psi$  thus has a spin singlet (s) and a spin triplet (t) part.

$$\psi_s(1, 2) = \frac{1}{\sqrt{2}} [\phi_n(\mathbf{r}_1)\phi_m(\mathbf{r}_2) + \phi_m(\mathbf{r}_1)\phi_n(\mathbf{r}_2)]\chi_s(\mathbf{s}_1, \mathbf{s}_2) \quad (1.6)$$

$$\psi_t(1, 2) = \frac{1}{\sqrt{2}} [\phi_n(\mathbf{r}_1)\phi_m(\mathbf{r}_2) - \phi_m(\mathbf{r}_1)\phi_n(\mathbf{r}_2)]\chi_t(\mathbf{s}_1, \mathbf{s}_2) \quad (1.7)$$

This particular form of the wavefunction is due to the Heitler-London approach.

It does not allow two electrons to occupy the same site and therefore has a built-in

correlation that reduces the Coulomb repulsion between electrons. In this problem, only the spin variables affect the energies of our problem. In order to estimate the singlet-triplet splitting, lowest order perturbation theory is used resulting in,

$$\Delta E_{s,t} = \frac{Q \pm J}{[1 + \beta^2]} \text{ where } \beta = \int \rho_{ab}(1) d^3 x_1 \text{ and } \rho_{ab}(1) = \phi_a^*(1)\phi_b(1),$$

and  $\beta$  is known as the overlap integral.

We also define charge densities of the unperturbed atomic orbitals as

$$\rho_a(1) = \phi_a^*(1)\phi_a(1) \text{ and } \rho_b(2) = \phi_b^*(2)\phi_b(2)$$

$Q$  is defined as the *Coulomb integral* which represents the interaction between the time average charge cloud on separate unperturbed atoms.  $J$  is known as the *exchange integral* which appears as the result of the symmetry of the spatial wavefunctions under interchange of electrons they are written as,

$$Q = \frac{e^2}{R} + \int \rho_a(1) \frac{e^2}{r_{12}} \rho_b(2) d^3 x_1 d^3 x_2 - 2 \int \rho_b(2) \frac{e^2}{r_{a2}} d^3 x_2, \text{ and} \quad (1.8)$$

$$J = \int \rho_{ab}(1) \frac{e^2}{r_{12}} \rho_{ab}(2) d^3 x_1 d^3 x_2 - 2\beta \int \rho_{ab}(1) \frac{e^2}{r_{b1}} d^3 x_1. \quad (1.9)$$

Thus the interesting result from the study of molecular hydrogen is the presence of a spin-dependent interaction of a magnitude given by the electrostatic forces. The *exchange integral*  $J$  is  $\approx 3 - 4$  eV in the case of hydrogen, and it arises from the symmetry requirements of the total wavefunction. Most magnetism found in nature is due to this exchange interaction.

## 1.2 MAGNETIC ORDER

In this section we introduce the concept of magnetic order which leads to an understanding of the systems such as a Heisenberg antiferromagnet which is the sample system studied in this work. For the simple case the spin-interaction alone can be written as,

$H_{\text{spin}} = -JS_1 \cdot S_2$  and can be generalized for all pairs of neighboring spins as

$$H_{\text{spin}} = - \sum_{i \neq j} J_{ij} S_i \cdot S_j \quad (1.10)$$

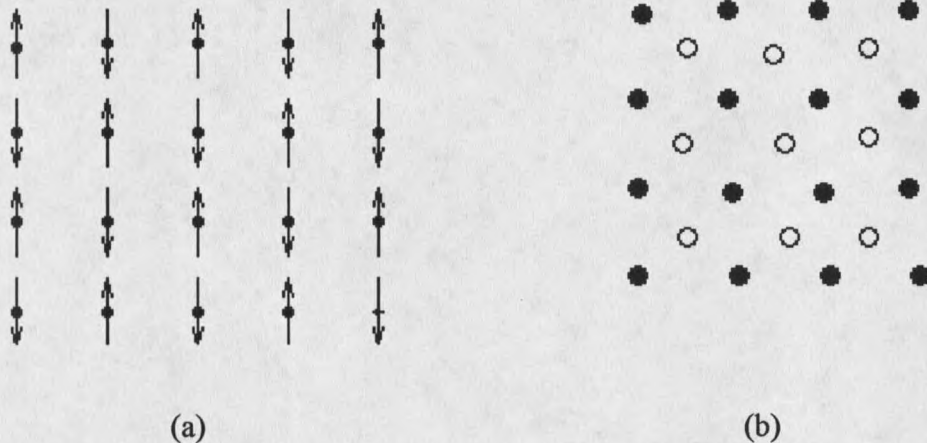


Figure 2. (a) Antiferromagnetic order on a square lattice. (b) Bragg peaks for antiferromagnetic order on a square lattice.

In magnetic materials at low enough temperatures interactions among spins lead to ordered structures, and if they prefer to be parallel, (as they do if  $J$  is positive) then a ferromagnetic phase results. If the neighboring spins prefer to be antiparallel, (when  $J$  is negative) then an antiferromagnetic phase results. The detailed form of the AFM order depends upon the lattice. On lattices, such as the square lattice in 2d that can be decomposed into two equivalent sublattices; the ordered state will consist of up spins in one

sublattice and down spins in the other. The development of AFM order leads to an increase in the size of the unit cell, and therefore, to new magnetic Bragg peaks, and a reduced size of the unit cell in reciprocal space. Furthermore in AFM an external magnetic field  $h$  does not destroy the long-range order when  $h$  is sufficiently small.

A complete description of the above mentioned ordered phases requires an introduction of a new variable quantifying the degree of order. It also requires the modification of the thermodynamics and statistical mechanics to describe the effects of these variables on free energies and entropies of the magnetic system. At low enough temperatures, even in zero magnetic field, it is possible for magnetic systems to have a spontaneous magnetization or a non-zero  $\langle m \rangle$ . This is the *order parameter* of a ferromagnetic state.

Depending upon the number of components,  $n$ , ( $x$ ,  $y$ ,  $z$ ) of the spins that are considered, one has a one-, two-, or three component spin system. The number  $n$  is called the spin-dimensionality, which is distinct from the lattice dimensionality  $d$ . Depending upon the number of combinations of the components  $J_x$ ,  $J_y$ ,  $J_z$  there may also be a variety of models, such as Ising, XY and Heisenberg models.

The Heisenberg Hamiltonian is the same as the one represented by eqn. (1.10). It is invariant with respect to an arbitrary rotation of all the spins  $S_i$ . All the spins in the ground state of a Heisenberg Ferromagnet are along the same direction, and acquire their maximal values. The ground state of a Heisenberg Antiferromagnet has not yet been found analytically. A generalized Heisenberg model may be represented by the Hamiltonian

$$H = -2J_{\parallel} \sum_{\langle ij \rangle} S_i^z S_j^z - J_{\perp} \sum_{\langle ij \rangle} [S_i^- S_j^+ + S_i^+ S_j^-] \quad (1.11)$$

The case in which we are interested in this thesis is the isotropic, antiferromagnetic, Heisenberg model wherein,  $J_{\parallel} = J_{\perp} = J < 0$ . The order parameter is the staggered magnetization

$$\mathbf{N} = N_0 \hat{\mathbf{n}} \quad \text{with} \quad \hat{N}(\mathbf{x}) = \sum_i \eta_i S_i \delta(\mathbf{x} - \vec{R}_i)$$

where  $\eta_i = +1$  if  $i$  is a site in sublattice A and

$$\eta_i = -1 \text{ if } i \text{ is a site in sublattice B.}$$

$S = \sum_i S_i$  commutes with  $H$  and all the three components of magnetization are conserved.

### 1.3 LONG RANGE ORDER IN LOW-DIMENSIONAL SYSTEMS

The concept of exchange can be extended to include interactions throughout the crystalline lattice (as opposed to nearest neighbor interactions only, as in a Heisenberg magnet). It is useful to define a pair-correlation function  $C(r, T) = \frac{\langle S_0^z S_r^z \rangle}{3S(S+1)}$  to describe the thermodynamic behavior of a low-d system<sup>11</sup>. We consider only the z-component of the spins for convenience. Above  $T_C$ ,  $C(r, T)$  decreases rapidly with increasing  $r$ , reflecting the short-range order (SRO) present in the magnetic system. As  $T_C$  is approached from above the correlation length that characterizes the degree of correlation between different spins at a particular temperature, will gradually increase until it diverges at  $T_C$ , signalling the onset of long-range order (LRO). Thus long-range

order can be understood as nonzero correlations between spins that are arbitrarily far apart. In a real time situation even though the interactions are not long range, the effects are observed over large distances. Transitions to such long-range order are characterized by both characteristic specific heat anomalies and susceptibility anomalies at the temperature  $T_C$ . Both the lattice dimensionality  $d$  and the spin-dimensionality  $n$  have a profound influence on the critical behavior of many-body systems. A question of primary importance is the presence or absence of long-range order (LRO) below some finite temperature  $T_C$ . For any value of  $n$ , 3d systems can exhibit long-range order, whereas in 1d systems a transition to LRO can occur only at absolute zero regardless of spin dimension. In the following section we shall discuss some specific examples of low- $d$  systems which exhibit long-range order<sup>12</sup>.

Landau's argument from a statistical standpoint, about the absence of LRO in 1d Ising chains, is quite transparent<sup>13</sup>. The Hamiltonian which represents a 1d Ising chain with free ends is  $H_{\text{Ising}} = -2J \sum_i S_i^z S_{i+1}^z$ , with the ground state energy  $E = -(N-1)J$  for  $N$  spins. The reversal of a spin causes a kink in the ordered chain with an energy cost of  $2J$ . Since this kink may be placed in any one of the  $N$  sites, the corresponding change in entropy is  $k_B \ln(N)$ . Thus the free energy change due to these excitations is  $\Delta F = 2J - k_B \ln(N)$  which is less than 0 for all  $T > 0$  for a large enough  $N$ . The chain therefore breaks up into smaller segments or domains which minimizes the free energy, thus yielding approximately  $e^{2J/k_B T}$  for the correlation length.

The correlation functions that are mentioned above are used to describe static behavior. Time-dependent correlation functions are used to describe the frequency-

dependent effects as in NMR, EPR and neutron diffraction.

The formation of domains in 1d systems, in order to minimize the free energy, indicates that short-range order (SRO) is present in magnetic systems above  $T_C$ . There are few exact solutions available for the Heisenberg model. Numerical calculations, however, are available which characterize the Heisenberg behavior to a fair degree of accuracy, particularly in 1-d<sup>14,15</sup>. For a 1d Heisenberg model, the correlation length is of the form  $R(T) \approx aJ/k_B T$  which has been experimentally observed for the 1d Heisenberg model TMMC<sup>16</sup>.

The important calculation for the 2d Ising model, for a  $S = 1/2$  system was first done by Onsager<sup>8</sup>. Applying the free energy-entropy considerations to a 2d square lattice of Ising spins, the transition temperature is found to be  $T_C = 2J/k_B \ln 3$ . The system is stable against domain formation for  $T < T_C$ , but above this temperature domains will form destroying the LRO. The exact transition temperature<sup>8</sup> is  $T_C = 2J/k_B \ln(1 + \sqrt{2})$ .

A more sophisticated version of this type of argument was first proposed by Peierls<sup>17</sup> to prove that in a 2d Heisenberg model, phase transitions do not occur. The absence of order at any finite temperature in a 2d Heisenberg model, has been proved by Mermin and Wagner<sup>18</sup>. A 2d XY model is distinct from the other models. It has no transition to LRO in the conventional sense, i.e, a temperature below which the order parameter diverges cannot be defined; yet there exists a finite temperature at which the susceptibility diverges in an exponential fashion. According to Kosterlitz, Thouless, and Berezinskii<sup>19,20</sup> this transition corresponds to the unbinding of the vortex - antivortex pairs, that exist in these systems below the ordering temperature  $T_{KT}$ .

The molecular field (MF) theory offers a remarkably good approximation to the qualitative behavior of phase transitions in 3d magnets. It, however, completely fails for low-dimensional magnets, since it fails to take into account SRO effects. In MF theory, the magnetic interaction of a given spin with its  $z$  nearest neighbors is replaced by an average interaction with all the other spins in the lattice. MF theory predicts a transition to LRO regardless of the lattice-dimensionality, which is not true for low-d systems. Even for systems that show LRO the MF theory becomes inadequate near the critical point. The fluctuations that are not accounted for in this theory become more important in models such as Ising and Heisenberg.

There will always be some weak interchain and interlayer interactions present in the experimental approximations to low-d systems that we encounter in real life. Of prime concern is, how the thermodynamic properties of these quasi low-d systems will be affected by these interactions. The 3-d order in a low-d system is basically driven by the divergence of the correlation length in the low-d system as one approaches  $T_C$  from above. The weak interchain or interlayer interactions, however small, allow correlations to propagate in three dimensions, thus allowing a 'crossover' to 3d behavior at low enough temperatures. An interesting question is whether the critical behavior close to transition merely reflects the 3d character of real layer type systems or whether it still represents specific 2d properties.

The thermodynamic behavior of low-d magnets is fundamentally different from those of their 3d counterparts because of the SRO effects that precede the onset of LRO. In order to discuss these effects it is useful to distinguish among three

temperature regimes. (a) When  $T \gg T_C$ , the magnetic systems are marked by random thermal fluctuations and precise estimates of the 'low-d' critical properties can be obtained. (b) The temperature region immediately above  $T_C$  is termed the fluctuation or critical regime which is determined by  $n$ ,  $d$  and the strengths of the exchange constants. This region may be further subdivided into a SRO region for the higher temperature and the crossover region where 3d effects begin to arise. Effects of SRO on the temperature dependence of the spin-correlations in the critical region of a 2d layered magnet will be the focus of the current work, rather than the crossover to 3d. (c) The temperature regime  $T \ll T_C$ , is where the system is ordered in 3d, where spin-wave type excitations dominate the thermodynamics.

From the above discussion it is evident that a molecular field approach is inadequate to describe co-operative phenomena in low-d systems. One has to resort to more realistic models such as Ising, XY, and Heisenberg. Unfortunately because of the mathematical difficulties involved, exact results for these models are not available except for the 1d case and the 2d Ising model. For 3d models our knowledge of thermodynamic behavior is based on approximation techniques, such as high temperature series expansions, scaling theory and renormalization group for critical behavior. However, in low-d systems information about the spin dynamics in the non-ordered region could be obtained. For the 2d XY and Heisenberg models it is well known that the low-amplitude excitations are spin waves. Other large amplitude fluctuations present in these systems are nonlinear excitations like kinks, solitons and skyrmions. In the following section the concept of topological excitations is introduced which is pertinent to the theory

developed in Ch. 3.

#### 1.4 TOPOLOGICAL EXCITATIONS

In recent years the study of nonlinear excitations such as vortices and solitons has enjoyed a vivid interest among theorists as well as experimentalists. While spin waves are the simplest type of excitations found in 2d systems that play an important role in the phase transitions of these systems, the contribution of these nonlinearities, classified as 'fluctuational excitations', cannot be ignored. Quasi-order in the XY model results from spin-waves and vortices which are topological excitations confined below a certain temperature. In the Heisenberg model vortices are prohibited; however, another type of topological excitation called a 'soliton' is allowed. This section is devoted to a discussion of these defects in magnetic systems.

Topological excitations are defects or distortions from a ground state configuration. These distortions arise from the imposition of boundary conditions, from external fields, or from thermal fluctuations. A general description of a topological defect is as follows. It can be characterized by some core region where order is destroyed, and a far field region where an elastic variable changes slowly in space. In order to elucidate the concept of topological defects we shall consider the example of a vortex in the XY-model. The order parameter that breaks the continuous symmetry of rotations in the xy-plane is a two-dimensional vector  $\langle \mathbf{s} \rangle = s(\cos\theta, \sin\theta)$  whose phase is specified by the angle  $\theta$ . The spin  $\langle \mathbf{s}(\mathbf{x}) \rangle = s(\cos\theta(\mathbf{x}), \sin\theta(\mathbf{x}))$  is a periodic function of  $\theta(\mathbf{x})$  and it is possible to have situations in which  $\mathbf{s}(\mathbf{x})$  is continuous everywhere in d-dimensional space. For

possible to have situations in which  $\mathbf{s}(\mathbf{x})$  is continuous everywhere in  $d$ -dimensional space. For example, if  $d = 2$  and  $\theta(\mathbf{x}) = \phi + \theta_0$ , where  $\theta_0$  is any constant and  $\mathbf{x} = (r, \phi)$  in polar co-ordinates, then  $\langle \mathbf{s}(\mathbf{x}) \rangle$  is continuous and  $\nabla\theta = 1/r$  is finite everywhere except at the origin, as shown in the figure. This configuration of spins defines a vortex. The angle  $\theta$  changes by  $2\pi$  in one circuit of any closed contour enclosing the vortex located at the origin.

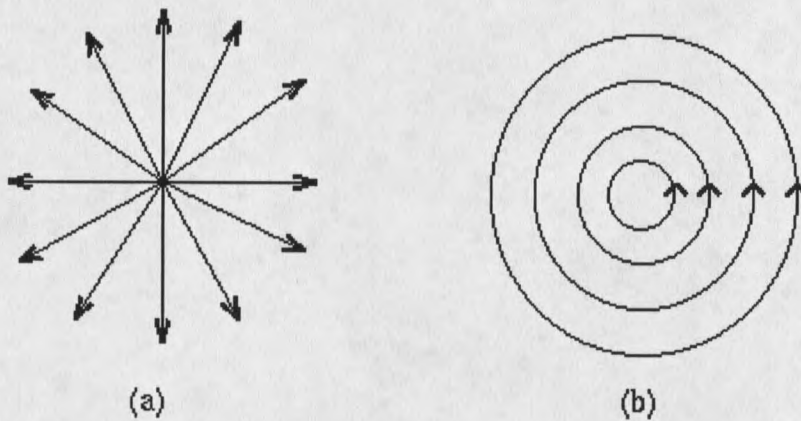


Figure 3. Two  $k = 1$  configurations. (a)  $\theta = \phi$ , (b)  $\theta = \phi + \pi/2$ .

Since  $\langle \mathbf{s}(\theta) \rangle = \langle \mathbf{s}(\theta + 2k\pi) \rangle$  for  $k = 0, \pm 1, \pm 2, \dots$ , there are an infinite number of distinct singularities in which  $\theta$  increases by  $2k\pi$  in one complete circuit of the core. The integer  $k$  is called the *winding number*, or the *strength*, of the vortex. Spin configurations for a few cases of low  $k$  values are shown in figure 3.

Defects such as vortices are important because they cannot be made to disappear by any continuous deformation of the order parameter. They are therefore called *topological defects*. In the  $k = 1$  vortex, spins rotate through  $2\pi$  along every contour enclosing the core. It is therefore impossible to distort the spin configuration of a  $k = 1$

vortex into that of a perfectly aligned state without tampering with the spins. The  $k = 1$  vortex is thus said to be *topologically stable*. Topological stability is a mathematical concept distinct from physical stability, which depends on free energies of different configurations. In most cases, however, topological stability implies physical stability.

The possible occurrence of nonlinear excitations in 2d systems was first introduced by Skyrme<sup>21</sup>. They were first referred to as *skyrmions*, after Skyrme who first invented them, but later came to be known as solitons. Magnetic solitons are localized solutions of dynamic equations of magnetization characterized by the boundary conditions,  $\theta = 0$  at  $r = \infty$  and  $\theta = \pi$  at  $r = 0$ . Here  $\theta$  is the polar angle and  $\phi$  the azimuthal angle, on the unit sphere. The solution for the 2d solitons was derived by Belavin and Polyakov<sup>22</sup> in a novel and elegant fashion. According to them, each point of the lattice plane or its spherical projection has its conformal mapping  $\tan(\theta/2) = r/r_0$  of the unit sphere, where  $r$  is the distance of the spin from the center with an arbitrary measure  $r_0$  of the width. The quantity  $r_0$  has the meaning of an excitation radius.

We can distinguish between two types of solitons namely, dynamic or nontopological soliton and topological solitons. A dynamic soliton can be reduced to a uniform magnetization by continuous deformation so that the excited ferromagnet makes a transition to the ground state. A topological soliton represents an inhomogeneous state of magnetization which cannot be reduced to a ground state by any finite deformation. Kosevich *et al.*, defined a topological invariant  $Q$  called the *topological charge* which indicates the mapping degree. This is an integer, corresponds to  $k$  of the vortex, which shows how many times the sphere in the spin space is covered in the course of the

mapping. The  $Q = 0$  soliton is topologically equivalent to the ground state and does not contain any topological charge.

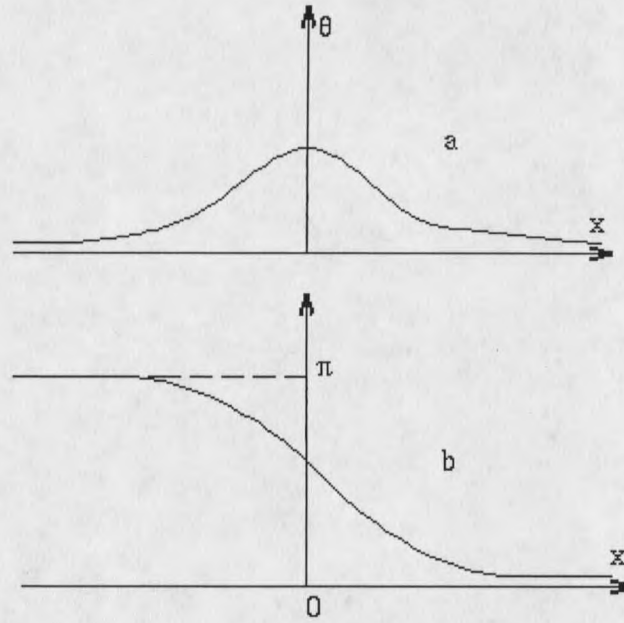


Figure 4. The distribution of  $\theta$  for one-dimensional solitons: (a) topological (b) nontopological solitons. From Ref 23.

We can define an antisoliton the same way as a soliton. In these excitations the vector  $\mathbf{S}(\mathbf{r})$  rotates in the opposite direction in an azimuthal plane and corresponds to a mapping  $\tan(\theta/2) = r_0/r$  of the unit sphere. In contrast to magnetic vortices, which always occur as vortex-antivortex pairs, single solitons may arise, which suppress long range order in Heisenberg magnets. In 2d systems solitons may form complicated line-patterns, and since they contain a finite energy, may be thermally excited. The energy of an excitation<sup>23</sup> is finite and equals to  $4\pi JS^2$  independent of  $r_0$ . The energy of an arbitrary solution with the mapping degree  $Q$  is equal to  $4\pi QJS^2$ . Such a solution can be interpreted as  $Q$  non-interacting solitons. The soliton density may be

estimated as  $n \approx \exp(4\pi|JS^2|/k_B T)$ , which is negligible at very low temperatures. At higher temperatures, close to  $T_C$ , solitons may be excited thermally. It will be of interest to explore to what extent these excitations are important for the thermodynamic behavior of 2d systems. It is with this goal in mind, that the current investigations were done. They have strengthened our belief that the nonlinear excitations play a dominant role in the spin dynamics of 2d systems.

## REFERENCES CITED IN CHAPTER 1

1. "Solitons in action", eds. K. Lonngren and Alwyn Scott, Academic Press, NY, 1978.
2. "Solitons", eds. S.E. Trullinger, V.E. Zakharov, and V.L. Pokrovsky, North Holland, Amsterdam, 1986.
3. "Experiments on Simple magnetic Model Systems", L.J. de Jongh and A.R. Miedema, Taylor and Francis monographs in Physics, (1974).
4. L.J. de Jongh, *J. Appl. Physics*, **49** (1978) 1305; and in "Recent Developments in Condensed Matter Physics", J.T. Devreese, ed. vol. I Plenum Press (1981).
5. "Magneto-Structural Correlations in Exchange Coupled Systems", Italy (1983), R.D. Willett, G. Gatteschi and O. Kahn, eds, Reidel (1985).
6. "Organic and Inorganic Low-Dimensional Crystalline Materials", Spain (1987), eds. P. Delhaes, and M. Drillon, Plenum (1987).
7. E. Ising, *Z.Phys.* **31**, 253 (1925).
8. L. Onsager, *Phys. Rev.* **65**, 117 (1944).
9. "Exactly Solved Models in Statistical Mechanics", R.J. Baxter, Academic Press, London, 1982.
10. H.E. Bethe, *Z. Phys.* **71**, 205 (1931).
11. "Principles Of Condensed Matter Physics", P.M. Chaikin, and T.C. Lubensky, Cambridge Press, 1995.
12. "Magnetic Properties of Layered Transition Metal Compounds", ed. L.J. de Jongh, Kluwer, Dordrecht, The Netherlands, 1990.
13. L.D. Landau and E.M. Lifshitz, "Statistical Physics", Pergamon Press, 482 (1958).
14. J.C. Bonner and M.E. Fisher, *Phys.Rev.* **135**, A640, (1964).
15. H.W.J. Blöte, *Physica*, **78**, 302 (1974); T. de Neef, A.J.M. Kuipers, and K. Kopinga, *J. Phys.*, **A7**, L171 (1974).
16. M.T. Hutchings, G. Shirane, R.J. Birgenau, and S.L. Holt, *Phys.Rev.* **B5**, 1999, 1972.

17. R. Peierls, *Helv. Phys. Acta*, *VII*, *Suppl. 2*, 81 (1936).
18. N.D. Mermin and H. Wagner, *Phys.Rev.Lett.*, **17**, 1133 (1966).
19. V.L Berezinskii, *Sov. Phys. JETP*, **32**, 493 (1971); V.L Berezinskii, and Y. Ya. Blank, *Sov. Phys. JETP*, **37**, 369 (1973).
20. J.M. Kosterlitz, and D.J. Thouless, *J. Phys. C.*, **6**, 1181 (1973); J.M. Kosterlitz, *J. Phys. C.*, **7** 1046 (1974).
21. T.H.R. Skyrme, *Proc. Roy. Soc. A***247**, 260 (1958).
22. A. A. Belavin, A. M. Polyakov, *Pis'ma v ZhETF* **28**, 503 (1975) [*JETP* **22**, 245 (1975)].
23. A.M. Kosevich, B.A. Ivanov, and A.S. Kovalev, *Sov. Sci. Rev. A Phys.* **6**, 161 (1985); A.M. Kosevich, B.A. Ivanov, and A.S. Kovalev, *Phys. Rep.* **194**, 119 (1990).

## CHAPTER 2

## SURVEY OF THE THEORY OF EPR

## 2.1 RELAXATION FUNCTION AND DYNAMIC SUSCEPTIBILITY

The purpose of the resonance theory described in this chapter is to study the behavior of a paramagnetic system under the influence of a constant and an oscillating magnetic field. In linear response theory, the response of the magnetization of  $\delta\vec{M}(t)$  to an external disturbance  $\delta\vec{H}(t')$  is given by<sup>1</sup>

$$\begin{aligned}\delta\vec{M}(t) &= \int_{-\infty}^t \left[ \frac{d}{dt'} \phi(t-t') \right] \cdot \delta\vec{H}(t') dt' \quad (t > t') \\ &= - \int_0^{\infty} \dot{\phi}(\tau) \cdot \delta\vec{H}(t-\tau) d\tau\end{aligned}\quad (2.1)$$

which defines the second rank tensor  $\phi(t)$  known as the relaxation function, apart from a constant. The function  $\phi(t)$  is usually chosen such that,

$$\phi(\infty) = \int_0^T \phi(t') dt' = 0. \quad (2.2)$$

Partial integration of eq.(2.1), under the assumption that  $\delta\vec{H}(-\infty) = 0$ , leads to

$$\delta\vec{M}(t) = \phi(0) \cdot \delta\vec{H}(t) - \int_0^{\infty} \dot{\phi}(\tau) \cdot \delta\vec{H}(t-\tau) d\tau \quad (2.3)$$

If the Fourier transform of  $\delta\vec{H}(t)$  exists, i.e

$$\delta\vec{H}(t) = \frac{1}{2\pi} \int_{-\infty}^{\infty} e^{i\omega t} \delta\vec{H}(\omega) d\omega,$$

then equation (2.3) can be written as

$$\delta\vec{M}(t) = \frac{1}{2\pi} \int_{-\infty}^{\infty} e^{i\omega t} \chi(\omega) \cdot \delta\vec{H}(\omega) d\omega \quad (2.4)$$

In this equation, the frequency dependent complex susceptibility per unit volume  $\chi(\omega)$ , is defined as

$$\chi(\omega) = \phi(0) - i\omega \int_0^{\infty} \phi(t) e^{-i\omega t} dt \quad (2.5)$$

which is also a second rank tensor. For the discussion of the EPR experiments in which a linearly polarized oscillating field is used, it is sufficient to consider only diagonal elements.

Separating  $\chi$  into a real part  $\chi'$  (dispersion) and an imaginary part  $\chi''$  (absorption), such that  $\chi = \chi' - i\chi''$ , one obtains

$$\chi'(\omega) = \phi(0) - \omega \int_0^{\infty} \sin \omega \tau \phi(\tau) d\tau \quad (2.6)$$

$$\chi''(\omega) = \omega \int_0^{\infty} \cos \omega \tau \phi(\tau) d\tau \quad (2.7)$$

where we have used the fact that  $\phi(t)$  is real. Furthermore,

$$\chi(0) = \chi'(0) = \phi(t=0) \quad (2.8)$$

where  $\chi(0) = \chi_0$  is the static susceptibility.

As  $\chi'$  and  $\chi''$  can both be expressed in terms of  $\phi(t)$ , they are directly related to each other (Kramers-Kronig relations)

$$\chi'(\omega) - \chi''(\infty) = P \int_{-\infty}^{\infty} \frac{\delta\omega'}{\pi} \frac{\chi''(\omega')}{(\omega - \omega')} \quad (2.9)$$

$$\chi''(\omega) = P \int_{-\infty}^{\infty} \frac{\delta\omega'}{\pi} \frac{\chi'(\omega') - \chi'(\infty)}{(\omega - \omega')} \quad (2.10)$$

Here the symbol P stands for the Cauchy principal value of the integral. It can be shown, that in the case of an oscillating disturbance  $\delta H(t) = H_1 \cos \omega t$ , the rate of work done by this field obeys<sup>2</sup>

$$\frac{dW}{dt} = \frac{1}{2} \omega \chi''(\omega) H_1^2 \quad (2.11)$$

Starting from eqn (2.1), the following expression for the elements of  $\phi(t)$  can be derived

$$\phi^{\mu\nu}(t) = \int_0^{\infty} d\lambda \left\langle \left\langle e^{\lambda \mathcal{H}} M^{\nu} e^{-\lambda \mathcal{H}} M^{\mu}(t) \right\rangle \right\rangle - \beta \left\langle \left\langle M^{\mu} \right\rangle \right\rangle \left\langle \left\langle M^{\nu} \right\rangle \right\rangle. \quad (\mu, \nu = x, y, z) \quad (2.12)$$

In this expression,  $M^{\mu}(t)$  describes the time-evolution of  $M^{\mu}$  in the absence of the external disturbance (natural motion) :

$$M^{\mu}(t) = \exp\left(\frac{i}{\hbar} \mathcal{H} t\right) M^{\mu} \exp\left(-\frac{i}{\hbar} \mathcal{H} t\right) \quad (2.13)$$

The equilibrium Hamiltonian is denoted by  $H$ ; double brackets denote the equilibrium expectation value

$$\langle\langle M^{\mu} \rangle\rangle = \text{Tr} [ \exp(-\beta \mathcal{H}) M^{\mu} ] / \text{Tr} [ \exp(-\beta \mathcal{H}) ] \quad (2.14)$$

and  $\beta \equiv 1/kT$ . The second term in the right hand side of eqn. (2.12) serves to meet the condition expressed by eqn. (2.2). Defining an inner product of operators A and B as

$$\langle A, B \rangle = \beta^{-1} \int_0^{\beta} d\lambda \langle\langle e^{\lambda \mathcal{H}} A e^{-\lambda \mathcal{H}} B \rangle\rangle \quad (2.15)$$

one can rewrite equation (2.12) as

$$\phi^{\mu\nu}(t) = \beta \langle M^{\nu}, M^{\mu}(t) \rangle. \quad (2.16)$$

Formally, a quantum mechanical correlation function between  $M^{\mu}(t)$  and  $M^{\nu}$  is defined as:

$$G^{\mu\nu}(t) = \left\langle \left\langle \{ M^{\nu}, M^{\mu}(t) \} \right\rangle \right\rangle \equiv \left\langle \left\langle \frac{1}{2} ( M^{\mu}(t) M^{\nu} + M^{\nu} M^{\mu}(t) ) \right\rangle \right\rangle \quad (2.17)$$

From equations (2.7), (2.12), and (2.17) one can derive<sup>1</sup>

$$\frac{\chi''(\omega)}{\omega} = \frac{1}{\hbar\omega} \text{tgh} \frac{\beta\hbar\omega}{2} G(\omega) \quad (2.18)$$

in which relation  $G(\omega)$  is defined as

$$G(\omega) = \int_{-\infty}^{\infty} dt e^{-i\omega t} G(t) \quad (2.19)$$

Once again only diagonal elements are considered; equation (2.18) represents the fluctuation-dissipation theorem, which relates the absorption in the presence of an external disturbance to the equilibrium fluctuations of the system, expressed by  $G(t)$ .

In the high -temperature approximation,  $\hbar\omega \ll kT$ , eq (2.18) reduces to

$$\frac{\chi''(\omega)}{\omega} = \frac{\beta}{2} G(\omega) \quad (2.20)$$

Comparison with eq. (2.7) shows, that in the high - temperature approximation,  $\phi(t)$  and  $G(t)$  are related by

$$\phi(\omega) = \beta G(\omega) \quad (2.21)$$

where  $\phi(\omega)$  is the Fourier transform of  $\phi(t)$ .

## 2.2 PARAMAGNETIC RESONANCE

Consider a system of  $N$  interacting magnetic ions with spin  $\vec{S}_i$  in a crystal with an external field  $\vec{H}$  directed along the  $z$  axis of a cartesian coordinate frame. The Hamiltonian  $\mathcal{H}$  consists of a Zeeman term

$$\mathcal{H}_Z = g\mu_B H \sum_i S_i^Z \quad (2.22)$$

(the  $g$ -tensor is assumed to be isotropic for simplicity) plus a term  $\mathcal{H}_{int}$  describing the interactions between spins  $\vec{S}_i$ , and  $\vec{S}_j, \dots$  which is denoted by

$$\mathcal{H}_{int} = \sum_{i < j} \mathcal{H}_{ij} \quad (2.23)$$

We denote the eigenstates of  $\mathcal{H}$  with  $|a\rangle, |b\rangle, \dots$  corresponding with energy levels  $E_a, E_b, \dots$ . If the oscillating field is normal to  $\vec{H}$  along e.g the  $x$  axis, it gives rise to a perturbation

$$\mathcal{H}'(t) = g\mu_B H_1 \sum_i S_i^x \cos \omega t \quad (2.24)$$

Using time - dependent perturbation theory, one can show that  $\mathcal{H}'(t)$  causes a constant

transition probability per second  $w_{ab}$  between states  $|a\rangle, |b\rangle$  of the form<sup>3</sup>

$$w_{ab} = \frac{\pi}{2\hbar^2} |\langle a | \mathcal{H}_1 | b \rangle|^2 \delta(\omega_{ab} - \omega) \quad (2.25)$$

where  $\omega_{ab} = \hbar^{-1} |E_a - E_b|$ . (2.26)

When the system is in thermal equilibrium with the lattice, the probability of occupation of a state is given by the Boltzmann factor  $Z^{-1} \exp(-E_a / kT)$ , where  $Z$  denotes the partition function of the system. If  $E_a < E_b$  there is a net absorption rate of energy by the system from the oscillating field, which can be written as<sup>3</sup>

$$\bar{P} = \frac{1}{2} \omega^2 H_1^2 f(\omega) \quad (2.27)$$

where the line - shape function  $f(\omega)$  is defined by

$$f(\omega) = \frac{\pi}{kTZ_{a,b}} \sum_{E_a < E_b} e^{-E_a/kT} (g\mu_B)^2 |\langle a | \delta S^x | b \rangle|^2 \delta(\omega_{ab} - \omega). \quad (2.28)$$

Here it has been assumed, that  $|E_a - E_b| \ll kT$  holds for all levels  $E_a, E_b$ . The condition

$E_a < E_b$  can be omitted in equation (2.28) when  $\omega_{ab}$  is redefined by

$$\omega_{ab} = \hbar^{-1} (E_a - E_b) \quad (2.29)$$

thus formally extending equation (2.28) to negative frequencies. Equating equations (2.11) and (2.27) yields

$$f(\omega) = \frac{\chi''(\omega)}{\omega}. \quad (2.30)$$

By virtue of equations (2.20) and (2.21) one thus obtains

$$f(\omega) = \frac{1}{2} \phi(\omega) = \frac{1}{2} \int_{-\infty}^{\infty} dt e^{-i\omega t} \phi(t) \quad (2.31)$$

where now, due to the choice of the direction of  $H_1$ , only the  $xx$  element of  $\phi(t)$  is considered. Equations (2.28) and (2.31) express the relation between the absorption spectrum and the microscopic properties of the system as given by the eigenstates  $|a\rangle$ ,

$|b\rangle, \dots$ . The fundamental problem is that these eigenstates are not known. This can be circumvented by calculating the moments of  $f(\omega)$  rather than  $f(\omega)$  itself (Van Vleck<sup>4</sup>). Following this method one can also explain the exchange narrowing phenomenon in a semi-quantitative way (Anderson and Weiss<sup>5</sup>). These theories are more or less incorporated in the theory of magnetic resonance developed by Kubo and Tomita<sup>2</sup>, which we shall summarize in the next section.

If  $H_{\text{int}}$  can be assumed as a perturbation of  $H_0$ , the energy spectrum is in first order given by the Zeeman levels

$$E_M = g\mu_B H M \quad (-NS \leq M = \sum m_i \leq NS) \quad (2.32)$$

where  $m_i$  denotes an eigenvalue of  $S_i^z$ . The  $S_i^x$  operator in eq. (2.24) connects states  $|M\rangle, |M'\rangle$  with  $\Delta M = \pm 1$ , corresponding with a transition frequency

$$\omega_{M, M\pm 1} = g\mu_B \hbar^{-1} H = \gamma H \quad (2.33)$$

also known as the Larmor frequency  $\omega_0$ .  $H_{\text{int}}$  may partially lift the degeneracy of  $E_M$  causing a certain distribution of the transition frequencies around  $\omega_0$  (inhomogeneous broadening<sup>6</sup>). The shape function then has a maximum for  $\omega = \omega_0$  (and for  $\omega = -\omega_0$ ) and shows a certain distribution around this maximum. This distribution can be measured by sweeping  $\omega$  around  $\omega_0$ , or by varying the external field  $H = \omega_0 / \gamma$ , such that effectively  $\omega_0$  is swept around a fixed frequency  $\omega_0 = 2\pi\nu$ , which is the usual experimental situation. The shape function,  $f(H - H_0)$  thus obtained is referred to as a resonance line, with a maximum at  $H_0 = \omega_0 / \gamma$  and a full width at half maximum denoted as  $\Delta H$ .

The dependence of  $\chi''$  on  $H$  is typically measured at fixed angular frequency and is shown in figure 5. A single absorption line yields three quantities: The resonance

position  $H_0$ ,  $\Delta H$  and the shape of the curve itself.

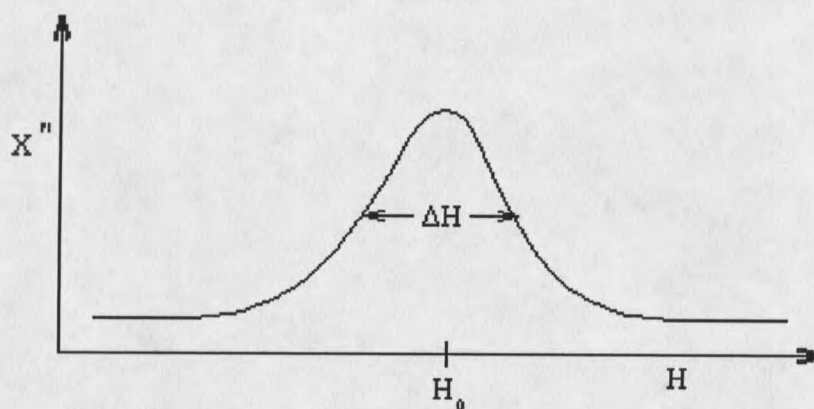


Figure 5. An EPR absorption line.

The linewidth  $\Delta H$  is the quantity in which we are interested in this work. The spectral density corresponding to the spin correlation function can be described by a Dirac delta function centered at the resonant frequency  $\omega_0$ . In reality the absorption line is broadened by non-isotropic interactions like the dipolar interaction between spins. The electrons in the crystal experience different local fields due to this, and thus different resonant conditions. The distribution of the resulting magnetic moments is random and hence the line-width can be described by a Gaussian function:

$$\Delta H \approx H_0 \exp[-C(\omega - \omega_0)^2], \quad \text{where } H_0 \text{ is the field at resonance}^7.$$

Modulation of the exchange interaction causes a narrowing of the absorption line by averaging the local fields to reduce  $\Delta H$  from the dipolar value<sup>8</sup>. For a Heisenberg Hamiltonian the exchange narrowing can be shown to be  $\Delta\omega \approx (\Delta\omega)^2 \hbar / J$  where  $J / \hbar$  is the exchange "frequency" or the rate of spin flips induced by the exchange interaction

Further the lineshape is modulated to yield a Lorentzian, wherein

$$\Delta H \approx \frac{aH_0}{a + b(\omega - \omega_0)^2}$$

The lineshape may be analyzed by plotting  $\frac{\chi''(H_0)}{\chi''(H)}$  vs  $\frac{(H - H_0)^2}{(\Delta H)^2}$ .

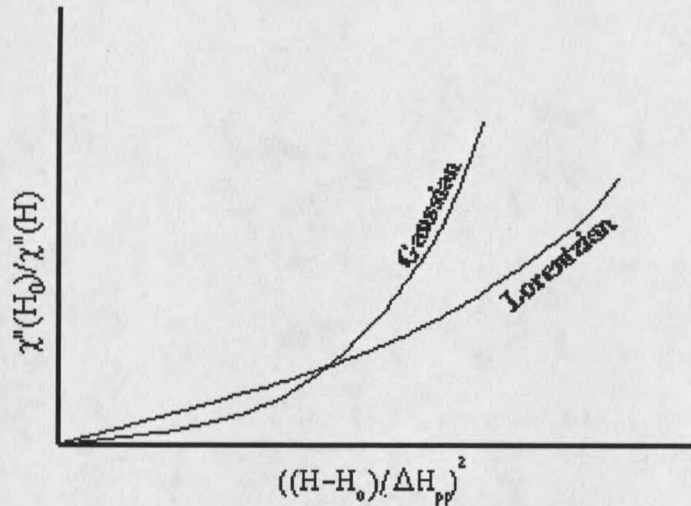


Figure 6. Gaussian and Lorentzian line shapes.

It can be seen that Gaussian curves fall much faster than Lorentzian curves indicating a more random process or a shorter correlation length.

### 2.3 THE KUBO-TOMITA THEORY OF MAGNETIC RESONANCE

All theories concerning the dynamic behavior of spin systems focus on the relation which has to be established between the time-evolution of the magnetization, expressed by  $\phi(t)$ , and the microscopic fluctuations of the system. In this section, we discuss the general outline of the theory first proposed by Kubo and Tomita<sup>2</sup>.

#### Spin Hamiltonian

The main contributions to  $\mathcal{H}_{int}$  (eq. 2.23) are :

$$\mathcal{H}_{\text{ex}} = \mathcal{H}_{\text{exchange}} = -2J \sum_{i < j} \vec{S}_i \cdot \vec{S}_j \quad (2.34)$$

$$\mathcal{H}_{\text{dd}} = \mathcal{H}_{\text{dipole-dipole}} = g^2 \mu_B^2 \sum_{i < j} r_{ij}^{-3} [ \vec{S}_i \cdot \vec{S}_j - 3(\vec{S}_i \cdot \vec{u}_{ij})(\vec{S}_j \cdot \vec{u}_{ij}) ]. \quad (2.35)$$

$J$  denotes the symmetric (Heisenberg) exchange constant ;  $\vec{r}_{ij} \equiv \vec{r}_j - \vec{r}_i$  is the position vector of  $\vec{S}_j$  relative to  $\vec{S}_i$  and  $\vec{u}_{ij} \equiv \vec{r}_{ij}/r_{ij}$ .

To describe the effect of  $\mathcal{H}$  on the motion of  $\vec{M}$  and the corresponding resonance spectrum, the Hamiltonian is separated into two parts,  $\mathcal{H}_0$  and  $\mathcal{H}_1$ , such that

$\mathcal{H}_0 = \mathcal{H}_z + \mathcal{H}_{\text{ex}}$  and  $\mathcal{H}_1 = \mathcal{H}_{\text{dd}}$ . The terms of  $\mathcal{H}_0$  obey the commutation rules:

$$[\mathcal{H}_z, \mathcal{H}_{\text{ex}}] = 0. \quad (2.36)$$

$$[\mathcal{H}_{\text{ex}}, M^\mu] = 0 \quad (\mu = x, y, z) \quad (2.37)$$

Using these commutation rules, it can be shown that the motion of  $\vec{M}$  consists of two kinds of modes :  $\mathcal{H}_z$  gives rise to a precessional motion of  $\vec{M}$  around  $\vec{H}$ , whereas  $\mathcal{H}_{\text{ex}}$  has no direct effect on this motion. However  $\mathcal{H}_{\text{ex}}$  modulates the dipolar interaction  $H_{\text{dd}}$ , which itself causes a random motion of  $\vec{M}$ . In the absence of  $H_{\text{dd}}$ , the resonance spectrum would in general consist of sharp resonances.  $H_{\text{dd}}$  causes a broadening and shift of these lines and may lead to the appearance of satellite lines.

## 2.4 CORRELATION FUNCTION OF THE EXCHANGE MODULATION<sup>9</sup>

Kubo and Tomita have obtained an expression of  $\phi(t)$  in terms of a new correlation function  $\psi(t)$ , which describes the random motion of  $M^x$ . An interaction representation is used whereby

$$M_x(t) = \exp [i\mathcal{H}_0 t / \hbar] \tilde{M}_x \exp [-i\mathcal{H}_0 t / \hbar] \quad (2.38)$$

$M_x(t)$  describes the motion of  $\tilde{M}_x$  in a coordinate frame moving with a Zeeman precession, caused by  $\mathcal{H}_z$ . In this frame, the motion of  $\tilde{M}_x$  is generated by

$$\frac{d\tilde{M}_x}{dt} = \frac{i}{\hbar} [\tilde{\mathcal{H}}'(t), \tilde{M}_x] \quad (2.39)$$

where

$$\tilde{\mathcal{H}}'(t) = \exp [ -i\mathcal{H}_0 t / \hbar] \mathcal{H}'(0) \exp [i\mathcal{H}_0 t / \hbar]. \quad (2.40)$$

If we neglect  $\mathcal{H}'$  in computing the thermal averages  $\chi''$  will then be given by

$$\chi''(\omega) = \frac{\omega V}{8k_B T} \left[ \int_0^\infty \langle \tilde{M}_+(t) M_-(0) \rangle \exp [i(\omega_0 - \omega)t] dt + \int_0^\infty \langle \tilde{M}_-(t) M_+(0) \rangle \exp [-i(\omega_0 - \omega)t] dt \right] \quad (2.41)$$

where  $M_\pm$  are the usual raising and lowering operators. It can be seen that  $\chi''(\omega)$  is peaked at  $\omega_0$  and has a width related to the correlation function  $\langle \tilde{M}_+(t) M_-(0) \rangle$  which

decays on the relatively slow time scale of  $\mathcal{H}'$ . It is convenient to write the relaxation function in terms of the ladder operators as

$$\phi(t) = \frac{\langle \tilde{M}_+(t) M_-(0) \rangle}{\langle M_+ M_- \rangle} \quad (2.42)$$

The shape of  $\chi''(\omega)$  is given by the Fourier transform of  $\phi(t)$  at the frequency  $(\omega_0 - \omega)$ .

Kubo and Tomita expanded the above expression and disregarding terms higher than the second order ones, obtained the following expression for the relaxation function,

$$\phi(t) = \exp \left[ - \int_0^t d\tau (t - \tau) \psi(\tau) \right], \quad (2.43)$$

Here the time - correlation of the exchange modulation obeys,

$$\psi(\tau) = \frac{1}{\hbar^2} \frac{\langle [\tilde{\mathcal{H}}'(\tau), M_+(0)] [M_-(0), \mathcal{H}'(0)] \rangle}{\langle M_+ M_- \rangle} \quad (2.44)$$

in the high temperature approximation.

The shape function of the resonance line at  $\omega_0$  obeys<sup>10</sup>

$$f^+(\omega) \propto \int_{-\infty}^{\infty} dt e^{-i(\omega-\omega_0)t} \hat{\phi}(t) \quad (2.45)$$

If  $f^+(\omega)$  is symmetric about  $\omega_0$  and narrow one can define a lineshape function

$$f^+(\omega - \omega_0) = f^+(\omega)$$

Inversion of the above yields

$$\hat{\phi}(t) \propto \int_{-\infty}^{\infty} d\omega e^{i(\omega-\omega_0)t} \hat{f}^+(\omega - \omega_0) \quad (2.46)$$

The influence of  $H_{ex}$  on the decay of  $\psi(t)$  and hence on  $f^+(\omega - \omega_0)$  may be obtained by choosing an analytical expression for  $\psi(t)$ .  $\psi(t)$  decays in a characteristic time  $\tau_c = \hbar/J$ , since the exchange interaction dominates  $H_0$ . Thus for  $t \ll \tau_c$ , a Gaussian correlation function serves as an approximation of  $\psi(t)$ , i.e

$$(a) \quad \psi(t) = \omega_p^2 \exp\left[-\frac{1}{2}\omega_e^2 t^2\right] \quad (2.47)$$

where  $\omega_p$  denotes the perturbation frequency which is characteristic of  $H_{dd}$  only and  $\omega_e$  can be regarded as a measure of the strength of  $H_{ex}$ .

In this limit  $\omega_e \ll \omega_p$  and one may assume  $\psi(t) \approx \psi(0)$  yielding

$$\begin{aligned} \phi(t) &= \phi(0) \exp\left[-\omega_p^2 \int_0^t (t-\tau) d\tau\right] \\ &= \phi(0) \exp\left[-\frac{1}{2}\omega_p^2 t^2\right] \end{aligned} \quad (2.48)$$

This results in a line shape function

$$f^+(\omega - \omega_0) \propto \exp\left[-\frac{(\omega - \omega_0)^2}{2\omega_p^2}\right] \quad (2.49)$$

which is a Gaussian with a half - width

$$\Delta\omega_{1/2} = [(2\ln 2) \omega_p^2]^{1/2} \quad (2.50)$$

b) For  $t \gg \tau_c$  i.e when  $\omega_e > \omega_p$   $\psi(t)$  effectively decays to zero before  $\phi(t)$  changes appreciably. Hence

$$\phi(t) = \phi(0) \exp[-(\pi/2)^{1/2} (\omega_p^2/\omega_e)|t|] \quad (2.51)$$

For the shape function one obtains,

$$f^+(\omega - \omega_0) \propto \frac{1}{(\omega - \omega_0^2) + (\pi/2)(\omega_p^2/\omega_e)^2} \quad (2.52)$$

This is a Lorentzian line with half - width

$$\Delta\omega_{1/2} = (\pi/2)^{1/2} (\omega_p^2/\omega_e). \quad (2.53)$$

In terms of magnetic field the linewidth can be expressed as

$$\Delta H \sim \hbar(\omega_p^2)/\gamma J.$$

It can be observed that the exchange modulation does two things :

- 1) alters the line-shape from Gaussian to Lorentzian
- 2) the frequency width has decreased from  $\omega_p$  to a factor  $\omega_p \tau_c \ll 1$ . This effect is known as *exchange narrowing*.

## 2.5 SPIN DIFFUSION<sup>11</sup>

The previous results given for the derivation of the Lorentzian lineshape break down in 1d and 2d because of the dominant effect of spin diffusion. A study of the time evolution of the spin-spin correlation function helps us understand the dynamic behavior of the local fluctuations. It can be defined as

$$C_{ij}^\alpha(t) = \langle S_i^\alpha(t) S_j^\alpha \rangle.$$

The auto-correlation function ( $i = j$ ) decreases smoothly with characteristic rate  $\omega_e = J[8zS(S+1)/3]^{1/2}$ , where  $z$  is the number of nearest neighbors. It can be

seen from the figure 7 that at  $\omega_e t \gg 1$  the correlation functions decrease much more slowly in the low-d case when compared to the 3d case.

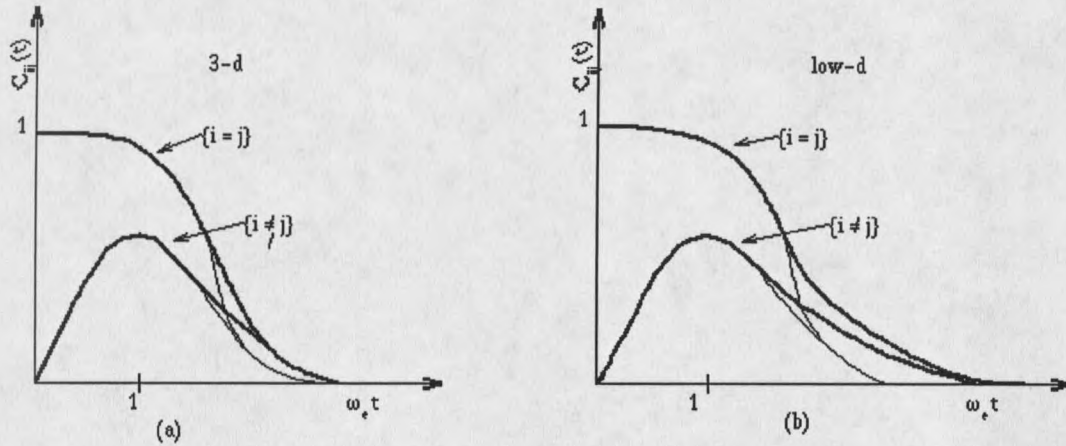


Figure 7. 2-spin correlation functions in (a) 3-d and (b) low-d magnetic systems. The time scale is defined by the exchange frequency  $\omega_e$ .

When  $\omega_e t \ll 1$ , the dimensionality plays a minor role only. For  $\omega_e t \gg 1$  a hydrodynamic description is used which can be justified by the fact that the Hamiltonian of equation (2.34) is a constant of motion. Therefore in the high-temperature limit, the microscopic fluctuations are governed by the diffusion equation:

$$D\nabla^2 C^\alpha(\mathbf{r}, t) = \frac{\partial}{\partial t} C^\alpha(\mathbf{r}, t) \quad (2.54)$$

where  $D$  is the diffusion coefficient. The solution to this equation strongly depends on the dimensionality  $d$  of the lattice.

$$C^\alpha(\mathbf{r}, t) = (4\pi Dt)^{-d/2} \exp(-r^2 / 4Dt) \quad (2.55)$$

The diffusive behaviour completes the description of the function at  $\omega_e t \gg 1$ . In 3d the tail decreases rapidly with time as  $t^{-3/2}$ . On the other hand in 1d and 2d systems the tail

persists at much longer times . In terms of spectral densities the diffusive behaviour leads to the divergence of the functions  $C^\alpha(\omega)$  at  $\omega = 0$ . One can show that,

$$C^\alpha(\omega) \sim \frac{1}{2\pi} (2D\omega)^{-1/2} \quad \text{for } d = 1 \quad (2.56)$$

$$C^\alpha(\omega) \sim \frac{1}{4\pi D} \ln(4\pi D / \omega) \quad \text{for } d = 2. \quad (2.57)$$

In real systems these divergences are usually suppressed for the following reasons:

(i) In crystals the spin arrangements do not correspond to a strictly 2d lattice. There exist small magnetic couplings between planes, giving a 3d character to the magnetic interaction.

(ii) The interaction Hamiltonian is not strictly isotropic. Anisotropic terms such as the interplane dipolar interactions  $\mathcal{D}$  are always present as perturbations in the Hamiltonian. In order to understand the truncation effects it is convenient if we can consider the spin operators in reciprocal space,

$$S_{\mathbf{q}}^\alpha = N^{-1/2} \sum_{\mathbf{j}=1}^N S_{\mathbf{j}}^\alpha e^{i\mathbf{q}\cdot\mathbf{r}_{\mathbf{j}}} \quad \text{and}$$

$$C_{\mathbf{n}}^\alpha(t) = \sum_{\mathbf{q}} C_{\mathbf{q}}^\alpha(t) e^{-i\mathbf{q}\cdot\mathbf{r}_{\mathbf{n}}} \quad \text{where } C_{\mathbf{q}}^\alpha(t) \text{ represents the normal mode}$$

associated with the wave vector  $\mathbf{q}$  :

$$C_{\mathbf{q}}^\alpha(t) = \left\langle S_{\mathbf{q}}^\alpha(t) (S_{\mathbf{q}}^\alpha)^+ \right\rangle \quad (2.58)$$

The corresponding spectral density is obtained by taking the Fourier transform.

From the diffusion equation one obtains

$$C_q^\alpha(\omega) = \left\langle |S_q^\alpha|^2 \right\rangle \frac{Dq^2}{\omega^2 + (Dq^2)^2} \quad (2.59)$$

For a pure Heisenberg system the width of the normal mode  $C_q^\alpha(\omega)$  is zero at  $q = 0$ , according to  $\Gamma_q = Dq^2$ . This explains the divergence of the spectral densities  $C_q^\alpha(\omega)$  in 1D and 2D systems.

## 2.6 EPR LINESHAPE STUDIES<sup>9</sup>

In this section we consider the problem of the shape of the EPR line. In studying the EPR lineshape we come across four-spin correlation functions of the form

$\langle \hat{S}_i^\alpha(\tau) \hat{S}_j^\beta(\tau) S_k^{\alpha'} S_l^{\beta'} \rangle$ . In NMR formulation where nuclear spins are randomly oriented, four-spin correlation functions can be reduced to two-spin correlation functions by suitable approximations. In the case of EPR since the resonating spins are coupled, such a reduction is not possible. As a consequence the EPR in a crystal can be, in general, described as a collective response of the  $q = 0$  mode of the total magnetization rather than one in which each spin resonates independently in its own local environment.

The common method of dealing with the four-spin correlation functions is to factorize them according to

$$\langle \hat{S}_i^\alpha(\tau) \hat{S}_j^\beta(\tau) S_k^{\alpha'} S_l^{\beta'} \rangle = \langle \hat{S}_i^\alpha(\tau) S_k^{\alpha'} \rangle \langle \hat{S}_j^\beta(\tau) S_l^{\beta'} \rangle + \langle \hat{S}_i^\alpha(\tau) S_l^{\beta'} \rangle \langle \hat{S}_j^\beta(\tau) S_k^{\alpha'} \rangle \quad (2.60)$$

The factorization of the kind  $\langle \hat{S}_i^\alpha(\tau) \hat{S}_j^\beta(\tau) \rangle \langle S_k^{\alpha'} S_l^{\beta'} \rangle$  has been ignored since it leads to a time independent term which is zero, for example, like the dipolar term. In order to

us understand these concepts we define the dipolar interaction coefficients

$$\langle \hat{g}_0(\tau) g_0^+ \rangle = \sum_{ijkl} F_{ji}^{(0)} F_{kl}^{(0)} \langle \hat{S}_i^z(\tau) S_k^z \rangle \langle \hat{S}_j^+(\tau) S_l^- \rangle \quad \text{where}$$

$$F_{ji}^{(0)} = -2\gamma\hbar(2K_{ij}^{+-} - K_{ij}^{zz}).$$

Here  $K_{ij}$  represents interactions which include terms like dipolar couplings, spin-orbit and crystal field couplings and only secular terms have been considered. When the magnetic field is parallel to the chain axis or perpendicular to the magnetization plane ( $\theta = 0$ ), only secular terms with dipolar coefficients of  $F_n^m$  ( $m = 0$ ) contribute to the linewidth. For  $|\omega - \omega_0| \leq \Delta H$ , diffusive behavior (non-Lorentzian) is minimized, and the fluctuations are actually dominated by the Heisenberg Hamiltonian. For  $|\omega - \omega_0| \geq \Delta H$ , the contribution from the secular terms is negligible and the spin dynamics is governed by diffusive processes.

For another special direction of H i.e., at the magic angle when  $\theta = 55^\circ$  the secular term  $F^{(0)}$  vanishes, and only non-secular terms with  $m = \pm 1, -2$  contribute to the EPR spectrum where the line-shape is Lorentzian. In the general case for any direction of the magnetic field the secular and the non-secular terms together contribute to the EPR linewidth.

An alternate procedure for treating four-spin correlation functions is to use the Random Phase Approximation (RPA). This scheme involves taking the Fourier transform of the exact expression  $\langle \hat{g}_0(\tau) g_0^+ \rangle$  before decoupling, wherein

$$\langle \hat{g}_0(\tau) g_0^+ \rangle = \sum_{qq'} F_{-q}^{(0)} F_{-q'}^{(0)} \langle \hat{S}_q^z(\tau) \hat{S}_{-q}^+(\tau) S_{q'}^z S_{q'}^- \rangle$$

From the above we retain only  $q = q'$  terms in making the RPA so that,

$$\langle \hat{g}_0(\tau) g_0^+ \rangle = \sum_q |F_q^{(0)}|^2 \langle \hat{S}_q^z(\tau) \hat{S}_{-q}^+(\tau) S_q^z S_{-q}^- \rangle \quad (2.61)$$

In the limit  $N \rightarrow \infty$  it can be shown that equation (2.61) and the decoupled form (2.60) are equivalent.

Another scheme of simplifying the EPR correlation functions is to assume their diffusive behavior. A hydrodynamic description is used at long times yielding the diffusion law that the spin-correlation function decays as  $\tau^{-d/2}$  but the diffusion constant  $D$  is twice as large as that for the case of two-spin correlation functions. In each of the above methods the essential feature that is noticed is that the sum over all pairs  $(i,j)$  and  $(k,l)$  produces a behavior that is dominated by the  $q \rightarrow 0$  mode.

## 2.7 TEMPERATURE DEPENDENCE OF THE LINEWIDTH OF A 2D AFM

In this we briefly outline the temperature dependence of the EPR linewidth in a 2d system. These results are used as a starting point for the derivation and analysis of linewidths which will be discussed in the following chapters. In this discussion we distinguish between two regions; firstly the high temperature region, in which the range of the spatial correlations between spins  $\vec{S}_i$  and  $\vec{S}_j$  steadily increases when  $T$  is lowered, but where the assumption of isotropy still holds. In this region the dominant effects are governed by short range order (SRO) and the basic picture of spin diffusion dominated by

by  $q \rightarrow 0$  is still applicable. Secondly there is the critical region, in which effects marking the onset of 3d long range order become predominant. In the antiferromagnetic layers  $\chi_T$  (isothermal susceptibility) is finite at  $T_N$  and the important contributions to the  $\vec{q}$  sum come from the superlattice vector  $\vec{q} = \vec{q}_0$ . EPR no longer probes fluctuations of the order parameter and therefore, it becomes important to single out this property. This is in contrast to the case of a ferromagnet whose  $\chi_T$  diverges near the critical temperature and where the long-wave  $\vec{q} \approx 0$  fluctuations dominate the EPR linewidth. The temperature which separates these two regions generally depends upon the systems under investigation. In 2d AFM systems it may be of the order of  $2T_N$ <sup>12</sup>.

When analyzing the temperature dependence of the linewidths at temperatures sufficiently above  $T_N$ , where the staggered susceptibility satisfies  $\chi_{||}^S = \chi_{\perp}^S$ , then the linewidth may be written as

$$\Delta H(T) = \Delta H_{\text{crit}}(T) + \Delta H_{T=\infty}. \quad (2.62)$$

Castner and Seehra were able to fit  $\Delta H_{\text{crit}}(T)$  to a power - law expression  $C\varepsilon^p$  using Huber's procedure for 2d AFMs  $K_2\text{MnF}_4$  and  $\text{Rb}_2\text{MnF}_4$ <sup>13,14</sup>. Here  $\varepsilon$  is the reduced temperature  $\frac{|T-T_N|}{T_N}$  and  $p \approx 2.4$ .  $\Delta H_{T=\infty}$  and  $C$  may be regarded as temperature

independent. Then  $\Delta H_{\text{crit}}(T)$  is given by

$$\Delta H_{\text{crit}}(T) \approx f(\theta) \frac{T}{\chi_{\perp}} \sum_q \int_0^{\infty} dt \langle S(\mathbf{q}+\mathbf{q}_0, t), S(\mathbf{q}+\mathbf{q}_0) \rangle^2 \quad (2.63)$$

where  $f(\theta)$  is a function which depends on the symmetry of the crystal and  $\theta$  is the angle between the applied field and the  $c$ -axis.

## REFERENCES CITED IN CHAPTER 2

1. R. Kubo, *J. Phys. Soc. Japan*, **12**, 570 (1957).
2. R. Kubo and K. Tomita, *J. Phys. Soc. Japan*, **9**, 888 (1954).
3. C. P. Schlichter, *Principles of Magnetic Resonance*, Harper and Row, New York (1963).
4. J. H. Van Vleck, *Phys. Rev* **74**, 1168 (1954).
5. P. W. Andersen and P. R. Weiss, *Rev. Mod. Phys.*, **25**, 269 (1953).
6. A. Abragam and B. Bleaney, *Electron Paramagnetic Resonance of transition ions*, Clarendon Press, Oxford ( 1970).
7. R.S. Rubins, unpublished seminar notes, Montana State University, 1994.
8. J.E. Drumheller, *Magn. Res. Rev* **7**. 123 (1982).
9. P.M. Richards, in "*Proc. International School of Physics Enrico Fermi, Course LIX: Local Properties at Phase transitions*", pp 539, eds K.A. Muller and A. Rigamonti, North Holland, 1976.
10. J. Onderwaater, Ph.D. Thesis, University of Leiden, The Netherlands, 1980.
11. "Magnetic Properties of Layered Transition Metal Compounds", ed. L.J.de Jongh, Kluwer, Dordrecht, The Netherlands, 1990.
12. P.M. Richards and M.B. Salamon, *Phys.Rev. B9*, **32**(1974).
13. D.L. Huber, *Phys. Rev.* **B6**, 3180 (1972); D.L. Huber and M.S. Seehra, *Phys. Lett.*, **43A**, 311 (1973).
14. H.W. de Wijn, L.R. Walker, J.L Davis and H.J. Guggenheim, *Solid State Commun.*, **11**, 803 (1972); M.S. Seehra and T.G. Castner, *Solid State Commun.* **8**, 787 (1970).

## CHAPTER 3

## 3. SOLITON CONTRIBUTION TO THE EPR LINEWIDTH

## 3.1 INTRODUCTION

As mentioned before there is no LRO in 2d Heisenberg magnets, but only SRO characterized by a correlation length  $R$ . We are interested in the spin dynamics in the SRO regimes of such systems. The main question of interest is, whether the spin dynamics are governed by extended collective excitations like spin waves, or are there other types of excitations. In particular as we approach the critical temperature the susceptibility is large and therefore large amplitude fluctuations become important. For example in antiferromagnets, where even the ground state is not precisely known, the spin-wave expansion fails to treat fluctuations in the critical regime. Consequently, it becomes essential to deal with nonlinear effects and to study under what conditions they become significant to the spin dynamics.

Starting with the discovery of solitons in 1844, the field of classical nonlinear dynamics, and in particular the treatment of problems in 1d magnetic systems in recent years, has made tremendous progress. The possibility of soliton-like excitations playing a nontrivial role in the critical dynamics has led to an explosion of theoretical and experimental activities in the last two decades. The existence of solitons in 1d systems was predicted by Mikeska<sup>1</sup> and was identified experimentally in  $\text{CsNiF}_3$ <sup>2</sup>. Considerable progress has been made in the diagonalization problem for  $s = 1/2$  spin chain since the pioneering work by Bethe<sup>3</sup> in 1931, where the elementary excitations were magnons and bound magnons. It was not until recently that Johnson *et al.*<sup>4</sup> were able to derive

thermodynamic quantities like susceptibility, from the excitation spectrum.

Until recently it was well accepted that the thermodynamics of quantum spin chains was dominated by spin waves. Recent theoretical work<sup>5</sup> and experiments<sup>6</sup> have shown that a  $s = 1/2$  chain structure supports nonlinear excitations such as bound magnons and solitons in the temperature region above  $T_C$ , as predicted by Johnson and Bonner<sup>4</sup>.

The classical Sine-Gordon(SG) chain serves as a good model system, in the continuum approximation, to investigate the nonlinear effects on the spin dynamics of 1d magnets. The most detailed information about the excitations can be obtained from a measurement of the spin-spin correlation function  $S(\vec{q}, \omega)$  in reciprocal space. Inelastic neutron scattering(INS) and EPR are two techniques which allow the direct measurement of  $S(\vec{q}, \omega)$ . While a large range of  $\vec{q}$  and  $\omega$  are accessible via the neutron scattering measurement, EPR measures at  $\vec{q} \approx 0$  with a very small range. This led to several INS studies on chain structures, to detect a SG soliton<sup>7, 8</sup>. A broadening of the central peak structure was observed, which is the signature of the AFM solitons. The x-y soliton shows up at  $\vec{q} \approx 0$  as well, as calculated by Sasaki<sup>9</sup>.

Due to the mathematical complexity involved, solvable models in 2d systems have been scarce. The spin-wave theory has been successful in accounting for the low-temperature properties of a number of 2d magnetic systems which have anisotropy small compared to exchange. Recently this study has been extended to include xy and Ising type anisotropy in the 2d ferromagnet<sup>10</sup>. Analytical results for nonlinear excitations in

the continuum approximation are available for the planar X-Y model and the isotropic Heisenberg models only. As mentioned earlier, in the X-Y model wherein the spins are confined to a plane, an interesting topological transition is known to exist. According to Kosterlitz and Thouless<sup>11</sup>, this transition corresponds to an unbinding of vortex-antivortex pairs into a gas of free vortices. Computer simulations give clear evidence of the topological excitations destroying LRO<sup>12</sup>. At low enough temperatures the Gaussian velocity distribution of the less dense gas leads to a central peak structure ( $q = 0$ ) in the dynamic structure factor.

It has been rigorously proven that the 2d Heisenberg model does not exhibit a phase transition at any finite temperature<sup>13</sup>. If an easy-axis anisotropy is added to the Heisenberg model, the spin-wave spectrum acquires a gap and the system becomes metastable<sup>14</sup>. Assuming diffusive behavior Richards and Salamon<sup>15</sup> calculated the time-dependent correlation functions for n-dimensional systems. This resulted in a calculation of the EPR linewidths, with the linewidth and the lineshape depending on the orientation of the crystal chain axis or the easy plane relative to the external magnetic field. Neutron scattering experiments in a 2d quantum Heisenberg model were interpreted by spin-wave excitations<sup>16</sup>. Monte Carlo treatments<sup>17</sup>, Schwinger Boson mean field theory<sup>18</sup>, scaling theory combined with renormalization group analysis and hydrodynamics<sup>19, 20</sup>, are some of the tools used in calculating the coherence length and the pair-correlation function in 2d quantum and classical systems.

Recent numerical simulations of a 2d  $s = 1/2$  AFM, have shown that the spin correlation functions have the same behavior as in the 2d classical spin systems thereby

establishing the correspondence between the 2d classical magnet and the high  $T_C$  superconductors<sup>17</sup>. For a quantum Heisenberg AFM the EPR linewidth has been calculated in the spin-wave approximation, and compared with experiment<sup>21,22</sup>. Localized, continuous, and analytic expressions for excitations of the 2d isotropic Heisenberg model, in the classical limit were found by Belavin and Polyakov<sup>23</sup> which was referred to in Chapter 1. The effect of these excitations on the spin-correlation functions was investigated by Trimper<sup>24</sup>. He found the correlation function changes over from a power law decay to that of an exponential and that the correlation length does not diverge at any finite temperature.

### 3.2 SOLITONS IN 2D HEISENBERG MAGNETS

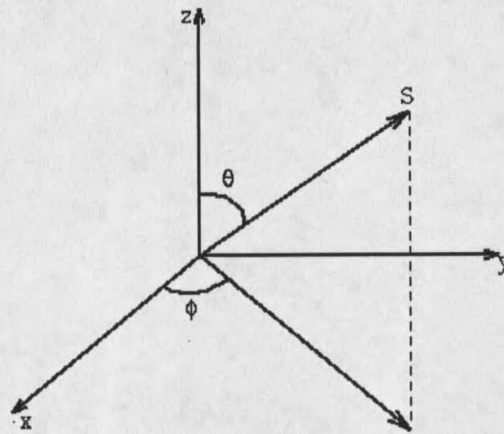


Figure 8. Orientation of the spin  $\vec{S}$  as a function of  $\theta$  and  $\phi$ , the polar angles.

We shall first consider the case of a Heisenberg ferromagnet. The isotropic Heisenberg Hamiltonian for a ferromagnet can be written as,

$$H = -J \sum_{\langle ij \rangle} \vec{S}_i \cdot \vec{S}_j \quad (3.1)$$

Expressing the classical spin vectors in the spherical polar co-ordinate system and assuming a continuum approximation in which the neighboring spins are nearly parallel, the above Hamiltonian can be rewritten as,

$$H = -JS^2N + \frac{JS^2}{2} \iint [(\nabla\theta)^2 + (\nabla\phi)^2 \sin^2\theta] d^2r \quad (3.2)$$

Here the spin vector can be represented as  $\vec{S}_i = S(\sin\theta_i \cos\phi_i, \sin\theta_i \sin\phi_i, \cos\theta_i)$ . The first term is the ground state energy of  $N$  bonds. The second term represents the excitation energy resulting from the deviation in the magnetization. This can be obtained by minimizing the expression within the parenthesis in the integral with respect to  $\theta(x, y)$  and  $\phi(x, y)$ . The integration of the resulting Euler-Lagrange equations yields the solutions  $\phi = \phi$  and  $\tan(\theta(r)/2) = (r_0/r)^{\pm 1}$ . The integration constant  $r_0$  reflects the scale invariance if the Hamiltonian in equation (3.2) and the sign of the exponent gives the magnetization direction as  $r \rightarrow \infty$ . Figure 9 depicts the  $r$ -dependence of the polar angle.

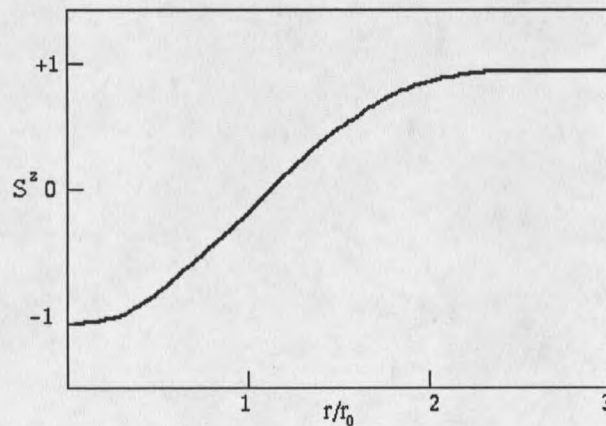


Figure 9. The radial dependence of the polar angle of the spins in a 2d soliton.

In 1d systems topological solitons can be viewed as domain walls moving freely along the chains having substantial magnetic order. For 2d systems, solitons can be defined as excitations which minimize the continuum free energy. Fig 10 represents a simplified picture of the spin structure. The projection of the spin vectors on the  $xy$ -plane resembles a vortex structure.

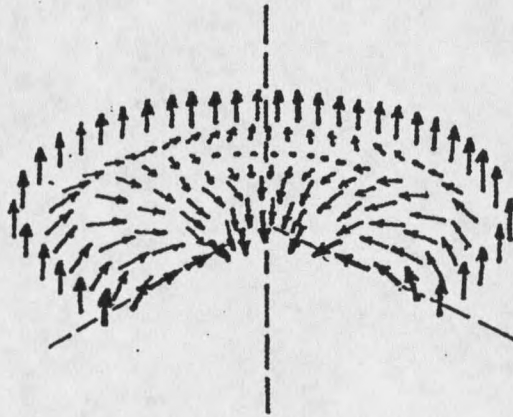


Figure 10. The structure of a two-dimensional topological soliton in a ferromagnet.

The static and dynamic properties of a 2d classical Heisenberg model with easy-plane anisotropy have been investigated<sup>25</sup>. Two static vortex spin configurations, planar and out-of-plane were found via a continuum theory. Numerical studies<sup>25</sup>, which include the discrete nature of the lattice, have shown there exists a critical value of the anisotropy parameter, which decides the region in which out-of-plane(in-plane) vortices are stable. For  $\lambda < \lambda_c < \sim 0.72$  on a square lattice, the static vortices are purely in-plane, whereas for  $\lambda > \lambda_c$  the out-of-plane component increases with  $\lambda$ . It has been observed that the correlation of the out-of-plane components is very sensitive to the vortex shape

are stable, the spin correlation function reveals a Gaussian central peak, whose width increases linearly with wave-vector  $q$ . This indicates that multimagnon processes and vortex-magnon interactions have an appreciable influence on the central peak. For a 2d ferromagnet vortex-magnon interaction has been considered in the xy ferromagnet<sup>26</sup>. Later this was generalized to include Ising and xy type anisotropy by examining the small oscillations about the static vortex structure<sup>10</sup>. A similar study done by Zaspel<sup>27</sup> on soliton dynamics contains several important results. First the random motion of the spins breaks the circular symmetry of the isotropic Heisenberg model. The dynamic correlation function is found to be a modified Gaussian with a central peak structure. With anisotropy it has been found that static solutions are impossible<sup>28</sup> unless a fourth order Skyrme term is included in the Hamiltonian. Waldner's numerical work<sup>29</sup> on the shape of the solitons indicates that it does not change appreciably in the presence of weak easy-axis anisotropy which is usually present in real systems.

### 3.2.1 SOLITONS IN 2D ANTIFERROMAGNETS

In this section we will derive a solution for the 2d classical AFM considering a nonlinear Euler-Lagrangian equation<sup>30</sup>. This result will be used later in the EPR linewidth calculation.

In order to write the Lagrangian for the system it is necessary to define the normalized magnetization vector  $\vec{m} = \frac{1}{2S}(\vec{S}_1 + \vec{S}_2)$  and the sublattice magnetization

vector  $\vec{l} = \frac{1}{2S}(\vec{S}_1 - \vec{S}_2)$  where  $\vec{S}_1$  and  $\vec{S}_2$  refer to the classical spin vectors of the two different sublattices. It is reasonable to assume that  $|\vec{l}| \gg |\vec{m}|$  where the nearest neighbor spins are almost antiparallel. With this assumption we can express the Lagrangian for the system as

$$L = \frac{JS^2}{2} \iint \left[ \frac{\theta_t^2}{c^2} - (\nabla\theta)^2 + \sin^2\theta \left( \frac{\phi_t^2}{c^2} - \nabla\phi^2 \right) \right] d^2r \quad (3.3)$$

Here  $\theta$  and  $\phi$  represent the polar and the azimuthal angles of the sublattice magnetization vector  $\vec{l}$  and  $\theta_t$  and  $\phi_t$  are the partial derivatives with respect to time. Static solutions to  $\theta_t$  and  $\phi_t$  can be obtained by following the same procedure as that for a ferromagnet in the continuum approximation. Using a similar Lagrangian formulation Ivanov and Sheka<sup>31</sup> have investigated mobile out-of-plane vortices in a classical 2d easy plane AFM in the presence of an external magnetic field. The presence of the field substantially modified the shape and position of the central peak of the dynamic structure factor resulting from vortex dynamics.

### 3.2.2 MOTIVATION FOR THE CURRENT WORK

It has been established that solitons in 1d chains will result in an Arrhenius temperature dependence of the linewidth, i.e.  $\Delta H \sim \exp(E_s/T)$  where  $E_s$  is the soliton energy<sup>32</sup>. Waldner's investigation<sup>29,33,34</sup> on the possible effects of solitons on the linewidth in layered Mn compounds has provided the motivation for the current work.

Waldner proposed that the observed temperature dependence of the linewidth

was due to the 2d spin correlations being modified in the presence of solitons. He based his conclusions upon a possible extension of Mikeska's<sup>1</sup> theory of slowly moving solitons with excitation energy  $E$ , for 1d magnets. By reexamining previously available EPR data on quasi-2d spin 5/2 AFMs, he found excellent fits to the above model<sup>34</sup>, and the excitation energy was found to be approximately  $4\pi JS^2$  to within 10%. In spite of the good agreement between theory and experiment Waldner argued that the Arrhenius temperature dependence does not prove the presence of solitons. He noted that the thermal activation is doubtful for such high ratios of  $(E_s/kT)$  and there was insufficient information about the nature of solitons. The arguments against associating solitons with the above behavior are twofold. EPR linewidth involves a dynamic correlation function, whereas the Belavin and Polyakov soliton is static. Secondly the observed Arrhenius behavior is derived from the motion of 1d Sine-Gordon solitons which does not apply to 2d systems.

The important question ahead of us is, are solitons responsible for the Arrhenius broadening observed in layered Mn compounds? In order to answer this question we need to address several issues. It has been noted that the spatial effects of the gapless spin waves and the solitons on the correlation length are too similar, making a discrimination between the two difficult<sup>16</sup>. However, doping the magnetic compound with nonmagnetic impurities introduces a concentration dependence on the EPR linewidth which may be used to separate the soliton contribution from the spin-wave contribution<sup>35</sup>. We need to consider the temporal effects of the two excitations separately, both of which result in a broadening of the EPR lines. This means that we

need to address the problem of soliton dynamics. The most obvious soliton motion has to be ruled out for the following reason. Moving solitons results in a central peak at  $\omega = 0$ , which is far removed from the EPR frequency. We will therefore have to consider soliton-magnon interaction as the possible time-dependent mechanism.

### 3.2.3 EFFECTS OF DOPING AN AFM WITH IMPURITIES

In recent years a great deal of theoretical as well as experimental work has been done on random-site diluted magnets<sup>36</sup>. In the case of magnetically diluted systems the ordering temperature  $T_N$  decreases with increasing concentration  $p$  of the impurities. For 1d chains even a small impurity concentration ( $\sim 1\%$ ) causes a broadening of the EPR line at room temperature<sup>37</sup> while for 2d, the effects are more pronounced near the percolation limit  $p = 0.59$  for the square lattice<sup>38</sup>. When a magnetic insulator is diluted with nonmagnetic impurities, the exchange pathways are cut off at random and the spin correlation function will decay more rapidly with distance. This results in the exchange narrowing in the EPR linewidth becoming less efficient and a broadening occurs. For 2d systems this effect is more dramatic near the percolation limit when the coherent spin network breaks into finite clusters. A 40% reduction in the EPR exponent associated with the divergence of the linewidth in the fluctuation region, was obtained upon doping  $K_2MnF_4$  with a small amount of Fe impurities<sup>39</sup>. This effect was attributed to the spin-phonon coupling of the non-S state  $Fe^{2+}$  ions, which should impede the slowing down of the critical fluctuations close to  $T_N$ . A theory developed by Van Luijk *et al.*<sup>40</sup>, to treat the

local thermodynamic properties around isolated impurities in an AFM, is based upon a Green's function formalism. In a recent review article on 2d spin-wave theory, data on  $K_2MnF_4$  (diluted with Zn, Mg, Ni)<sup>40</sup> has been compared with the above mentioned theory. De Wijn *et al.*<sup>41</sup>, have concluded that the effect of the impurity-associated excitations is very localized and of a moderate size. In addition they point out that for 2d, spinwave approach fails above  $T_N/2$  due to the wider range of critical fluctuations present. An EPR study of a Mn layered compound doped with Cd ( 0.1% - 10%), reveals a drastic reduction in the soliton activation energy<sup>35</sup>. For this thesis similar measurements were done but the impurity concentrations were kept low ( $< 1\%$ ), because our goal was to investigate how a single impurity at the soliton center affects the temperature-dependent, critical EPR linewidth.

### 3.2.4 DISCRETENESS OF THE LATTICE

While the Sine-Gordon approximation in the classical continuum limit gave a satisfactory qualitative description of solitons in magnetic chains, it was found inadequate for a quantitative description. One of the parameters responsible for the deviation from ideal behavior was found to be the soliton length scale, which describes the importance of the discreteness of the lattice. Results obtained in the continuum limit are modified by the discrete lattice of the real material<sup>42</sup>. A more detailed investigation showed that instabilities exist owing to the discreteness of the lattice both in FMs and AFMs<sup>43</sup>. Such studies have been extended to vortices in 2d easy plane FM<sup>44,45</sup> as well as XY models<sup>46</sup>, because of their relevance in interpreting dynamic correlation

measurements in neutron scattering experiments.

A continuum field description of a vortex center is found inadequate for any range of parameters. This is because the spins near the vortex "core" vary rapidly over small lengths, which is represented as a singularity in a continuum theory. Wysin<sup>45</sup> has dealt with such singularities by treating the discrete degrees of freedom in the core region exactly on a lattice. Solitons, in general can be well described by a continuum theory, except for certain parameter ranges. This becomes evident upon inspecting the energy derived from the Hamiltonian of equation 3. 2.

By following the procedure outlined for a FM, we obtain the soliton energy as

$$E(r_0) = \frac{E_s r_0^2}{(r_0^2 + r_c^2)} \quad (3.4)$$

where  $r_c \sim 1$  is the lower limit of the radial integration corresponding to the core radius and  $r_0$  is an integration constant representing the soliton size. If the soliton size is large ( $r_0 \gg a$ ) then  $E \simeq E_s$ , which is independent of the soliton size. Also  $\theta(1) \simeq \pi$  meaning that the continuum approximation is valid even at  $r = 0$ . On the other hand, for a small soliton  $r_0 \simeq a$ ,  $\theta(1) \neq \pi$  resulting in a discontinuity in the magnetization. In this case the energy of the core must be calculated, exactly, using eqn. (3.1). The calculation that follows is adapted from the work done by Wysin<sup>46</sup>, in studying the planar vortex stability of an easy-plane magnet.

### 3.2.5 CALCULATION OF THE DISCRETE CORE ENERGY

The total energy of the soliton is split into two parts; one the energy of the region

inside the core radius i.e. the discrete core, and the other from the energy of the surrounding continuum.

$$E(r_0) = E_c(r_0) + \frac{E_s r_0^2}{r_0^2 + r_c^2} \quad (3.5)$$

For the calculation of  $E_c(r_0)$  we have considered a static soliton structure on a square lattice which is defined by discrete lattice sites connected by bonds as illustrated in figure 11. We have assumed that the structure is centered in a unit cell with its origin on a lattice site. The soliton center is at  $(0,0)$  with 4 sites equidistant from the center at  $r_1 = 1$  and  $S_z = m_1 S$  and 4 sites at  $r_2 = \sqrt{2}$  and  $S_z = m_2 S$  and so on. On each circle the values of  $\theta(r)$  and  $\varphi(r)$  are known from the Skyrme solution and they can be used to calculate the energy from the four bonds going out from  $r_1$ .

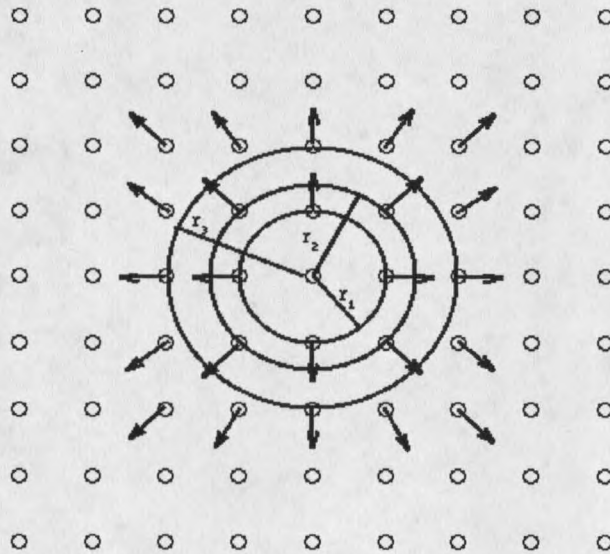


Figure 11. Projection of the spins onto the square lattice at the soliton center. Small circles represent lattice sites.

In the first approximation considering only the lattice sites on the first circle and

using the Hamiltonian of equation (3.1) we obtain the following energy functional for the core.

$$E_{c1} = -4JS^2 \quad (3.6)$$

The next largest core includes the next set of spins with exchange bonds going radially outward from  $r_2 = \sqrt{2}$ . When both sets of spins are included the total core energy now becomes

$$E_{c2} = E_{c1} + 12JS^2 - 8JS^2 \left[ m_2 m_3 + \frac{1}{2} \sqrt{1-m_2^2} \sqrt{1-m_3^2} \right] - 4JS^2 \left[ m_2 m_4 + \sqrt{1-m_2^2} \sqrt{1-m_4^2} \right] \quad (3.7)$$

Here  $m_2$ ,  $m_3$  and  $m_4$  are known in terms of  $r_0$ . The core energy calculation was extended upto sixteen sets of spins yielding  $E_{c16}$ . These calculations and the code that was used to solve the energy equations are shown in Appendix A.

These energies were used to calculate the various spin orientations  $m_n$  in the core region. The extrema of the core energy were determined by the minimization condition  $\frac{\partial E_n}{\partial m_n} = 0$ , where  $n = 1, 2, \dots, 16$ . This resulted in a set of 16 coupled nonlinear equations, whose solutions were obtained numerically. One found that the values of  $m_n$  resulting from the discrete solution were significantly different from the continuum solutions. Finally these  $m_n$  were plugged back in the energy functional expressions, to yield  $E_n$  as a function of the internal parameter  $r_0$ .

Data points were generated using  $E(r_0)$  which is the sum of the energies of the core and the continuum parts of the soliton. Figure 12 shows the core energy plotted

against  $r_0$ . A plot of the total energy  $E(r_0)$  versus  $r_0$  is shown in figure 13a. A numerical

fit to the curve using the function  $f(r_0) = \frac{ar_0^2}{b^2 + r_0^2}$  yields the constants  $a = 12.56$  and  $b =$

0.23.

When a single non-magnetic impurity atom displaces the magnetic atom at the center of the core, exchange pathways with the immediate neighbors are lost without affecting the remaining soliton structure. This means the core energy to the first order

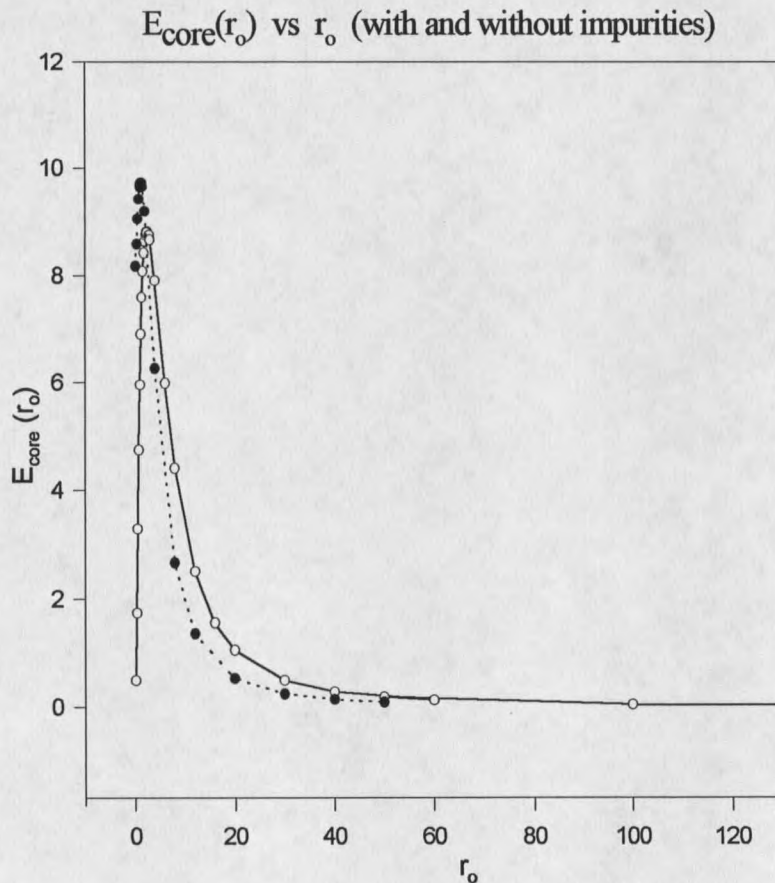


Figure 12. A plot of the core energy vs the size parameter  $r_0$ . The dotted line represents the curve for the soliton core energy without an impurity at the center. The solid line represents the case of a soliton with an impurity.

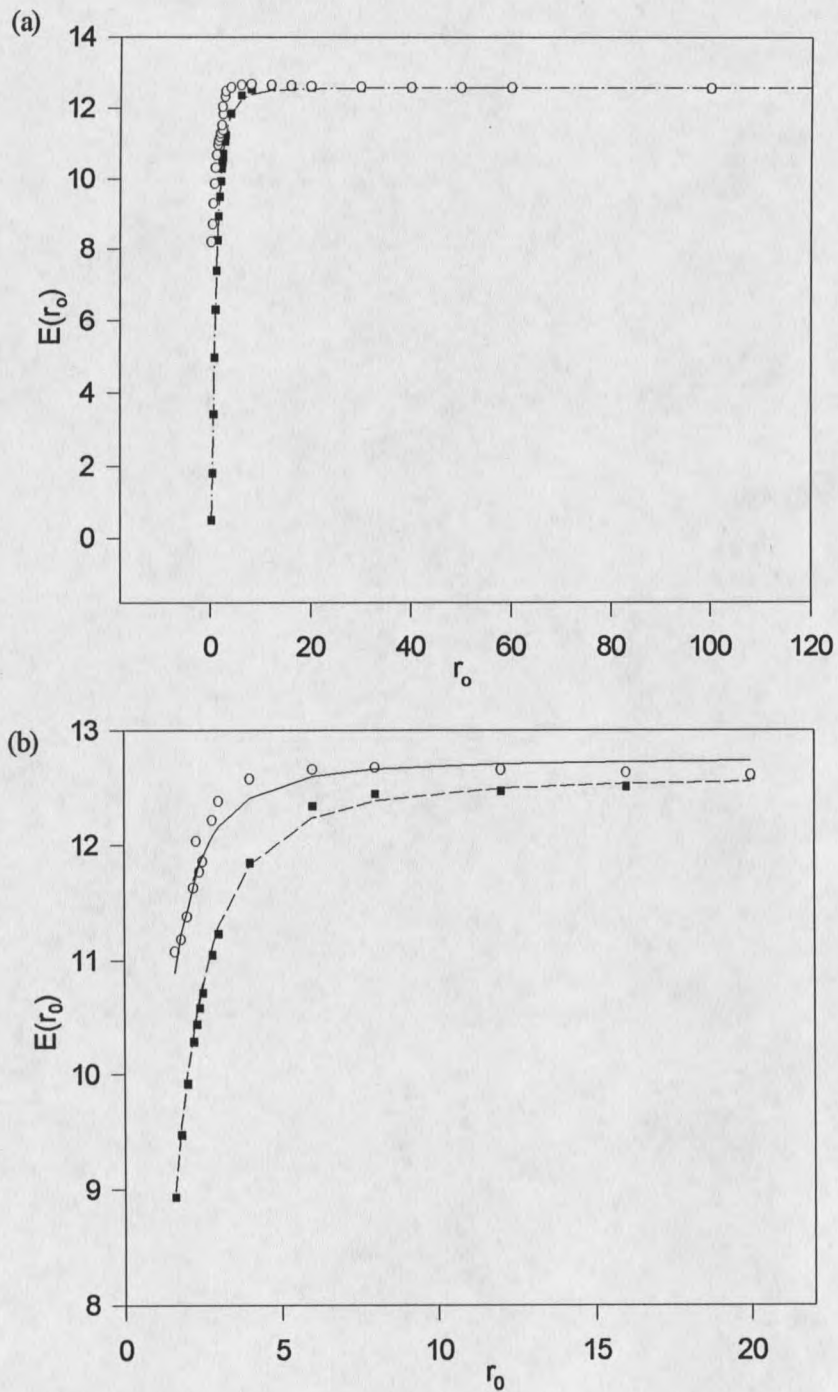


Figure 13. (a) A plot of total soliton energy vs  $r_0$ ,  $\circ$  -- represents a plain soliton.  $\blacksquare$  -- represents an impurity pinned soliton. (b). An expanded view of the above plot indicating the critical value of  $r_0$ .

approximation  $E_{c1}$  reduces to zero, while the other terms remain the same. A similar procedure as described above was repeated with the single impurity-pinned soliton core energy functionals. This procedure yielded the constants  $a = 12.6$  and  $b = 1.01$ . It can be seen, in figure 13b, that the effect of a single impurity, is to reduce the soliton energy and expand the core region. For solitons with  $r_0 \simeq 10$ , the core energy is maximum. For core sizes greater than  $r_0 \simeq 10$ , the effect of the core is negligible. The total energy of a soliton of the same size saturates at the continuum value. This implies that for  $r_0 < 10$ , the effects of the discreteness of the lattice are important and have to be taken into consideration.

### 3.3 EPR LINEWIDTH CALCULATION

This section deals with the calculation of the EPR linewidth from the dynamic correlation function, with the soliton-magnon interaction contributing to the dynamics. We refer back to the equation 2.63, in the last section of Chapter 2, in writing the following expression for linewidth.

$$\Delta H_{\text{crit}}(T) \approx \frac{T}{\chi_{\perp}} \sum_q f_q \operatorname{Re} \int_0^{\infty} dt e^{i\omega_0 t} \langle S(q + q_0, t), S(q + q_0) \rangle^2 \quad (3.8)$$

where  $\omega_0$  is the resonance frequency and  $f_q$  is the Fourier Transform of the dipolar coefficients. The sum over  $q$  is restricted to  $|q|R \leq 1$ .

### 3.3.1 SOLITON-MAGNON INTERACTION

Assuming the soliton-magnon interaction to be the dominant dynamic process in this system, in the fluctuation region above  $T_N$ , the Lagrangian of equation ( 3.3 ) will be solved. The solution will incorporate the change in soliton structure that will affect the soliton structure factor. In the 1d case a theory has been proposed for the soliton-magnon<sup>†</sup> interaction<sup>47</sup>. EPR has been applied to the study of soliton-magnon interference, in order to measure the linewidth with high resolution at  $\vec{q} = 0$  only<sup>48</sup>. Small wavelength magnons interacting with the static solitons manifests themselves in two ways: each soliton passing a magnon will reverse the two sublattices and cause a shift of the magnon phase and there will be a corresponding change in the density of states. In the temperature region of interest, the effect of these shifts on the EPR linewidth is small. We are more interested in the time-dependence that will be introduced in the static soliton structure factor.

The procedure is the same as in Ref 49. The soliton-magnon interaction is treated as a time-dependent perturbation around the static solution. The deviations in the soliton structure are assumed to be very small and can be represented by,  $\theta(r, t) = \theta(r) + \chi(r)\cos\omega t$  and  $\varphi(\phi, r, t) = \phi + \xi(r)\sin\omega t$ .  $\chi(r)$  and  $\xi(r)$  are small perturbations found only in the presence of the soliton. It has been shown that only s-wave scattering contributes mainly to the vortex-magnon interaction<sup>25</sup>. Following a similar argument it is reasonable to assume that  $\chi$  and  $\xi$  are independent of  $\phi$ . Here  $\omega = c|q|$  is the magnon frequency for an AFM. Substituting for  $\theta(r, t)$  and  $\varphi(\phi, r, t)$  in the Lagrangian of

equation (3.3) one gets

$$L = L_0 + L' \text{ where}$$

$L_0$  is the static Lagrangian and  $L'$  is the dynamic Lagrangian given by,

$$L' = \frac{JS^2}{2} \left[ \frac{1}{c^2} (\chi_t^2 + \xi_t^2 \sin^2 \theta_0) - (\nabla \chi)^2 - (\nabla \xi)^2 \sin^2 \theta_0 - \frac{\chi^2}{r^2} \cos 2\theta_0 \right] \quad (3.9)$$

Linearization of the Euler-Lagrange equations resulting from equation (3.9) around the static solution yields,

$$\chi_{rr} + \frac{1}{r} \chi_{rr} + \left( \frac{\omega^2}{c^2} - \frac{1}{r^2} \cos 2\theta_0 \right) \chi = 0 \quad (3.10a)$$

$$\left( \sin^2 \theta_0 \xi_r \right)_r + \frac{\omega^2}{c^2} \sin^2 \theta_0 \xi = 0 \quad (3.10b)$$

Using a rather simple but clever set of transformations the above equations can be solved. They are  $\chi(r) = -\xi(r) \sin \theta_0$  where  $\theta_0$  is the static solution, and  $\xi(r) = rf(r)$  which yield,

$$f_{rr} + \frac{1}{r} (3 - 2 \cos \theta_0) f_r + \left( \frac{\omega^2}{c^2} + \frac{1}{r^2} (1 - 2 \cos \theta_0) \right) f = 0 \quad (3.11)$$

$\theta_0 = 0$  and  $\cos \theta_0 = 1$  corresponds to a case of no soliton. This will reduce the above equation to a Bessel's equation with the solutions  $J_1\left(\frac{\omega}{c}r\right)$  and  $Y_1\left(\frac{\omega}{c}r\right)$  which are magnon solutions. The assumption that the magnons scatter from the outer most region of the soliton, i.e  $r \gg r_0$ , enables us to use the Born approximation to solve equation (3.11). This allows us to use the static soliton solutions as  $\sin \theta_0 \cong 2r_0/r$  and  $\cos \theta_0 \cong 1 - 2r_0^2/r^2$ . Equation (3.11) now reduces to

$$f_{rr} + \frac{1}{r}f_r + \left(\frac{\omega^2}{c^2} - \frac{1}{r^2}\right)f = -\frac{4r_0^2}{r^3}\left(f_r + \frac{f}{r}\right) \quad (3.12)$$

In the light of the approximation used to solve eqn. (3.12) we can see that the term in the right hand side is equivalent to the Born scattering potential. The Green's function of the above can be expressed as,

$$G(r, \tau) = \frac{2}{\pi\tau} \left[ Y_1\left(\frac{\omega}{c}\tau\right) J_1\left(\frac{\omega}{c}r\right) - J_1\left(\frac{\omega}{c}\tau\right) Y_1\left(\frac{\omega}{c}r\right) \right] \quad (3.13)$$

Using the above we can write the solution to (3.11) as  $f(r) = \int G(r, \tau)V(\tau)d\tau$  where

$V(\tau) = -\frac{4r_0^2\omega}{c\tau^3}$  is the scattering potential. Evaluation of the above integral is made

simpler if we assume that the magnon frequency to be so small that  $\omega r/c \ll 1$ . Using the small argument expansion of Bessel functions

$$J_1\left(\frac{\omega r}{c}\right) \cong \frac{\omega}{2c}r \quad \text{and} \quad Y_1\left(\frac{\omega r}{c}\right) \cong -\frac{2c}{\pi\omega r}$$

we have the solution to (3.12) as

$$f(r) = \frac{2\omega_0 r^2}{\pi^2 c r^3} \quad (3.14)$$

Working back through the transformations we have

$$\chi(r) = -\xi \sin\theta_0(r) \quad (3.15a)$$

$$\text{where } \xi(r) = \frac{2\omega_0 r^2}{\pi^2 c r^2} \quad (3.15b)$$

### 3.3.2 CALCULATION OF THE FOUR-SPIN CORRELATION FUNCTION

In this section, we calculate the four-spin correlation function, by taking into account the dynamic properties of the two types of solitons present in the impurity-doped system. This is accomplished by the extension of the techniques used in Ref 49.

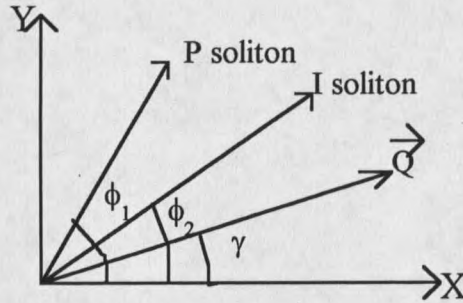


Figure 14. Diagram illustrating the relative angular separation between a magnon, a (pure) P-soliton, and an I-soliton (soliton with an impurity at the center).

If the spin at  $\vec{r}$  is assumed to be from the P-type solitons at  $\vec{R}_\mu$  and the I type (solitons with an impurity at the center) solitons at  $\vec{R}_\nu$ , then the time-dependent spin at  $\vec{r}_i$  is given by,

$$\vec{S}^x(\vec{r}_i, t) = \sum_{\mu} \vec{S}^x(\vec{r}_i, -\vec{R}_\mu, t) + \sum_{\nu} \vec{S}^x(\vec{r}_i, -\vec{R}_\nu, t). \quad (3.16)$$

where the contribution to  $\vec{S}^x(\vec{r}_i, t)$  at site  $i$  comes from the solitons (both P-type and I-type) centered at  $\mu, \nu$ .

$$\text{Here } \vec{S}^x(\vec{r}_i, t) = \frac{1}{2\pi^2} \int g(\vec{Q}, t) e^{i\vec{Q} \cdot \vec{r}} d^2 r \quad (3.17)$$

where  $g(\vec{Q}, t)$  is the structure factor, and  $\vec{Q}$  is the reciprocal lattice vector. Any modifications in the shape or size of the soliton, arising from the magnon interference will affect the structure factor. Since we are interested in the sublattice magnetization

correlation function it is convenient to define the structure factor as,

$$g(\vec{Q}, t) = \int I^x(\vec{r}, t) e^{-i\vec{Q} \cdot \vec{r}} d^2r \quad (3.18)$$

with  $I^x(\vec{r}, t) = S \sin\theta(r, t) \cos\phi(r, \phi, t)$ . Omitting some algebraic steps the structure factor calculation finally leads to,

$$g(\vec{Q}, t) = \int \sin\theta_0 \cos\phi e^{-i\vec{Q} \cdot \vec{r}} d^2r \int \xi(r) \sin\theta \sin\phi \sin\omega t e^{-i\vec{Q} \cdot \vec{r}} d^2r - \int \xi(r) \sin\theta_0 \cos\theta_0 \cos\phi \cos\omega t e^{-i\vec{Q} \cdot \vec{r}} d^2r. \quad (3.19)$$

where the first term is the static soliton structure factor, and the other two terms are the time-dependent terms arising from soliton-magnon scattering. The exponential part of the integral terms may be written as a Bessel function series expansion<sup>50</sup> where  $\vec{Q} \cdot \vec{r} = Qr \cos(\gamma - \phi)$  where  $\gamma$  is the direction of the vector  $\vec{Q}$  relative to the x-axis.

$$e^{i\vec{Q} \cdot \vec{r}} = J_0(rQ) + 2iJ_1(rQ)(\cos\phi \cos\gamma + \sin\phi \sin\gamma) + \dots \quad (3.20)$$

The first term and the higher order terms in equation (3.20) that are of the type  $\left(\frac{\sin}{\cos}\right)_n \phi$ , where  $n > 1$ , do not survive the integration over  $\phi$  in the structure factor calculation. We get the static structure factor in terms of the  $r$  integral,

$$g_0(Q) = 2\pi i \cos\gamma \int_0^R \sin\theta_0(r) J_1(rQ) r dr \quad (3.21)$$

Here  $R$  is the distance over which any two solitons will remain correlated. It is known that the presence of other solitons diminishes the correlations and limits the size of the solitons<sup>22</sup>. It is therefore reasonable to assume that the soliton density is inversely proportional to the correlation length, which is the upper limit of the integral. If the upper limit is extended to infinity this integral is a Hankel-Nicholson type integral which

gives for the static structure factor

$$g_0(Q) = 4\pi i K_1(rQ) r_0^2 \cos\gamma \quad (3.22)$$

where  $K_1(r_0Q)$  is a MacDonald function. A more useful form of  $g_0$  is obtained if again we assume that the system is fluctuating close to the antiferromagnetic wave-vector. Then the small argument expansion for the MacDonald function is used to get the simple expression for the static structure factor

$$g_0(Q) \cong 4\pi i \frac{r_0}{Q} \cos\gamma \quad (3.23)$$

Next we evaluate the dynamic part which is first simplified by the assumption  $\cos\theta_0 \cong 1$   $\sin\theta_0 \cong 2r_0/r$  to get the integral over  $r$

$$g_1(Q, t) = 8\pi i (\cos\omega t \cos\gamma + \sin\omega t \sin\gamma) \int_{r_c}^R \frac{\omega r_0^3}{\pi^2 c r^2} J_1(r, Q) dr \quad (3.24)$$

It is important to note that due to the large  $r$  assumption, it is necessary to introduce a cut-off radius as the lower limit of the integral. Since we are only considering the scattering of magnons from the outer most region of the soliton, this is a reasonable assumption to make in the evaluation of  $g_1(Q, t)$ . Using these, together with the small  $Q$  approximation this integral can be evaluated to give the logarithmic factor  $\ln(R/r_0)$  where  $r_0 < R$ . The dynamic part of the structure factor now becomes,

$$g_1(Q, t) = -\frac{r\omega r_0^3 Q}{\pi c} i \cos(\omega t - \gamma) \ln\left(\frac{R}{r_0}\right) \quad (3.25)$$

For the P and the I solitons, the structure factor differs in the parameter  $r_0$ . The expression for the spin correlation function comes from a generalization of the technique

developed for vortices<sup>45,50</sup>. This enables one to write the correlation function in terms of the structure factor by summing over both the I-type and P-type soliton centers. The most important part of the linewidth calculation is the evaluation of the four-spin correlation function. Using equations (3.16) and (3.17) the four spin-correlation will be

$$\begin{aligned} \langle S^x(\vec{r}_i, t) S^x(\vec{r}_j, t) S^x(\vec{r}_o, t) S^x(\vec{r}_p, t) \rangle = & \langle (\sum_{\alpha} \vec{S}^x(\vec{r}_i, -\vec{R}_{\alpha}, t) + \sum_k \vec{S}^x(\vec{r}_i, -\vec{R}_k, t)) (\sum_{\beta} \vec{S}^x(\vec{r}_j, -\vec{R}_{\beta}, t) \\ & + \sum_l \vec{S}^x(\vec{r}_j, -\vec{R}_l, t)) (\sum_{\gamma} \vec{S}^x(\vec{r}_o, -\vec{R}_{\gamma}, t) + \sum_m \vec{S}^x(\vec{r}_o, -\vec{R}_m, t)) \\ & (\sum_{\delta} \vec{S}^x(\vec{r}_p, -\vec{R}_{\delta}, t) + \sum_n \vec{S}^x(\vec{r}_p, -\vec{R}_n, t)) \rangle \quad (3.26) \end{aligned}$$

where  $\alpha, \beta, \gamma, \delta$  represent P- soliton centers, and  $k, l, m, n$  represent I - soliton centers.

Using 3.17 the above can be written as a sum over the static soliton structure factors.

For example for a sum over the soliton centers  $k, l, \gamma, \delta$  yields,

$$\left\langle g_I(Q_1, t) e^{i(r' - r_k)Q_1} g_I(Q_2, t) e^{i(r'' - r_l)Q_2} g_P(Q_3) e^{i(r''' - r_{\gamma})Q_3} g_P(Q_4) e^{i(r'''' - r_{\delta})Q_4} \right\rangle. \text{ The sum}$$

over the Greek indices is done by the conversion of the sum to an integral with a factor of the soliton density;  $n_P$  for the P-type soliton and  $n_I$  for the I-type soliton. Also the integral definition of the delta-function is used to get terms of the type,

$$\frac{n}{(2\pi)^6} \left\langle \int g(Q_1, t) g(Q_2, t) g(Q_3, 0) g(Q_4, 0) e^{iQ_1 \cdot r_k + iQ_2 \cdot r_l + iQ_3 \cdot r_{\gamma} + iQ_4 \cdot r_{\delta}} \delta(Q_1 + Q_2 + Q_3 + Q_4) d^2 Q_1 \dots d^2 Q_4 \right\rangle \quad (3.27)$$

Higher order terms with higher powers of  $n$ , the soliton density, have been disregarded.

In the expression for the linewidth, the sum over the sites is done subject to the condition

$i \neq j$  and  $k \neq l$ . These result in the additional  $\delta$ -functions,  $\delta(Q_1 + Q_3)$  and  $\delta(Q_2 + Q_4)$  and the resulting expression for the sum will be,

$$\begin{aligned}
& (2\pi)^6 n_P \left[ 2 \langle g_P(Q, t) g_P(Q') g_P(-Q) g_P(-Q') \rangle + 2 \langle g_P(Q', t) g_P(Q) g_P(-Q') g_P(-Q) \rangle \right] \\
& + (2\pi)^8 n_P n_I \left[ 2 \langle g_P(Q, t) g_I(Q) g_P(-Q) g_I(-Q) \rangle + 2 \langle g_I(Q, t) g_P(-Q) g_P(Q) g_I(-Q) \rangle \right] + \\
& + (2\pi)^8 n_I^2 4 \cdot 2 \langle g_I(Q, t) g_I(-Q) g_I(Q) g_I(-Q) \rangle + (2\pi)^6 n_I \left[ 2 \langle g_I(Q, t) g_I(Q') g_I(-Q) g_I(-Q') \rangle \right. \\
& \left. + 2 \langle g_I(Q', t) g_I(Q) g_I(-Q') g_I(-Q) \rangle \right] \quad (3.28)
\end{aligned}$$

### 3.4 SOLITON CONTRIBUTION TO THE LINEWIDTH

The four-spin correlation function obtained above is used in eqn. (3.4) to get a tractable expression for the temperature dependent linewidth. It is now necessary to write the complete expansion for the structure factor upto first order as  $g(Q, t) = g_0(Q) + g_1(Q, t)$ . It is a reasonable approximation in the light of our earlier assumption that  $Q$  is close to the antiferromagnetic wave-vector resulting in  $g_0 \gg g_1$ . This approximation allows us to expand the terms in the correlation function expression. The first term for example, can be written as

$$\begin{aligned}
& (2\pi)^6 n_P \left[ 2 \langle g_P(Q, t) g_P(Q') g_P(-Q) g_P(-Q') \rangle + 2 \langle g_P(Q', t) g_P(Q) g_P(-Q') g_P(-Q) \rangle \right] \equiv \\
& (2\pi)^6 n_P \left[ 2 \langle g_{P1}(Q, t) g_{P0}(Q') g_{P0}(-Q) g_{P0}(-Q') \rangle + 2 \langle g_{P1}(Q', t) g_{P0}(Q) g_{P0}(-Q') g_{P0}(-Q) \rangle \right]
\end{aligned}$$

Due to the exponential, oscillating factor  $e^{i\omega_0 t}$ , only terms with a time-dependent factor will contribute to the linewidth and the other terms will vanish. In ref 49, symmetric decoupling was used for the calculation of the four-spin correlation function. In this

work the decoupling mechanism used here is the RPA( Random phase approximation) wherein  $\delta(Q-Q') = 1$ . It has been argued that this procedure probably overestimates the effects of critical fluctuations near the critical point. Nevertheless, this factorization is used since it allows us to use the standard starting point of the linewidth calculation. The third and the fourth terms are neglected because they contain higher order soliton density terms. The decoupling of the remaining terms in RPA results in,

$$\sim \{4n_P \langle g_{P0}^2(Q) \rangle \langle g_{P0}(Q)g_{P1}(Q) \rangle + 4n_I \langle g_{I0}^2(Q) \rangle \langle g_{I0}(Q)g_{I1}(Q) \rangle + (2\pi)^2 4n_P n_I \langle g_{I0}^2(Q) \rangle \langle g_{P0}(Q)g_{P1}(Q) \rangle\} \quad (3.29)$$

We next substitute for  $g_0(Q,0)$  and  $g_1(Q,t)$  from (3.19) and (3.21) which will enable us to do the thermal averages. We now have for the linewidth,

$$\begin{aligned} (\Delta H)_{sol} \sim \frac{A(k_0)}{(2\pi)^2} 4^5 \pi^2 \langle \cos^4 \gamma \rangle \left\langle \frac{\omega}{c} \right\rangle \langle \cos(\omega t) \rangle \left\langle \frac{1}{Q^2} \right\rangle \left\{ (n_P \langle r_0^2 \rangle_P \left\langle r_0^4 \ln \left( \frac{R}{r_0} \right) \right\rangle_P \right. \\ \left. + n_I \langle r_0^2 \rangle_I \left\langle r_0^4 \ln \left( \frac{R}{r_0} \right) \right\rangle_I \right) + 4\pi^2 n_I n_P \langle r_0^2 \rangle_I \left\langle r_0^4 \ln \left( \frac{R}{r_0} \right) \right\rangle_P \right\} \quad (3.30) \end{aligned}$$

The calculation of the thermal averages that appear within the square brackets will be shown in Appendix B.

### 3.4.1 CALCULATION OF $\langle \cos(\omega t) \rangle$

The EPR resonance frequency  $\omega_0$  is assumed to be very small compared to the magnon frequency  $\omega$  so that the factor  $e^{i\omega_0 t}$  will be neglected. Then the time-

dependence will appear in integrals of the form  $\int_0^{\infty} \cos(\omega(q)t) dt$ . Evaluation of this integral is done following the assumption that magnetization relaxes by diffusion<sup>51</sup>. This has been found experimentally to be true<sup>14,52</sup>. With spin-wave damping the magnon

frequency can be expressed as,  $\omega(q) = c|q| - i\frac{Dq^2}{2}$  where the diffusion constant is  $D \sim$

$R\sqrt{\frac{T}{\chi_{\perp}}}$  and  $c$  is the magnon velocity.

### 3.4.2 CALCULATION OF $\left\langle \frac{\cos^4 \gamma}{Q^2} \right\rangle$

$$\langle \cos^4 \gamma \rangle = \int_0^{2\pi} \cos^4 \gamma d\gamma = \frac{3\pi}{4}$$

Substituting these calculated expressions in (3.30) yields,

$$(\Delta H)_{\text{sol}} \sim \frac{A(k_0)}{(2\pi)^2 \chi_{\perp}} 4^5 \pi^2 \frac{3\pi}{4} \ln R \frac{R}{2c^2} \sqrt{\frac{T}{\chi_{\perp}}} X$$

$$\left[ \int_{1/R}^1 \left[ n_P \langle r_0^2 \rangle_P \left\langle r_0^4 \ln \left( \frac{R}{r_0} \right) \right\rangle_P + n_I \langle r_0^2 \rangle_I \left\langle r_0^4 \ln \left( \frac{R}{r_0} \right) \right\rangle_I \right. \right. \quad (3.31)$$

$$\left. \left. + 4\pi^2 n_I n_P \langle r_0^2 \rangle_I \left\langle r_0^4 \ln \left( \frac{R}{r_0} \right) \right\rangle_P \left\langle \frac{\omega}{c} \right\rangle \frac{dQ}{Q} \right] \right]$$

The lower limit of the  $Q$  integral is limited by the correlation length.

### 3.4.3 CALCULATION OF THE THERMAL AVERAGES

First we calculate  $\left\langle \frac{\omega}{c} \right\rangle$ . In the classical limit  $\left\langle \frac{\omega}{c} \right\rangle = \sum_q n(q)q$  where  $n(q)$  is the Bose

occupation number which can be expressed as  $\frac{T}{cq}$ . Converting this sum to an integral we

$$\text{have } \frac{1}{2\pi} \int_{\pi/R}^{\pi} \frac{T}{c} q \, dq = \frac{\pi T}{c} \sim \frac{T}{c}.$$

#### 3.4.4 CALCULATION OF THE TERMS OF THE TYPE $\langle f(r_0) \rangle$

Here  $f(r_0)$  refers to the soliton size parameter raised to some power. In ref. 49 the evaluation of the thermal averages involved the assumption that the soliton energy  $E_s = 4\pi JS^2$  is independent of the soliton-magnon interaction. However in this work, taking the discreteness of the core into account, the soliton energy has been determined as a function of  $r_0$ . Using the energies calculated in section 3.7 the temperature-dependent soliton sizes are estimated by performing the thermal average

$$\langle r_0^n \rangle = \frac{1}{Z} \sum r_0^n e^{-E(r_0)/T} \quad (3.32)$$

where  $Z$  is the partition function of the system for a single excitation. The sum can be converted to an integral by including a density of states factor  $\frac{dN}{dr_0}$ <sup>27</sup>. It is important to

ascertain the upper limit of the integral while doing the thermal averages. Figure 15 illustrates the radial dependence of the structure of two neighboring solitons. At the edge of the soliton  $r = R$  there appears to be a discontinuity in the radial function

$$\theta(r) = 2 \tan^{-1} \left( \frac{r}{r_0} \right)^{\pm 1}.$$

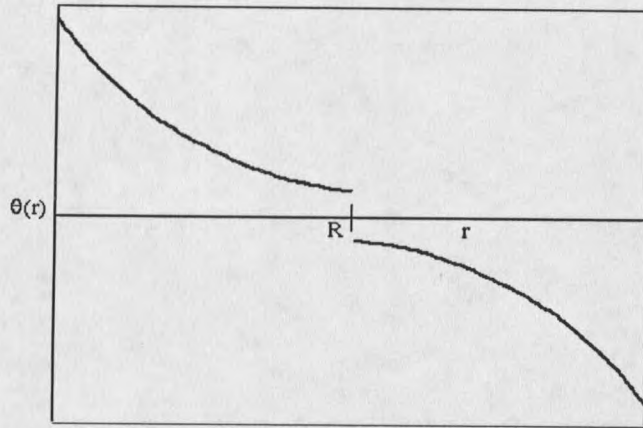


Figure 15. Radial dependence of the structure of a soliton and a neighboring antisoliton.

The left soliton is of the form  $\theta(r) = 2 \tan^{-1} \left( \frac{r_0}{r} \right)$  and the right soliton is of the form

$\theta(r) = 2 \tan^{-1} \left( \frac{r}{r_0} \right)$  with the discontinuity seen at  $r = R$ . This 'gap' at the boundary will

be consistent with the continuum approximation if the condition  $\theta(R) \leq \left| \max \left( \frac{d\theta_0}{dr} \right) \right|$

is satisfied. This constraint limits the  $r_0$  value to  $\sqrt{R}$ . If  $r_0$  is larger than this value, the deviation from the continuum approximation will result in a smaller Boltzmann factor.

Using the above, the sum in (3.28) can be written as

$$\langle r_0^n \rangle = \frac{1}{Z} \int_{r_c'}^{\sqrt{R}} r_0^n e^{-E(r_0)/T} r_0 dr_0 \quad (3.33)$$

where  $Z = \int_{r_c'}^{\sqrt{R}} e^{-E(r_0)/T} r_0 dr_0$ . Since the energy of the soliton  $E(r_0)$  depends upon

whether it is P-type or I-type the thermal averages turn out to be different for each case.

In the partition function calculation,

$$Z = \frac{1}{2} e^{-E_S/T} \left[ \text{Re}^{\sigma/R} - \sigma \text{Ei} \left( \frac{\sigma}{R} \right) - (r_c^2 + r_c'^2) e^{\sigma/(r_c^2 + r_c'^2)} + \sigma \text{Ei} \left( \frac{\sigma}{(r_c^2 + r_c'^2)} \right) \right] \quad (3.34)$$

where  $\sigma = E_S r_c^2/T$  and  $r_c$  is the cut-off radius which decides the boundary between the core region and the continuum region and  $r_c'$  is the lower limit of the integral. When  $r_c = 0.23$  for the P-soliton the first two terms are dominant, while for I-soliton,  $r_c = 1$  and the last two terms are dominant. Evaluation of these integrals for a P-type soliton yields

$$\begin{aligned} \langle r_0^2 \rangle &\sim \frac{R}{2} \\ \left\langle r_0^4 \ln \left( \frac{R}{r_0} \right) \right\rangle &\sim \frac{R^2 \ln R}{6} \end{aligned} \quad (3.35)$$

The calculation of the thermal averages for the I-soliton yields,

$$\begin{aligned} \langle r_0^2 \rangle_I &= \frac{\left[ \frac{2x^3}{\sigma} + R\alpha(\sigma + R) \right]}{(\sigma + \alpha R)} & \langle r_0^4 \ln R \rangle_I &\approx \langle r_0^4 \rangle_I \ln R \approx \frac{R^2 \alpha (2R + \sigma) \ln R}{6(\sigma + \alpha R)} \end{aligned} \quad (3.36)$$

Here  $x = (r_c^2 + r_c'^2)$  and  $\alpha = \exp \left( \frac{\sigma}{R} - \frac{\sigma}{x} \right)$

### 3.4.5 DETERMINATION OF THE SOLITON DENSITY

The soliton density  $n \sim 1/R^2$  in terms of the correlation length<sup>53</sup>, as we have seen before. In our test sample, doped with impurities we have both P- and I- type solitons with densities  $n_p$  and  $n_i$  respectively. Therefore we have,

$$n \sim n_p + n_I \text{ where } n_p = n - n_I \sim \frac{1}{R^2} - n_I.$$

In Ref.45, Mertens *et al* have used a model of a dilute gas of freely moving vortices in the presence of spin waves to study the dynamical correlations of mobile vortices. In order to calculate the number of vortices moving between any two points in space they have used a Maxwellian velocity distribution. In this calculation, however, we have considered solitons in the static approximation. We have used a fundamental assumption of the probability theory in predicting the state of the system in terms of the Boltzmann factor, and the partition function of the system. If  $\rho$  is the concentration of the impurity added to the sample then  $n_I$  may be written as

$$n_I = \rho(1 - P) \text{ where } P = \frac{e^{-E_s/T}}{\frac{\int e^{-E_I/T} r_0 dr_0}{\int r_0 dr_0}} \text{ is the probability of finding a P-soliton in the}$$

system with an energy  $E_s$  at a given temperature. Substitution of the soliton densities and the thermal averages, which gives the temperature and concentration dependent line-width, eqn. (3.31) transforms to

$$(\Delta H)_{\text{sol}} \sim 16\pi A(k_0) X \left( \frac{4\pi}{E_s} \right)^{3/2} X$$

$$T^{5/2} R^2 (\ln R)^2 \left[ \left( 1 - \rho(1-P)R^2 \right) \left( 1 + \frac{8\pi^2(1-P)y}{(\sigma + \alpha R)} \right) + \frac{2\rho\alpha R(1-P)(2R + \alpha)y}{(\sigma + \alpha R)^2} \right]$$

(3.37)

$$\text{where } y = \left( \frac{2x^3}{\sigma^2} + R\alpha(\sigma + R) \right).$$

It is immediately obvious that this expression agrees with Zaspel's<sup>49</sup> calculation for  $\rho = 0$ . If we use Takahashi's<sup>54</sup> expression for the correlation length,  $R \sim \exp(E_s/2T)$ , we find  $\Delta H \sim T^{1/2} \exp(E_s/T)$  which is nothing but the Arrhenius form predicted by Waldner<sup>33,34</sup>. In reference 35, starting with static impurity excitations, the Arrhenius temperature dependence observed in 2d classical Heisenberg magnets was justified. It was however, pointed out that such a temperature dependence was a result of the thermal averaging and not soliton dynamics. In this work an  $\exp(E_s/T)$  temperature dependence for the linewidth has been predicted, by specifically including the effects of soliton dynamics in the form of soliton-magnon interaction. Examining the linewidth expression, it is obvious, that the effect of impurities is to reduce the temperature dependence of the EPR linewidth. It is reasonable to expect this behavior, since in an impurity doped compound, higher energy solitons are replaced by static, low energy, impurity excitations.

### 3.5 MAGNON CONTRIBUTION TO THE LINEWIDTH

A spin wave analysis of the temperature dependence of the EPR linewidth has been worked out by Chakravarty and Orbach<sup>20</sup>, for a  $s = 1/2$ , 2d AFM, in particular for  $\text{La}_2\text{CuO}_4$ . Applying the work done by Huber, Moriya and Kawasaki to a  $s = 1/2$ , quantum Heisenberg Antiferromagnet (QHAF) on a square lattice, they predict that the EPR linewidth would narrow rapidly with increasing temperature, due to the enhanced critical fluctuations.

Starting with the standard expression for linewidth of eqn. (3.8), they have used the RPA to factorize the four-spin correlation function. It has been established that the

Starting with the standard expression for linewidth of eqn. (3.8), they have used the RPA to factorize the four-spin correlation function. It has been established that the dynamic properties of a QHAF are directly related to the low-frequency long wavelength behavior of a classical lattice rotor model (CLRM). Numerical studies by Tyc *et al.*<sup>19</sup>, which utilizes the above mentioned correspondence in conjunction with dynamic scaling and renormalization - group analysis, have predicted the dynamic form factor of a QHAF at low temperatures.

We shall extend the above studies to a classical  $s = 5/2$  system, in order to determine the magnon contribution to the linewidth. According to Tyc *et al.*<sup>19</sup>, the Fourier transform of the two-spin correlation function can be written as,

$$S(q, \omega) = \frac{1}{\omega_0} S(q) \phi(x, \nu) \quad (3.38)$$

where  $\omega_0 = \frac{c}{R} \left( \frac{T}{2\pi\rho_S} \right)^{1/2}$  where  $\rho_S$  is the spin stiffness constant, and  $c$  is the spin-wave velocity;  $x = qR$  and  $\nu = \omega/\omega_0$  are the scaling variables. For a classical magnet  $\rho_S = JS^2$ . The following Lorentzian form of the dynamic scaling function is a result of a molecular dynamics study<sup>19</sup>.

$$\phi(x, \nu) = \frac{\gamma_q}{(\nu - \nu_q)^2 + \gamma_q^2} + \frac{\gamma_q}{(\nu + \nu_q)^2 + \gamma_q^2} \quad (3.39)$$

where  $\nu_q$  is the spin-wave frequency and  $\gamma_q$  is the width. According to renormalization-group analysis the equal time correlation function  $S(q)$  is given by the form

$$S(q) = S(q=0)f(qR) \quad (3.40)$$

$$\text{where } S(q=0) = \frac{B_S R^2 N_0^2}{\left[ \left( \frac{2\pi JS^2}{T} \right) + 1 \right]} \quad (3.41)$$

where  $B_S$  is a universal constant, and  $N_0$  is the value of the order parameter at  $T=0$ .

Fitting  $\gamma_q$  and  $\nu_q$  with suitable expressions with adjustable parameters, we obtain the two-spin correlation function which when plugged into our expression for  $\Delta H$  gives,

$$(\Delta H)_{\text{mag}} \sim \frac{T}{\chi_{\perp}} \sum_q \int_0^{\infty} S^2(q,t) dt. \quad (3.42)$$

$$\sim \frac{T}{\chi_{\perp}} \sum_q \frac{\pi^2}{q^2} S^2(q=0) \frac{1}{4\omega_0} \left[ \frac{1}{\gamma_q} + \frac{\gamma_q}{\gamma_q^2 + \nu_q^2} \right] f^2(qR) \quad (3.43)$$

The sum is converted to an integral and the limits of the integral are subject to the condition  $qR \ll 1$ . Finally using a small  $q$  expression for the static and dynamic scaling functions, we have for the magnon contribution to the linewidth

$$(\Delta H)_{\text{mag}} \sim \frac{A(k_0)}{(2\pi)^2} \frac{T}{\chi_{\perp}} \frac{\pi^3}{2c} \sqrt{\frac{2\pi JS^2}{T}} \left( \frac{T}{JS^2} \right)^4 R^3 \quad (3.44)$$

Comparing the expressions of the linewidth from equations (3.37) and (3.44) it can be readily seen that the magnon contribution to the linewidth goes as  $R^3$  while the soliton contribution goes as  $R^2$ . At first sight it appears as though the spinwave contribution to the linewidth is a dominant factor. But one needs to consider all the temperature dependent terms in the linewidth expression, especially in the critical region before coming to any conclusion. A more careful analysis of the EPR linewidth including both the magnon and soliton contributions will be done in Chapter 5.

## REFERENCES CITED IN CHAPTER 3

1. H.J. Mikeska, *J. Phys.* C11, L29 (1978).
2. M. Steiner, K. Kakurai, and J.K. Kjems, *Z. Phys.* B 53, 117 (1983).
3. H.E. Bethe, *Z. Phys.* 71, 205 (1931).
4. J. D. Johnson, and J.C. Bonner *Phys. Rev.* 22, 251 (1980).
5. H.J. Mikeska, *J. Phys.* C13, 2913 (1980); K. Maki, *J. Low Temp. Phys.* 41, 327 (1980); J.M. Loveluck, T. Schneider, E. Stoll, and H.R. Jauslin, *Phys. Rev. Lett.* 45, 1505 (1980); G. Reiter, *Phys. Rev. Lett.* 46, 202 (1980).
6. J.K. Kjems and M. Steiner, *Phys. Rev. Lett.* 41, 1137 (1978); J. Cibert and Y. Merle d'Auigne', *Phys. Rev. Lett.* 46, 1428 (1981).
7. M. Steiner, *J. Mag. Mag. Mat.* 14, 142 (1979); *ibid.*, 31-34, 1277 (1983).
8. J.P. Boucher., L.P. Regnault, J. Rossat-Mignod, J.P. Renard, J. Bouillot, and W.G. Stirling, *Solid State Commun.*, 33, 171 (1980); J.P. Boucher. and J.P. Renard, *Phys. Rev. Lett.* 45, 486 (1980).
9. K. Sasaki and K. Maki, *Phys. Rev. B*, 35, 257 (1984).
10. A.R. Pereira, A.S.T. Pires and M.E. Gouveau, *Phys. Rev.*, B51, 15, 974 (1995).
11. J.M. Kosterlitz and D.J. Thouless, *J. Phys.* C6, 1181 (1973).
12. J. Tobochnik, and G.V. Chester, *Phys. Rev.* B20, 3761 (1971); D.P. Landau, and K. Binder, *Phys. Rev.* B24, 1391(1981); C. Kawabata and K. Binder, *Solid. State.Com.* 22, 705 (1977); C. Kawabata and A.R. Bishop, *J. Phys. Soc. Jpn.* 52, 27 (1983).
13. N.D. Mermin and H. Wagner, *Phys. Rev. Lett.*, 17, 1133 (1966).
14. M. Uwaha, *Prog. Theor. Phys.*, 63, 2115 (1980).
15. P.M. Richards and M.B. Salamon, *Phys. Rev.* B9, 32 (1974).
16. G. Shirane, Y. Endoh, R.J. Birgeneau, M.A. Kastner, Y. Hidaka, M. Oda, M. Suzuki and T. Murakami, *Phys. Rev. Lett.*, 59, 1613 (1987).
17. H.Q. Ding and M.S. Makivic' . *Phy. Rev. Lett.*, 64, 1449 (1990).

18. A. Auerbach and D.P. Arovas, *Phys. Rev. Lett.*, **61**, 617 (1988).
19. S. Chakravarty, B.I. Halperin and D.R. Nelson, *Phys. Rev.*, **B39**, 2344 (1989).
20. S. Tyc, B.I. Halperin and S. Chakravarty, *Phys. Rev. Lett.*, **62**, 835 (1989).
21. S. Chakravarty and R. Orbach, *Phys. Rev. Lett.*, **64**, 224 (1990).
22. T.G. Castner and M.S. Seehra, *Phys. Rev.* **B47**, 578 (1993).
23. A. A. Belavin, A. M. Polyakov, *Pis'ma v ZhETF* **28**, 503 (1975) [*JETP* **22**, 245 (1975)].
24. S. Trimper, *Phys. Lett.*, **A70**, 114 (1979).
25. M.E. Gouveau, G.M. Wysin, A.R. Bishop and F.G. Mertens, *Phys. Rev.* **B39**, 11840 (1989).
26. B.V. Costa, M.E. Gouveau and A.S.T. Pires, *Phys. Lett.*, **A165**, 179 (1992).
27. C.E. Zaspel, *Phys. Rev.*, **B48**, 926 (1993).
28. A.A. Bogolubskaya and I.L. Bogolubsky, *Phys. Lett.*, **A136**, 485 (1989).
29. F. Waldner, *J. Magn. Magn. Mat.*, **54-57**, 873 (1986).
30. B.A. Ivanov and D.D. Sheka, *Phys. Rev. Lett.*, **72**, 404 (1994).
31. B.A. Ivanov and D.D. Sheka, *JETP*, **80**, 907 (1995).
32. H.J. Mikeska, *J. Phys.* **C13**, 2913 (1980).
33. F. Waldner, *J. Magn. Magn. Mat.*, **31-34**, 1203(1983).
34. F. Waldner, *J. Magn. Magn. Mat.*, **104-107**, 793(1992).
35. T.E. Grigereit, Ph. D Thesis, Montana State University (1993).
36. H.L. Frisch and J.M. Hammersley, *J. Soc. Industr. Appl. Math.*, **11**, 894 (1963); V.K.S. Shante and S. Kirkpatrick, *Adv. Phys.*, **20**, 235 (1971); S. Kirkpatrick, *Rev. Mod. Phys.*, **45**, 574 (1973); D. Stauffer, *Physics Reports* **54**, 1 (1979).
37. P.M. Richards, *Phys. Rev.* **B10**, 805 (1974); E. Siegel, J. Ibrugger and A. Lagendjik, *J. Phys.* **C15**, 4583 (1982).

38. H. Takano and Y. Yokozawa, *J. Phys. Soc. Japan*, **42**, 1059 (1977); W. M. Walsh, R.J. Birgeneau, L.W. Rupp and H.J. Guggenheim, *Phys. Rev.* **B20**, 4645 (1979).
39. A.F.M. Arts, J. van der List, J.G.M. van Miltenburg, C.M.J. van Uijen and H.W. de Wijn, *J. Magn. Magn. Mat.* **31-34**, 1181 (1983).
40. J.A. Van Luijk, A.F.M. Arts and H.W. de Wijn, *Phys. Rev.* **B21**, 1963 (1980).
41. A.F.M. Arts and H.W. de Wijn, "Magnetic Properties of Layered Transition Metal compounds", ed L.J. de Jongh, Kluwer Academic publishers (1990).
42. P.S. Riseborough, D.L. Mills, and S.E. Trullinger, *J. Phys.* **C14**, 1109 (1981).
43. E. Magyari and Thomas, *J. Phys.* **C16**, L535 (1983); P. Kumar, *Phys. Rev.* **B25**, 483 (1982); G.M. Wysin, A.R. Bishop and J. Oitmaa, *J. Phys.* **C19**, 221 (1986).
44. A.R. Völkel, F.G. Mertens, A.R. Bishop and G.M. Wysin, *Phys. Rev.* **B43**, 5992 (1991); F.G. Mertens, A.R. Bishop, G.M. Wysin and C. Kawabata, *Phys. Rev. Lett.* **59**, 117 (1987);
45. F.G. Mertens, A.R. Bishop, G.M. Wysin and C. Kawabata, *Phys. Rev.* **B39**, 591 (1989).
46. G.M. Wysin, *Phys. Rev.* **B49**, 8780 (1994).
47. E. Allroth and H.J. Mikeska, *J. Phys. C: Solid State Phys* **13**, L725 (1980);  
E. Allroth and H.J. Mikeska, *Z. Phys.* **B43**, 209 (1981).
48. Benner et al., *Europhysics Lett.* **3**, 1135 (1987); *J. Magn. Magn. Mat.*, **45**, 354 (1984);
49. C.E. Zaspel, T.E. Grigereit, and J.E. Drumheller, *Phys. Rev. Lett.* **74**, 4539 (1995).
50. A.S.T. Pires, A.R. Pereira, and M.E. Gouveau, *Phys. Rev.*, **B49**, 9663 (1994).
51. L.P. Kadanoff and P.C. Martin, *Ann. Phys.* (N.Y) **24**, 419 (1963).
52. H.R. Boesch, U. Schmockler, F. Waldner, K. Emerson, and J.E. Drumheller, *Phys. Lett.* **36A**, 461 (1971).
53. D.J. Bishop and J.D. Reppy, *Phys. Rev. Lett.* **40**, 1727 (1978); V. Ambegaokar, B.I. Halperin, D.R. Nelson, and E.G. Siggia, *Phys. Rev.* **B21**, 1806 (1980).
54. M. Takahashi, *Phys. Rev.* **B40**, 2494 (1989).

## CHAPTER 4

## 4. EPR MEASURING TECHNIQUE AND EXPERIMENTAL DETAILS

## 4.1 INTRODUCTION

In this chapter we describe some of the experimental details concerning our investigations. The first part is devoted to the description of the spectrometer, in general terms, with which the experiments were carried out<sup>1,2,3,4</sup>.

## 4.1.1 DETECTION OF MAGNETIC RESONANCE

If a magnetic dipole  $\mu = \gamma\mathbf{J}$  is placed in a field  $\vec{B}$ , it precesses about the field with an angular velocity  $\omega_L = \gamma\vec{B}$ . If there is another oscillatory magnetic field  $H_1\cos\omega t$  normal to  $\vec{B}$  the response of the dipole is precession about its direction according to

$$\frac{d\vec{\mu}}{dt} = \gamma(\vec{\mu} \times \vec{B}) \quad (4.1)$$

For an electronic dipole  $\gamma = -g(e/2m)$  so that for  $\vec{B} = 3300$  Gauss the frequency is  $\omega_L/2\pi = 9.2$  Ghz.

The electronic magnetic dipole moment of a free atom is  $\mu = -g\mu_B\vec{S}$  and the Hamiltonian for its Zeeman interaction with a field is

$$\mathcal{H} = -(\mu \cdot \vec{H}) = g\mu_B(\vec{H} \cdot \vec{S}) \quad (4.2)$$

For a stationary state whose magnetic quantum number is  $M$ , the magnetic field  $\vec{H}$  gives rise to  $2S + 1$  equal spaced energy levels namely

$$E_M = g\mu_B H M \quad (4.3)$$

and transitions between the energy states of the spin system of the type  $\Delta M = \pm 1$  are allowed if the following resonance condition is satisfied.

$$h\nu = g\mu_B H \quad (4.4)$$

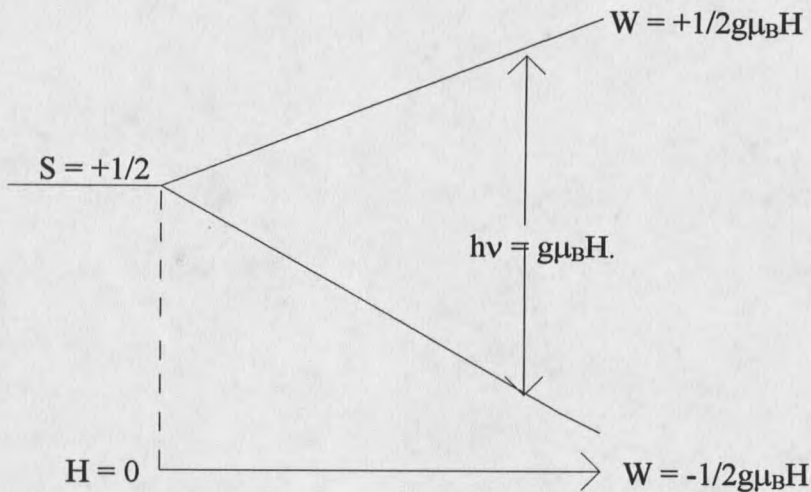


Figure 16. Zeeman energy splitting in a magnetic field.

There are two kinds of processes taking place in paramagnetic resonance: the radio frequency field tends to equalize the populations of the various magnetic levels, and the internal interactions tend to restore the Boltzmann distribution. In order to maintain the thermal equilibrium, some excited electrons must fall back down, releasing energy by interacting with the lattice or with each other. The rate of the process in which equilibrium is established between the spin system and the lattice is characterized by the spin-lattice relaxation time  $T_1$ . The process of establishing an equilibrium within the spin system, characterized by the spin-spin relaxation time  $T_2$ , consists of an exchange of energy within its various parts, while conserving the energy of the system. These spin-spin relaxation times and spin-lattice relaxation times can be used to study the spin dynamics of the system. In a standard continuous wave spectrometer the power

level is not high enough to saturate the system. In pulsed EPR measurements the sample is exposed to a very high-power short duration pulse of microwave energy and the strength of the decay rate of the induced magnetization is measured from which the relaxation times can be extracted.

Every EPR spectrometer consists of the following basic parts: 1) a microwave oscillator (klystron) with stabilized frequency and power supply; 2) an absorption cell in the form of a rectangular cavity resonator; 3) a detector; 4) an amplifier and recording device; 5) a source of a steady magnetic field; and 6) a system for the modulation of the steady magnetic field. The central part of each EPR equipment is the resonance cavity, in which a standing wave pattern of electromagnetic wave is generated. To this purpose, microwaves are transmitted from a klystron via waveguides to the cavity, which is coupled to the wave-guide system by means of a coupling hole (iris) or by an antenna. When magnetic resonance occurs the sample absorbs energy from the microwave field at a rate per unit volume given by

$$\bar{P} = \frac{1}{2} \omega H_1^2 \chi'' \quad (4.5)$$

where  $\omega$  is the microwave frequency and  $\chi''$  the imaginary part of the dynamic susceptibility.

For our experiments reflection type cavities have been used. A cavity of this type may be considered as an impedance  $z$  which terminates the waveguide. This impedance obeys

$$z = \frac{\beta}{1+i\delta} \quad (4.6)$$

where  $\beta = \frac{Q_0}{Q_{\text{ext}}}$  and  $\delta = Q_0 \left( \frac{\omega}{\omega_0} - \frac{\omega_0}{\omega} \right)$ . Here  $Q_0$  denotes the unloaded quality

factor, defined by

$$Q_0 = 2\pi \frac{\text{energy stored in the cavity}}{\text{energy lost in the cavity per period}} \quad (4.7)$$

$Q_{\text{ext}}$  denotes the external quality factor, defined in an analogous way as  $Q_0$ , but with energy lost outside per period in the denominator of expression (4.7). The ratio of the power absorbed by the sample under investigation to the power dissipated in the cavity itself equals

$$P/P_0 = 4\pi\chi''Q_0/V \quad (4.8)$$

The loaded quality factor,  $Q_L$ , is the quality factor of the resonance cavity coupled to the waveguide, and is related to  $Q_0$  and  $Q_{\text{ext}}$  by

$$Q_L^{-1} = Q_0^{-1} + Q_{\text{ext}}^{-1} \quad (4.9)$$

For reflection cavities  $Q_L$  is generally of the order of  $10^3$ . The parameter  $\beta$  is called the coupling parameter; when  $\beta = 1$ , the energy losses inside and outside the cavity are equal and the cavity is critically coupled to the waveguide. In that case,  $Q_L = 0.5Q_0$ . Finally,  $\omega_0$  denotes the microwave frequency for which impedance is maximal; from equation (4.6) one can infer, that for large  $Q_0$ , the impedance has a pronounced peak around  $\omega = \omega_0$ ;  $\omega_0$  is therefore called the resonance frequency of the cavity. Another important parameter is the reflection coefficient  $\Gamma$ ; this is a complex number, the absolute value of which describes by definition the ratio of the amplitudes of the reflected and incident waves. The argument of  $\Gamma$  represents the phase shift of the reflected wave. The

reflection coefficient is related to the impedance of the cavity by

$$\Gamma = \frac{z - 1}{z + 1} \quad (4.10)$$

Energy absorption by a sample inside the cavity leads to a reduction of the quality factor, given by

$$\Delta Q_L = 4\pi\eta\chi''Q_L^2 \quad (4.11)$$

Variation of the external field near magnetic resonance will also produce a change in the real part of the dynamic susceptibility  $\chi'$ , as  $\chi'$  and  $\chi''$  are coupled. This leads to a change in  $\omega_0$  given by

$$\Delta\omega_0 = 2\pi\eta\chi'\omega \quad (4.12)$$

The parameter  $\eta$  which occurs in the above equations is the cavity filling factor, defined by

$$\eta = \frac{\int_{\text{sample}} H_1^2 dV}{\int_{\text{cavity}} H_1^2 dV} \quad (4.13)$$

and can be maximized by placing the sample at a position inside the cavity where  $H_1$  is maximum. An EPR experiment has to be carried out in such a way, that only  $\chi''$  is measured, i.e. the influence of  $\chi'$  on  $\Gamma$  can be eliminated. This may be achieved by keeping the klystron frequency tuned to the cavity frequency. Under these conditions the reflection coefficient obeys

$$\Gamma \cong \Gamma_0 + 8\pi\eta\chi''Q_L \frac{\beta}{(1 + \beta)^2} \quad (4.14)$$

the reflected wave via a directional coupler to a rectifying crystal detector. When the output voltage of this detector is proportional to the amplitude of the reflected wave, i.e.

to  $\chi''$ , the detector is linear. This way of detecting resonance is referred to as homodyne. A more sensitive method is obtained by superheterodyne detection ; in this case a second microwave signal is mixed with the signal which is reflected by the cavity. It is based on the use of a balanced bridge, which receives power from the klystron with a frequency  $\omega'$  and from the auxiliary klystron with a frequency  $\omega$ . When a constant frequency difference  $(\omega' - \omega)$  between the two signals is maintained, the detector voltage has a component with an amplitude proportional to  $\chi''$  and with fixed frequency  $(\omega' - \omega)$ . By amplifying the signal with an ac amplifier with small bandwidth around  $(\omega' - \omega)$  and by subsequent rectification, one can obtain an important increase in sensitivity compared with homodyne detection. The mixing of two frequencies is achieved by using two microwave sources and an Automatic Frequency Control (AFC) between them.

The effects of noise inherent in the crystal detector and in the klystron can be reduced by the technique of field modulation. If a small magnetic field sinusoidally varying at an audio or radio frequency is superimposed on  $H_0$ , a component of detector current at that frequency will in general exist in the neighborhood of the resonance. In fact, if the modulation amplitude is smaller than the magnetic resonance width, a simple Taylor expansion shows that this component will be proportional to the derivative of  $\chi''$  with respect to  $H_0$  or  $\omega_0$ . By mixing this signal with a reference signal at the modulation frequency, a d-c signal will be obtained proportional to  $d\chi''(\omega_0)/d\omega_0$ . Although the derivative response is sometimes inconvenient to interpret, this technique has one important advantage—it accepts only the noise within a narrow bandwidth near the modulation frequency. The derivative absorption curve is actually more sensitive to slight tendencies

toward structure in the curve of  $\chi''$  versus frequency than is the  $\chi''$  curve itself.

If one modulates the magnetic field at a high frequency, e.g. 100 KHz, one may obtain a better sensitivity employing phase sensitive detection. The mode of operation is briefly described below.

Energy is fed into the hybrid tee bridge from the klystron and is split equally between the side arms. One arm feeds energy to the resonant cavity and the other arm carries components which reflect back a reference wave, adjustable in amplitude and phase. These two reflected waves are detected in the fourth arm of the hybrid tee. In the off-resonant condition the reference signal is equal in amplitude and opposite in phase to the reflection from the sample and cavity, so balancing out cavity reflection and sending zero power to the crystal detector in the fourth arm. In practice, the cavity is matched by a matching element that is placed near to the cavity, so at this stage the reference wave should be zero. When resonance occurs an off-balance signal is detected.

In practice, the best signal-to-noise ratio of the crystal detector is obtained by working higher up the slope of the crystal characteristic, and for this reason the reference arm is allowed, under off-resonant conditions, to reflect back a small signal so that when the EPR signal is obtained, the crystal is working at the optimum slope of its characteristic. There is also another reason why it is necessary to unbalance the bridge slightly. A completely balanced bridge will detect both  $\chi'$  and  $\chi''$ . It is only by allowing a small off-balance current that one may distinguish between  $\chi'$  and  $\chi''$ , as off-balance in amplitude alone can detect  $\chi''$ , a change in which gives rise to pure absorption, while off-

balance of phase will detect  $\chi'$ , which signifies a change in the dispersion.

#### 4.1.2 PARTS OF THE SPECTROMETER

An overall scheme of the 9.3 GHz spectrometer is described in the following. The microwaves that are generated by a water cooled Varian E102 reflex klystron, are directed via an isolator, a calibrated variable attenuator, and a directional coupler to the resonant cavity. The reflected signal passes through the other arm of the coupler to the detector diode. The frequency of the klystron can be adjusted in a coarse way with a tuning screw. A more subtle way of doing this will be to use the klystron reflector voltage. In order to keep the klystron tuned to the cavity frequency during an experiment, the reflector voltage is regulated through the feedback circuit involving the part marked AFC circuits. A signal of this frequency is superimposed with the output of the main klystron; any change in  $\omega_0$  leads to phase shift of the signal at the detector diode, which is detected by the AFC and converted into a dc output voltage; this will adjust the primary klystron frequency via the klystron power supply. The frequency is measured by HP 5246L frequency counter. Microwaves generated by a secondary klystron are guided via a directional coupler to the detector diode. To allow superheterodyne mixing of the two signals arriving at the diode a constant frequency difference of 70 KHz is maintained. This is done by a second feedback loop in the part named 'AFC circuits'. Parts of the two signals are branched off to the detector which detects a signal component with a frequency equal to the difference of the two incident

frequencies. This signal is amplified and compared with a standard frequency by means of a discriminator. Its output voltage adjusts the secondary klystron reflector voltage via the power supply. This signal is detected in such a way, that a direct absorption curve  $\chi''(H)$  or a first-derivative curve  $\partial\chi''/\partial H$  is obtained.

The external magnetic field is provided by a rotatable iron-pole (VarianV-7200) magnet; it may be varied continuously up to 10 KG. The field strength can be measured via the current through the magnet. For accurate measurement of the field, used in g-value measurements, a NMR gaussmeter is used. It is a precision magnetic flux measuring instrument used with Hall effect magnetic field probes placed close to the cavity.

The sample is cooled with an Oxford ESR-900 continuous flow through cryostat which is equipped with a heater coil that is controlled by an Oxford ITC4 temperature controller using a gold + 0.03% iron vs chromel thermocouple. Temperatures in the range of 4.2K and 300K were measured by a carbon glass resistor attached to the sample rod and placed within 1 mm of the crystal in the microwave cavity. The resistor has little or no magnetic field dependence for the field range generated by the electromagnet. Temperature stability to within 2% could be obtained.

A vacuum of the order of  $10^{-5}$  Torr was maintained in the double-walled space of the cryostat using a Leybold-Heraeus turbopump with a Welch mechanical roughing pump in line. A larger Compton pump was used to pump the liquid He through the cryostat. In addition, the He flow through the sample space was controlled with a manual valve which lies in line the mechanical pump that draws the liquid Helium into

the sample space. This needle valve is so sensitive that it could be used to control the liquid He flow and hence the temperature of the sample space.

Current to the carbon-glass resistor is supplied by a laboratory made current source. The output of the resistor is directed to a Fluke digital voltmeter that was connected to the PC via an IEEE data bus for conversion to temperature units and display of the same. A HP 5246L Electronic Counter in conjunction with a HP 5257A Transfer Oscillator plug-in unit was used for the microwave frequency measurement.

For additional calibration purposes a single crystal of  $\text{MgO: Cr}^{3+}$  is mounted inside the cavity. A  $g$ -value for  $\text{Cr}^{3+}$  in the octahedral symmetry of this crystal is known<sup>5</sup> to be  $1.9800 \pm 0.006$  allowing precise field and/or frequency determination to be made. The free electron  $g = 2$  resonance occurs at a field of 3322 Gauss for a frequency of 9.3 GHz.

## 4.2 DESCRIPTION OF THE INVESTIGATED SAMPLE

### 4.2.1 CRYSTAL STRUCTURE OF PAMC

N-propyl ammonium manganese tetrachloride or shortly PAMC is the compound chosen for our experiments. The lower half of the unit cell is as shown in figure 17. The structure consists of layers of Manganese ions coupled antiferromagnetically, and separated by alkyl ammonium groups. Each Mn ion is surrounded by four Cl ions according to the crystal structure analysis<sup>6</sup>. The crystal structure is orthorhombic, space group  $\text{CmCa}$  with four magnetic ions per unit cell. There are two  $\text{Cl}_2$  atoms situated above and below but do not participate in the superexchange interaction. Thus layers of

corner sharing  $\text{MnCl}_6^-$  octahedra are obtained.

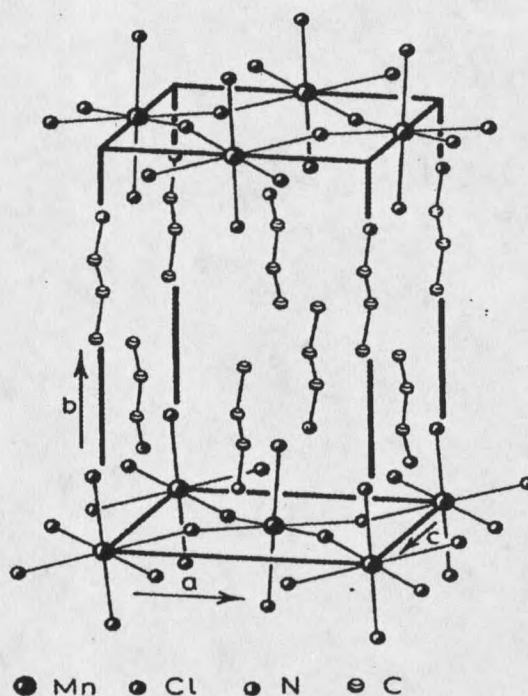


Figure 17. Lower half of the unit cell of PAMC. Only the carbon atoms of the propyl group are shown<sup>6</sup>.

The  $\text{NH}_3$  ions form hydrogen bonds with three  $\text{Cl}_2$  ions of the  $\text{MnCl}_6^-$  octahedra. This causes the distorted metal-halogen octahedra to be tipped by  $8^\circ$  away from the crystallographic axis orthogonal to the layers. The unit cell dimensions are<sup>6</sup>  $a = 7.2 \times 10^{-10} \text{ m}$ ,  $b = 25.94 \times 10^{-10} \text{ m}$ ,  $c = 7.51 \times 10^{-10} \text{ m}$ . The crystal platelets are easy to cleave into small sheets parallel to the 010 plane. The surface of the platelets is almost a square, the 'a' and the 'c' axis falling along the two diagonals.

The structural properties of PAMC decide its magnetic behavior. The deviation of the pure 2d magnetic character is expressed by the ratio of the intralayer coupling  $J$  to

the interlayer exchange coupling  $J'$   $|J'/J| \approx 10^{-6}$ . Dipolar broadening is ascribed to be the main source of anisotropy, which leads to the idea that b-axis is the easy axis of magnetization. The Neel temperature<sup>8</sup>  $T_N$  for the antiferromagnetic ordering is 39.2K, while the intralayer exchange coupling<sup>8</sup> is known as -9K at 80K. Compared to other members of the series of metal-organic compounds  $(C_nH_{2n+1}NH_3)_2MnCl_4$ ,  $n = 1, \dots, 9$ , PAMC has low anisotropy<sup>7</sup>. PAMC is known to show weak ferromagnetism<sup>8</sup> below 39.2K due to canting of the spins by  $0.05^\circ$ .

#### 4.2.2 CRYSTAL GROWTH AND CONCENTRATION MEASUREMENT

The doped samples  $(C_3H_7NH_3)_2M_xMn_{1-x}Cl_4$  were grown by the traditional method of slow evaporation of a solution of all the salts mixed in stoichiometric proportions. While the Cd and the Zn doped samples were grown from aqueous solutions, the solvent used for growing the Mg doped crystals was 95% ethanol. Since we are working with doping concentrations  $< 1\%$  a solvent with a very high degree of purity was used. PAMC crystallizes as faint pinkish orange platelets which had to be washed in ice cold ethanol and air dried. The dimensions of the crystals varied from  $2\text{mm} \times 2\text{mm} \times 0.2\text{mm}$  to  $5\text{mm} \times 5\text{mm} \times 0.6\text{mm}$  depending upon the conditions of growth. The crystal masses ranged from less than 1mg to 10mg. Typically the sizes of the crystals used in EPR experiments were  $2\text{mm} \times 2\text{mm} \times 0.2\text{mm}$ .

The thermal gradient method was attempted to grow large and heavier crystals. Large and clean crystals could be grown but the dilution was not very effective, probably because of the slower diffusion rate of the heavier dopants Zn and Cd. The dilution

strengths of Cadmium and Magnesium that are reported here were measured by Galbraith laboratories. The Zinc concentrations were measured in the MSU Chemistry Laboratory using gravimetric analyses. The error bar shown in the impurity concentrations due to chemical analyses is nearly 10% for  $x = 0.001$  and goes down as the doping concentration increases. Several batches of crystals were prepared, but the data for the crystals used in the EPR experiments only will be reported here.

It is expected that the crystallization curve (the ratio of Cd/Mn in the crystal plotted vs the ratio of Cd/Mn that goes into the solution) is symmetric but at some higher level Cd would prefer to remain in solution. While Cadmium was found to be present in the single crystal in concentrations roughly an order of magnitude higher than the molar ratio in solution, the contrary was the case with Magnesium doped crystals. It is known that compounds with the general formula  $(C_nH_{2n+1}NH_3)_2MCl_4$ , with  $M = Mn$  or Cd can be synthesized in the laboratory. It is therefore not surprising to find Cd go readily into the crystal as it crystallizes with the same symmetry as Mn. Zn doped crystals seemed to contain slightly higher concentrations of Zn than that was put into solution. It was noted, however, that in the case of Mg, at all levels of concentration the amount of dopant in the crystal is less than the amount that goes into solution. This could be due to the dopant having a greater solubility than Mn.

### 4.3 ANISOTROPY MEASUREMENTS

The angular dependence of the linewidth was measured for the pure compound and two other samples of doped PAMC. Since the impurity concentration levels are well

below the percolation threshold, no angle dependence was expected as a function of concentration<sup>9</sup>. The linewidth as a function of angle was measured for each sample at temperatures below 80K. The linewidth  $\Delta H$  was plotted as a function of  $\theta$ , the angle between the applied field and the b-axis. These plots are shown in figures 18, 19, and 20. The linewidth has a maximum when H is directed normal to the ac plane and decreases with increasing  $\theta$ , and reaches a minimum at  $\theta \approx 35^\circ$ . This effect, which is a manifestation of diffusive behavior, is largely observed<sup>7,9</sup> in the temperature range 300K to 70K and the angular dependence is proportional to  $(3\sin^2\theta - 1)^2$ .

In all the three samples measured below  $T \approx 56K$ ,  $\Delta H$  at  $\theta \approx 35^\circ$  becomes larger than  $\Delta H$  at  $\theta \approx 90^\circ$ . At these temperatures the angular dependence changes from  $(3\sin^2\theta - 1)^2$  to roughly  $(1 - \sin^2\theta)$ . Such a change in the angular dependence has been observed for some manganese layer-type compounds<sup>7,10-13</sup>. According to Richards and Salamon this may be regarded as an indication of the range of the dominating q modes changing from  $q \approx 0$ ,  $t \rightarrow \infty$  diffusive behavior to  $q \approx q_0$ , when the fluctuations are in the staggered magnetization mode<sup>14</sup>. The purpose of the low temperature anisotropy experiments was to determine at what temperature this occurs.

The angular anisotropy in these crystals at temperatures  $T < 65K$  can be expected to follow<sup>15</sup>

$$\Delta H(\theta) = (a - b\sin^2\theta). \quad (4.15)$$

The data are shown in figures 21 to 24. Quantitative agreement with the data is reasonably good as seen by the dotted line fit. The results of the fits are summarized in

Table 1. Misalignment of the angular scale mounted on the sample holder and the error bars in the temperature measurement may be regarded as the chief sources of error. It was observed in the case of  $K_2MnF_4$  that at  $T = 1.2T_N$  the angular dependence showed the expected  $(1 - \sin^2 \theta)$  behavior<sup>10</sup>. In our measurements, since we were above this temperature limit the misalignment of the fit is not surprising.

Table 1. Summary of the anisotropy parameters for the pure and the doped samples of PAMC at  $T < 65K$ , obtained by fitting  $(a - b \sin^2 \theta)$  to the linewidth  $\Delta H(\theta)$ .

Name of the impurity	Temperature K	a	b
none	56.4	36.0	6.4
Cd	52.5	20.8	5.05
Mg	58	35.9	5.76
Mg	52	98.1	22.3

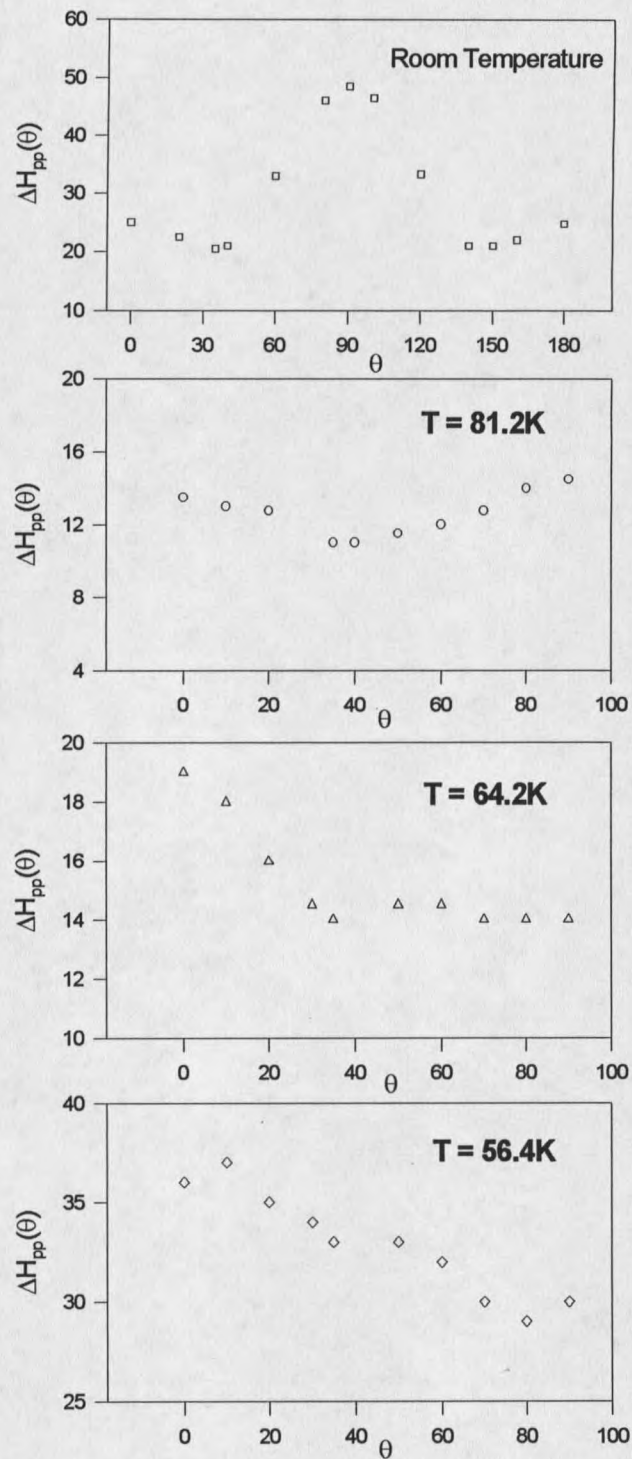


Figure 18. Angular variation of the EPR linewidth of pure PAMC at various temperatures.

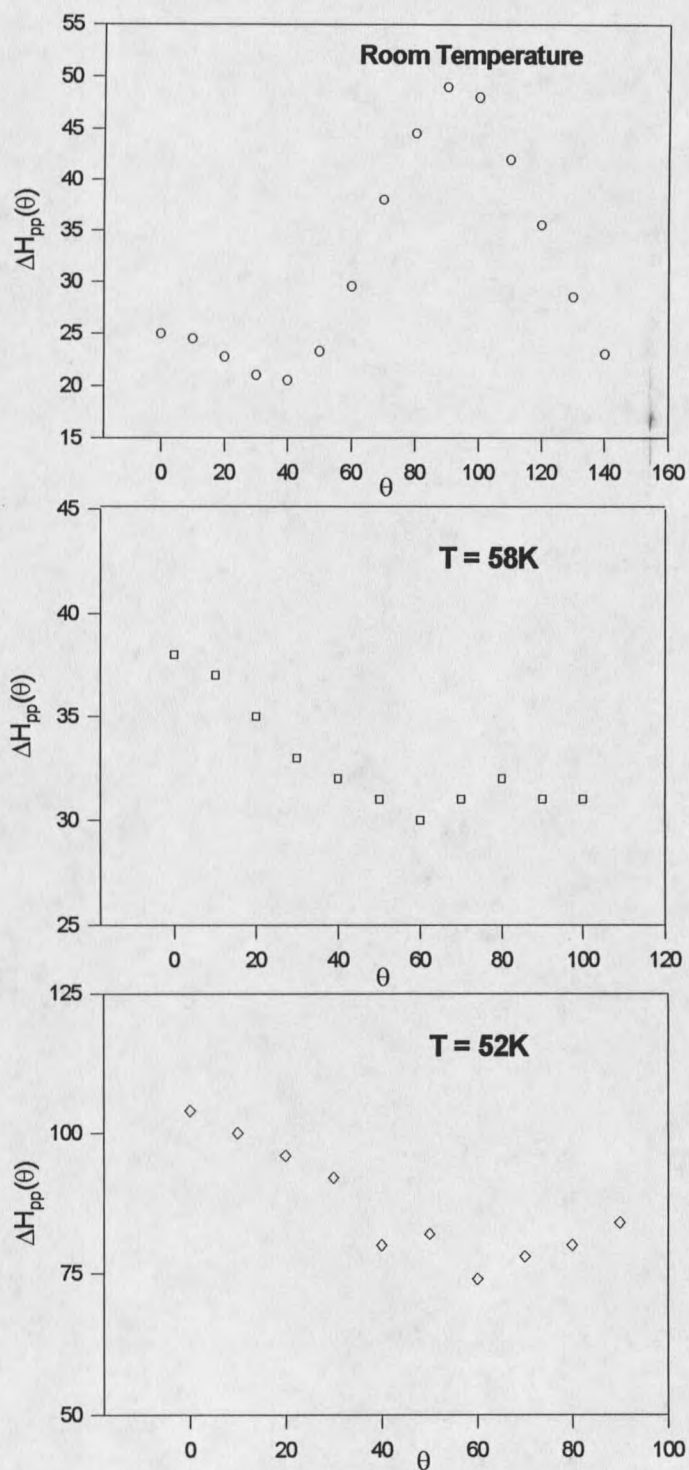


Figure 19. Anisotropy of PAMC with some magnesium as an impurity, at various temperatures.

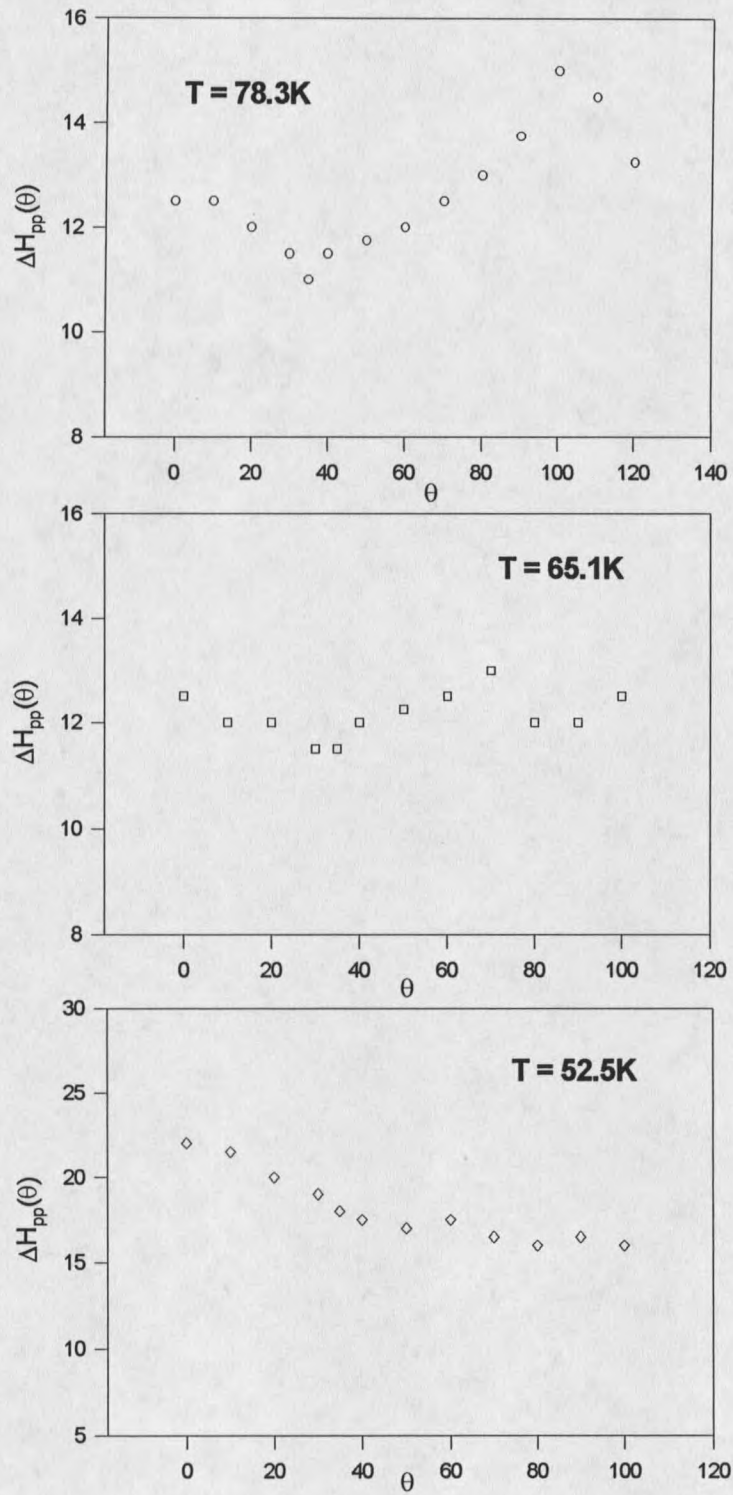


Figure 20. Anisotropy of PAMC with some Cadmium as an impurity, at various temperatures.

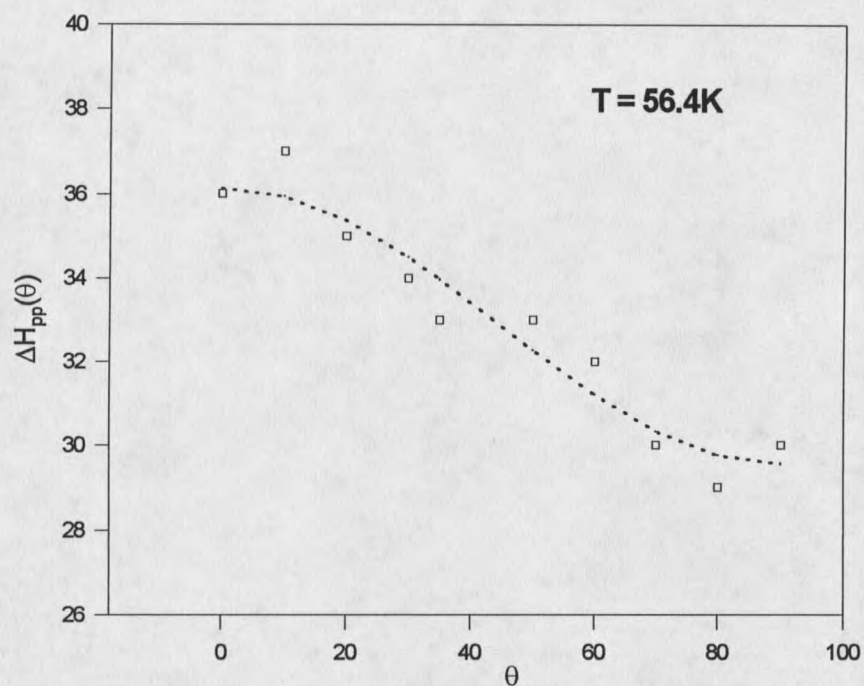


Figure 21. Anisotropy of PAMC with no impurity at  $T = 56.4\text{K}$ . The dotted line corresponds to the fit of equation 4.15.

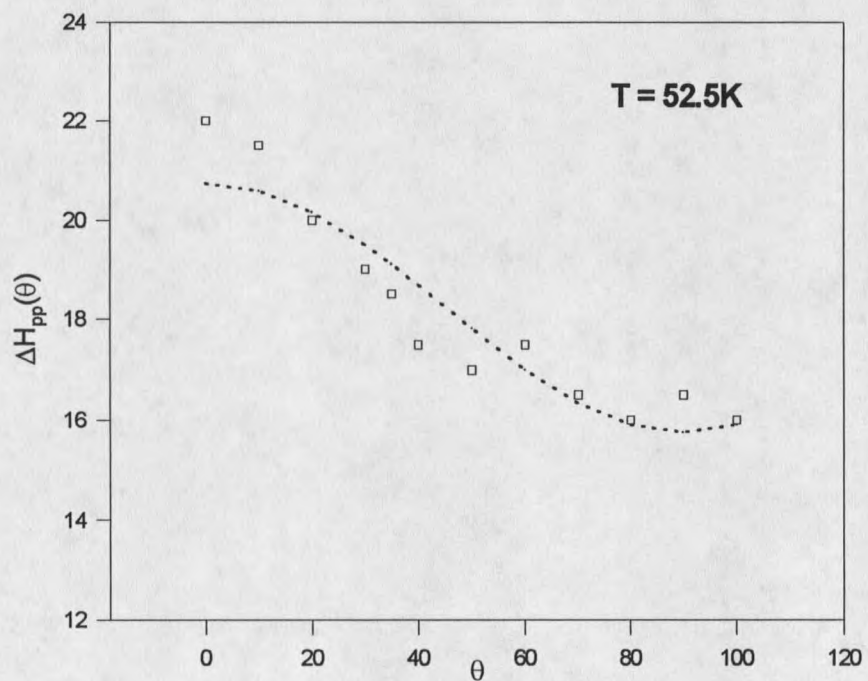


Figure 22. Anisotropy of PAMC with some Cadmium at  $T = 52.5\text{K}$ . The dotted line corresponds to the fit of equation 4.15.

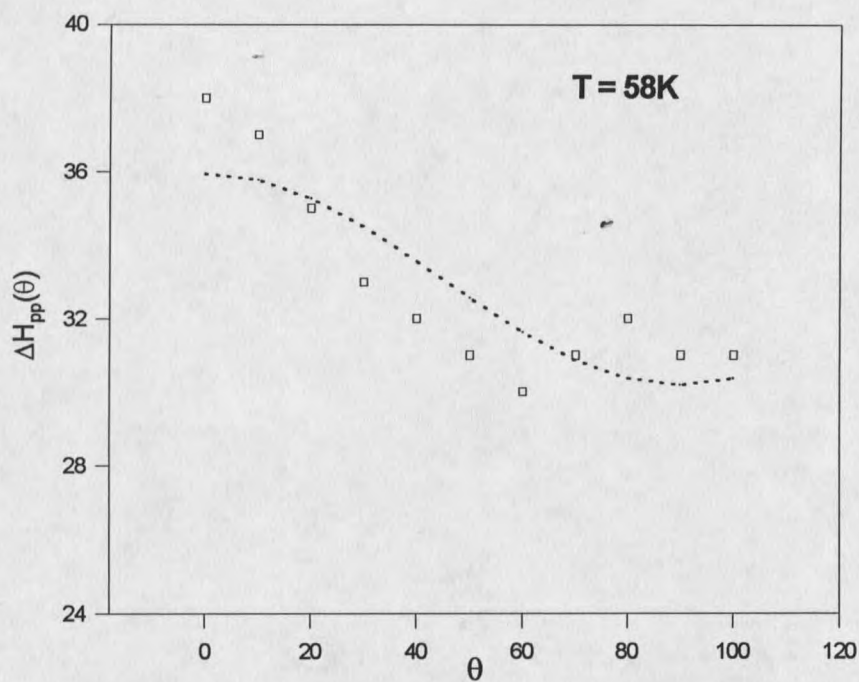


Figure 23. Anisotropy of PAMC with some Magnesium at  $T = 58K$ . The dotted line represents the fit of equation 4.15.

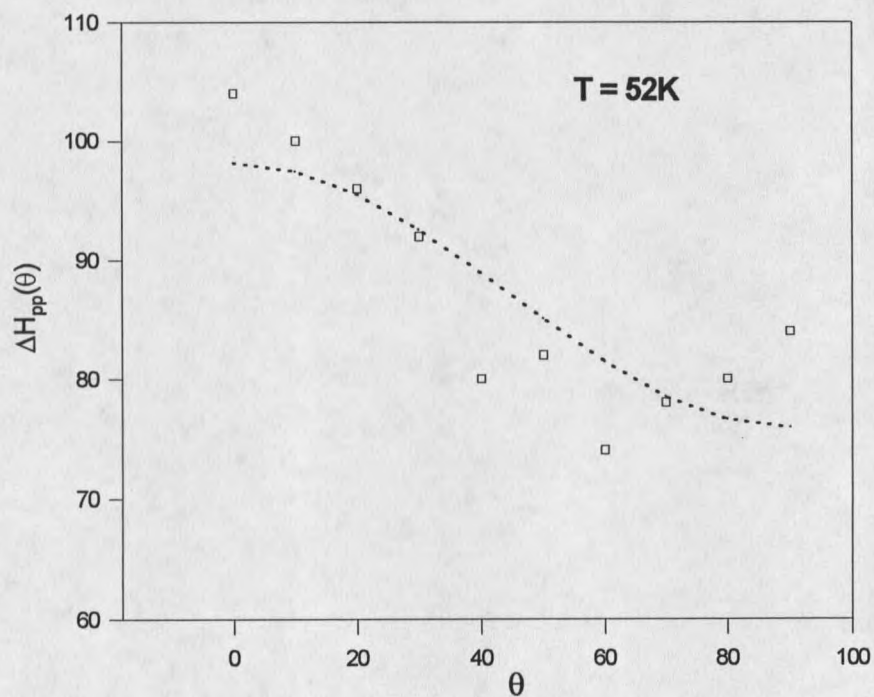


Figure 24. Anisotropy of PAMC with some Magnesium at  $T = 52K$ . The dotted line represents the fit of equation 4.15.

## 4.4 LINEWIDTH MEASUREMENTS

Linewidth as a function of temperature was measured for several samples of impurity (Cd, Zn, Mg) doped crystals. The impurity concentrations in all the three cases were well below the percolation threshold. The linewidths were measured by hand and entered into the computer manually. Each experiment has three graphs associated with it.  $\Delta H$  vs  $T$  over the whole temperature range of interest, natural log of  $\left(\frac{\Delta H(T)}{\Delta H_{\infty}}\right)$  versus  $\left(\frac{T_N}{T}\right)$  over the whole temperature range and  $\ln\left(\frac{\Delta H(T)}{\Delta H_{\infty}}\right)$  versus  $\left(\frac{T_N}{T}\right)$  in the critical region. One representative data set is illustrated in figures 25, 26, and 27. A summary of the concentration and linewidth measurements is shown in tables 2,3, and 4. The measured excitation energy appearing in each of these tables is an average of at least two measurements on each sample. The last graph mentioned above contained a linear fit to the data that yields the soliton excitation energies that are listed in the tables. Figures 28 to 36 represent a graphical summary of the linear fit plots obtained for every single measurement.

A similar trend in the temperature dependence of the linewidth is observed for each data set; as the temperature is lowered, the linewidth initially decreases, passes through a minimum near 70K and again increases rapidly as one approaches  $T_N$ . The lineshape was found to be nearly Lorentzian through the temperature region investigated. By observing the figures it can be seen that the linewidth consists of two regions; one between room temperature and 70K, where the linewidth increases approximately

linearly with temperature and another is the fluctuation region below the minimum but above  $T_N$  where the linewidth increases exponentially.

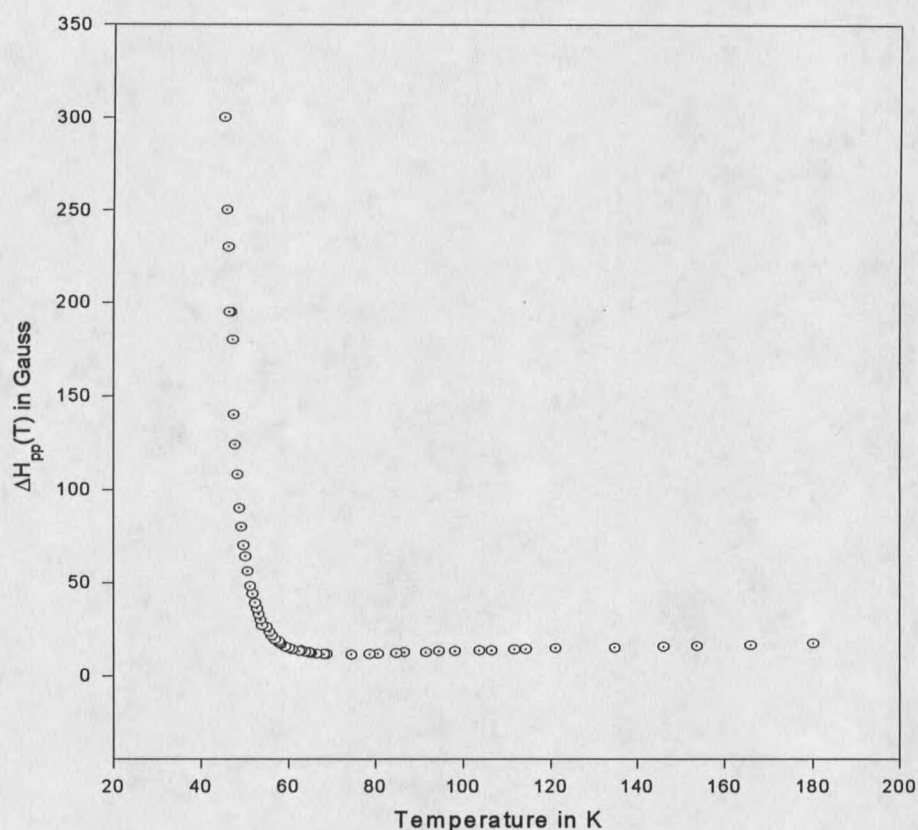


Figure 25. Linewidth temperature dependence of a 0.15% Cd doped sample.

The sharp rise in linewidth as one approaches the Neel temperature from above, is the illustrative behavior of solitons which was indicated by equation (3.37). It is safe to assume that the temperature dependence of  $\Delta H_{\infty}(T)$  is negligible in the relatively narrow fluctuation region and is contained in  $\Delta H_{crit}(T)$ . Below 46K the linewidth and the noise level increased to such an extent that an accurate measurement was no longer possible. The change in anisotropy below  $T = 65K$  coupled with the steep increase in the linewidths close to  $T_N$  helped us to define the narrow temperature region of interest as



































































































